論文 / 著書情報
Article / Book Information

題目(和文)	
Title(English)	A Watch-like Thrust-generating Attachable Device for Long-reach Robotic Arm Enhancement
著者(和文)	PanSiyi
Author(English)	Siyi Pan
出典(和文)	学位:博士（工学）, 学位授与機関:東京工業大学, 報告番号:甲第12034号, 授与年月日:2021年6月30日, 学位の種別:課程博士, 審査員:遠藤 玄,鈴森 康一,菅原 雄介,中西 洋喜,髙山 俊男
Citation(English)	Degree:Doctor (Engineering), Conferring organization: Tokyo Institute of Technology, Report number:甲第12034号, Conferred date:2021/6/30, Degree Type:Course doctor, Examiner:,,,,
学位種別(和文)	博士論文
Type(English)	Doctoral Thesis

A WATCH-LIKE THRUST-GENERATING ATTACHABLE DEVICE FOR LONG-REACH ROBOTIC ARM ENHANCEMENT

Siyi Pan

Academic Supervisors:

Prof. Gen Endo

Prof. Koichi Suzumori

A dissertation submitted to Department of Mechanical Engineering of Tokyo Institute of Technology in partial fulfillment of the requirements of the degree of Doctor of Engineering

Abstract

Long-reach robotic arms are useful for many applications, such as infrastructure inspection, nuclear plant decommissioning, and firefighting, due to their large workspaces, long operation time, and redundant degrees of freedom. However, a fundamental problem of a long robotic arm is that even an extremely small end effector reaction force or the arm gravity itself can result in significant torques on proximal joints that may overload actuators. Previous researchers proposed many specially designed long robotic arms that can counteract external reaction forces and arm gravity. However, those specialized long arms have two drawbacks. (1) Their force compensation mechanisms are difficult to be applied to other existing long robotic arms and (2) They are difficult to be customized to different missions.

To solve the fundamental problem of long robotic arms and overcome the drawbacks of specialized long robotic arms, this dissertation proposes a watch-like thrust-generating attachable device, called flying watch, which can be attached to the links of a long robotic arm with a mission-dependent attachment allocation and generate thrusts in cooperation with the original arm actuators to enhance arm strength. Firstly, the concept and mechanical design of flying watch is introduced. Next, a method called Allocation Optimization based on Weighted Situations (AOWS) for customizing the flying watch attachment allocation to different missions is described and verified through simulations. Then a model-based thrust planner, call Watch Actuator Cooperation for Arm Enhancement (WACAE) is described and verified using simulations. WACAE is an offline thrust planner suitable for situations when the arm model as well as mission procedures are known in advance. Finally, a model-free thrust planner, called Physical-gradient-based Optimization of Thrust (POT) is described and demonstrated for verification. POT is an online thrust planner that does not require any arm model or mission descriptions and can handle unexpected situations during a mission.

Table of Content

Abstract I
Table of Content II
List of Figures IV
List of Tables VII
List of Symbols VIII
1. Introduction 1
1.1. Research Motivation and Goal 1
1.2. Related Work 6
1.3. Contribution and Dissertation Organization 11
2. Flying Watch Concept and Design 14
2.1. Flying Watch Concept 14
2.2. Thrust Generating Unit Design 15
2.3. Thrust Generating Unit Experiments 20
2.4. Attachment Mechanism Design 25
2.5. Flying Watch Prototypes 28
2.6. Flying Watch Selection and Application Scope 30
2.7. Flying Watch Dynamics 35
2.8. Summary 38
3. Flying Watch Attachment Allocation Optimization 39
3.1. Reduction Rate 42
3.2. Thrust Drivability Surface 43
3.3. Thrust Drivability 46
3.4. Allocation Optimization based on Weighted Situations (AOWS) 48
3.4.1. Weighted Situation Model 49
3.4.2. DH-Allocation Description 49
3.4.3. Allocation Optimization based on Weighted Situations 50
3.4.4. Overall Allocation Design Process 52
3.5. Simulation Verification 54
3.5.1. Static Object Holding Mission 57
3.5.2. Object Manipulation Mission 65
3.6. Summary 70
4. Model-based Flying Watch Thrust Planning 74

4.1. Watch Actuator Cooperation for Arm Enhancement 74
4.2. Simulation Verification 80
4.3. Summary 90
5. Model-free Flying Watch Thrust Planning 92
5.1. Physical-gradient Optimization of Thrust (POT) 93
5.1.1. Memory-based Thrust Prediction 96
5.1.2. Physical Gradient Probing 97
5.1.3. Physical Line Search 100
5.1.4. Physical-gradient-based Optimization of Thrust 101
5.2. Demonstration 104
5.3. Summary 107
6. Conclusion 109
Reference 112
Publications 118
Acknowledgments 119

List of Figures

1.1. An example of passive force counteraction long robotic arm…..……...…… 2
1.2. An example of active force counteraction long robotic arm ……3
1.3. A flying watch prototype ……4
1.4. Applications of Flying Watch ……5
1.5. Air thrust driven robotic arms ……6
1.6. Water-jet driven robotic arms ……7
1.7. Thrust-assisted robots……..8
1.8. Arm-based aerial manipulation systems……..9
1.9. Body-based aerial manipulation systems……9
1.10. Ground-aerial hybrid manipulation systems……10
1.11. Torque Unit Manipulator……10
2.1. The basic components of a flying watch……15
2.2. Mechanisms of Thrust-generating Unit……..16
2.3. The hardware system of propeller flying watches……18
2.4. The hardware system of propellerless flying watches……19
2.5. The equipment for thrust experiment of propeller thrust-generating unit……...20
2.6. The equipment for thrust experiment of propellerless thrust-generating unit…….22
2.7. Design of propellerless thrust-generating unit……22
2.8. Pure thrusts and gravity of propellerless flying watch……23
2.9. Flying watch belt designs……...26
2.10. Possible flying watch buckles…..……27
2.11. Propeller flying watch prototype (propeller TGU + modified bar belt)……..28
2.12. Propeller flying watch prototype (propeller TGU + modified Zulu belt)……29
2.13. Propeller flying watch prototype (propeller TGU + modified NATO belt)…….29
2.14. Propellerless flying watch prototype (propellerless TGU + modified Zulu belt)……..30
2.15. Meaning of Workspace Factor..……...32
2.16. Design of Planar Inspection Arm……33
3.1. Customization of flying watch attachment allocation……39

3.2. Thrust Drivability Surface…….47

3.3. The overall design process of flying watch allocation……..53

3.4. Specification of the simulation arm and the human-experience-based design of flying watch allocation…….55

3.5. Human-experience-based flying watch allocation in the static object holding mission….59

3.6. Thrust Drivability Surface of human-experience-based flying watch allocation in the static object holding mission……...60

3.7. AOWS-based flying watch allocation in the static object holding mission……..61

3.8. Thrust Drivability Surface of AOWS-based flying watch allocation in the static object holding mission……..……..62

3.9. The sequence of arm configurations in the object manipulation mission……..66

3.10. Human-experience-based flying watch allocation in the object manipulation mission…69

3.11. Thrust Drivability Surface of human-experience-based flying watch allocation in the object manipulation mission……..……..70

3.12. AOWS-based flying watch allocation in the object manipulation mission……..71

3.13. Thrust Drivability Surface of AOWS-based flying watch allocation in the object manipulation mission……...72

4.1. The setup of the simulation robotic arm and flying watches……..82

4.2. The simulation arm and flying watch thrusts under WACAE-I when the end effector reaction force is [125,0,0] N (RLR = 24.1%)…….…….……..85

4.3. The simulation arm and flying watch thrusts under WACAE-II when the end effector reaction force is [125,0,0] N (RLR = 35.6%)…….……...85

4.4. The simulation arm and flying watch thrusts under WACAE-I when the end effector reaction force is [0,125,0] N (RLR= − 20.6%)…….……86

4.5. The simulation arm and flying watch thrusts under WACAE-II when the end effector reaction force is [0,125,0] N (RLR = 31.7%)……...…….……86

4.6. The simulation arm and flying watch thrusts under WACAE-I when the end effector reaction force is [0,0,− 125] N (RLR = − 1.0%)…….……....87

4.7. The simulation arm and flying watch thrusts under WACAE-II when the end effector reaction force is [0,0,− 125] N (RLR = 20.8%). ……87

5.1. The system integration of POT and original arm controller……..93

5.2. The workflow of POT……95

5.3. Planar Inspection Arm attached with two flying watches…….104

5.4. System design of PIA enhanced by flying watches……..104

5.5. Demonstration of POT on PIA…….106
5.6. PIA trajectory in POT demonstration……..106

List of Tables

2.1. Advantages and Disadvantages of Different TGU Arrangements……..17

2.2. Results of Propellerless Flying Watch Thrust Test……..……..24

3.1. AOWS-based and human-experience-based allocations of static mission……...…..58

3.2. Thrust drivability of static object holding mission……....64

3.3. AOWS performance under different condition……..65

3.4. AOWS-based and human-experience-based allocations of object manipulation mission……...……..67

3.5. Thrust drivability of object manipulation mission…….70

4.1. Joint torques of example cases…….…….84

4.2. Overall performance of flying watches……..……88

4.3. Speed of example WACAE solution…….89

5.1. Specification of planar inspection arm…….105

List of Symbols

s	Magnitude of flying watch thrust
$\dot{m}_e$	Mass flow rate of discharging air
v_e	Velocity of discharging air
ρ_{air}	Air density
Q	Flow rate
A	Nozzle area
ΔP	Difference of interior and exterior pressure of a propellerless flying watch
C_d	Discharge Coefficient
f_{ae}	Actuator enhancement factor
s_c	Characteristic thrust of a flying watch
l_{arm}	Length of a robotic arrm
τ_a	Maximum actuator load exerted on arm joints
f_{rc}	Reaction counteraction factor
τ_r	Maximum torque due to environmental reaction force
g	Gravity acceleration
l_c	Characteristic length of a flying watch
l_{link}	Length of an attached arm link
f_w	Workspace factor
θ_{link}	Obstruction angle
N_f	Number of attached flying watches
v	Wind speed
C_{dr}	Drag coefficient
E	Kinetic energy
t	Time
$\boldsymbol{q}$	Generalized coordinate
$\boldsymbol{Q}$	Generalized force
U	Potential energy
$\boldsymbol{\tau}$	Actuator load vector

$\boldsymbol{p}$	End effector position and orientation
$\boldsymbol{F}_e$	External reaction force and torque on the end effector
$\boldsymbol{T}_k$	Thrust generated by the k th flying watch
$\boldsymbol{r}_k$	Position vector of the k th flying watch
$\boldsymbol{J}$	Jacobian matrix of the end effector
$\boldsymbol{J}_k^f$	Jacobian matrix of k th flying watch
$\boldsymbol{M}$	Manipulator inertia tensor
$\boldsymbol{h}$	Velocity term of the Equation of Motion
$\boldsymbol{g}$	Gravity term of the Equation of Motion
$\boldsymbol{a}_k$	Unit direction vector of the k th flying watch
s_k	Thrust magnitude of the k th flying watch
$\boldsymbol{R}$	Attachment style matrix
$\boldsymbol{s}$	Thrust magnitude vector
$\boldsymbol{H}$	Normalization matrix of joint load
$\tilde{\boldsymbol{\tau}}$	Normalize joint load vector
τ_p	Maximum permitted loads
$\tilde{\boldsymbol{J}}$	Normalized Jacobian Matrix
$\widetilde{\boldsymbol{R}}$	Normalized attachment style matrix
$\widetilde{\boldsymbol{g}}$	Normalized Gravity term of Equation of Motion
ζ	Reduction rate
$\tilde{\boldsymbol{\tau}}_{bm}$	Normalized joint load of a benchmark case
$\boldsymbol{s}_{bm}^*$	Optimized flying watch thrust of a benchmark case
$\tilde{\boldsymbol{\tau}}_{coi}$	Normalized joint load of a case of interest
$\boldsymbol{s}_{coi}^*$	Optimized flying watch thrust of a case of interest
$\boldsymbol{s}_u$	Upper bound of flying watch thrust
$\boldsymbol{s}_l$	Lower bound of flying watch thrust
$\boldsymbol{F}_k$	Known end effector reaction force
$\boldsymbol{F}_u$	Unexpected end effector reaction force
$\boldsymbol{s}_k$	Flying watch thrusts for counteracting know effects
$\boldsymbol{s}_u$	Flying watch thrusts for counteracting unexpected effects
$\tilde{\boldsymbol{\tau}}_k$	Normalized joint loads resulted from known effect
$\tilde{\boldsymbol{\tau}}_u$	Normalized joint loads resulted from unexpected effect

$\boldsymbol{s}_u^+$	Optimal solution
$\boldsymbol{b}$	Intermediate load vector
θ	Polar angle
ϕ	Azimuthal angles
$\boldsymbol{e}$	Unit end effector reaction force
ρ	Radial distance
θ_l	Lower bound of polar angle
θ_u	Upper bound of polar angle
ϕ_l	Lower bound of azimuthal angle
ϕ_u	Upper bound of azimuthal angle
D	Thrust Drivability
$\boldsymbol{\omega}$	Direction region
$\boldsymbol{\Pi}$	Weighted situation model
$\tilde{\boldsymbol{\tau}}_{bm}^*$	Optimal normalized joint loads of a benchmark allocation
$\tilde{\boldsymbol{\tau}}_k^*$	Optimal normalized joint load due to known effect
$\boldsymbol{s}_{bm}^*$	Optimal thrust magnitude vector for a benchmark allocation
$\boldsymbol{s}_k^*$	Optimal thrust magnitude vector for counteracting known effect
$\tilde{\boldsymbol{\tau}}_u^0$	Normalized joint load vector due to unknown effect with zero watch thrusts
$\tilde{\boldsymbol{\tau}}_u^+$	Optimal normalized joint load due to unknown effect
$\tilde{\boldsymbol{\tau}}^*$	Optimum normalized total joint load
$\boldsymbol{s}^*$	Optimum total thrust magnitude vector
k	Ratio of unknown effect
$\boldsymbol{E}$	Set of situations
$\boldsymbol{P}$	Set of importance factors
$\boldsymbol{\mu}_f$	Full DHAD vector
$\boldsymbol{\mu}_d$	Displacement components of full DHAD
$\boldsymbol{\mu}_\eta$	Orientation components of full DHAD
$\boldsymbol{d}$	Displacement vector of a flying watch
$\boldsymbol{a}$	Direction vector of a flying watch
$\boldsymbol{R}_i^{DH}$	Rotation matrix of the i th DH frame
$\boldsymbol{r}_i^{DH}$	Position vector of the i th DH frame

$\boldsymbol{\mu}_s$	Simplified DHAD vector
$\boldsymbol{\mu}_{sd}$	Coordinate of the flying watch on X axis of the i th DH frame
$\boldsymbol{\mu}_{s\eta}$	Angle between flying watch thrust vector and Y axis of the i th DH frame
$\tilde{\boldsymbol{\tau}}_{ki}^{0}$	Normalized joint load vector due to known effect with zero watch thrusts
$\tilde{\boldsymbol{\tau}}_{ki}$	Normalized joint load vector due to known effect in the i th situation
$\boldsymbol{\mu}$	Full or simplified DHAD vector
$\boldsymbol{F}_{ki}$	Known end effector reaction force in the i th situation
$\boldsymbol{s}_i$	Flying watch thrust magnitude vector of the i th situation
$\boldsymbol{q}_i$	Arm configuration of the i th situation
p_i	Importance factor of the i th situation
α_j	Drivability weight factor of the j th situation
β	Unexpected effect weight factor
D_{ij}	Weighted situation model
$\boldsymbol{\omega}_j$	The j th direction region
$\boldsymbol{C}$	Constraints
$\boldsymbol{q}_{m1}$	Arm configuration of the static object holding mission
$\boldsymbol{\Pi}_{m1}$	Weighted situation model of the static object holding mission
$\boldsymbol{E}_{m1}$	Set of situations of the static object holding mission
$\boldsymbol{P}_{m1}$	Set of importance factors of the static object holding mission
$\boldsymbol{\omega}_{m1}$	Direction region of the static object holding mission
$\boldsymbol{Q}_{m2}$	Set of arm configurations in the object manipulation mission
$\boldsymbol{F}_{m2}$	Set of end effector reaction forces in the object manipulation mission
$\boldsymbol{E}_{m2}$	Set of situations in the object manipulation mission
$\boldsymbol{\Pi}_{m2}$	Weighted situation model of the object manipulation mission
α_{m2}	Drivability weight factor of object manipulation mission
$\boldsymbol{\omega}_{m2}$	Direction region of the object manipulation mission
α_{m1}	Drivability weight factor of static object holding mission
β_{m1}	Unexpected effect weight factor of static object holding mission
β_{m2}	Unexpected effect weight factor of object manipulation mission
$\boldsymbol{q}_l$	Lower bound of generalized coordinates of arm
$\boldsymbol{q}_u$	Upper bound of generalized coordinates of arm
$\boldsymbol{p}_d$	Desired end effector position and orientation

$\boldsymbol{V}$	Unlocked generalized coordinates
$\boldsymbol{I}_l$	Index of the locked generalized coordinates
$\boldsymbol{L}$	Locked generalized coordinates
N_r	Dimensions of optimizable generalized coordinates
$\boldsymbol{\xi}$	Index of optimizable generalized coordinates
C	Cost function
$\boldsymbol{q}_r$	Optimizable redundant generalized coordinates
$\boldsymbol{\psi}$	Updating direction
C_{NO_FW}	Maximum normalized actuator load without flying watch
C_{FW}	Maximum normalized actuator load under the WACAE
$\boldsymbol{V}_l$	Lower bound of unlocked generalized coordinates
$\boldsymbol{V}_u$	Upper bound of unlocked generalized coordinates
Λ	Cost function of POT
$\boldsymbol{\tau}_a$	Actuator load vector
$\boldsymbol{H}_a$	Normalization matrix of actuator load
$\tilde{\boldsymbol{\tau}}_a$	Normalized actuator load vector
τ_{ap}	Maximum permitted actuator loads
$\boldsymbol{s}_{pred}$	Predicted flying watch thrust magnitude vector
$\widehat{\Lambda}$	Measurement of the cost function of POT
δ_T	Very small change of thrusts
$\boldsymbol{e}_i$	A unit vector with the i th component as 1
$\boldsymbol{\eta}$	Vector indicating optimizable generalized coordinate
ϵ	Very small change of generalize coordinates
$\boldsymbol{q}_0$	Initial value of generalized coordinate
$\boldsymbol{s}_{back}$	Temporary record of thrust magnitude vector
$\boldsymbol{\delta}_{\boldsymbol{s}}$	Gradient of cost function regarding thrust magnitude
$\boldsymbol{\delta}_{\boldsymbol{q}_r}$	Gradient of cost function regarding optimizable generalized coordinates
t_{WACAE}	Step size of WACAE
η	Relative Load Reduction
$\boldsymbol{q}_{cur}$	Current arm configuration
δ_{idw}	Equality threshold used in inverse distance weighting
γ	Power parameter in inverse distance weighting

N_{idw}	Size of memory for storing previous arm configuration
δ_T	Vibration magnitude for physical gradient probing
β_T	Incremental factor of vibration magnitude for physical gradient probing
$\boldsymbol{g}_p$	Partially calculated physical gradient
δ_T^{max}	Maximum value of Vibration magnitude for physical gradient probing
α_{pls}	Parameter of physical line search
t_{pls}	Step size of physical line search
t_{pls}^{max}	Maximum step size of physical line search
β_L	Incremental factor of step size for physical line search
τ_{permit}	Maximum permitted joint load in POT
$\boldsymbol{s}_{temp}$	Temporary thrust magnitude vector in POT
t_{pot}	Step size of POT
$\boldsymbol{s}_{pruning}$	Thrust magnitude vector under pruning in POT
K	Degrees of Freedom of an arm
V_{TDS}	Volume of TDS in a given direction region
V_{unit}	Volume of a unit sphere in a given direction region
$\boldsymbol{r}_k$	Position of the k th flying watch
λ	Damp parameter of damped least squares method
ξ_{m2}	Trajectory parameter of the object manipulation mission
f_{belt}^{max}	Maximum pulling strength of watch belt
f_{buckle}^{max}	Maximum pulling strength of watch buckle
T_{TGU}^{max}	Maximum thrust of a TGU
G_{watch}	Gravity of flying watch
s_{safe}	Safety factor
L	Lagrangian

1. Introduction

1.1. Research Motivation and Goal

Long-reach robotic arms have the following three major features. (1) Large workspaces. (2) Many redundant Degrees of Freedom (DoF) to negotiate obstacles. (3) Very long operation time since the power supply is directly connected to the arm base. Another type of robots we may compare with long robotic arms is Unmanned Aerial Vehicle (UAV) (including aerial manipulators) since an UAV also have large workspaces and can negotiate obstacles. However, an UAV with onboard power supply (e.g. LiPos) generally cannot operate for a long time and UAVs tethered to ground power source [1], [2] have a high operation risk of tether-obstacle entanglement (UAV Energy Conundrum). Because of those long arm features, long robotic arms are useful for many applications such as infrastructure inspection [3]-[5], nuclear plant decommissioning [6],[7], and firefighting [8].

A fundamental problem for building and operating a long-reach arm is that even a small end effector reaction force or the arm gravity itself may result in extremely large torques on proximal joints that can exceed their actuation ability because of long moment arms.

To solve this problem, previous researchers proposed varieties of specially designed long robotic arms which can counteract end effector reaction forces and arm gravity. Those arms can be classified into two classes, passive force counteraction arms and active force counteraction arms, based on whether an energy source is required for force counteraction. Regarding passive force counteraction arms, in [3], a 20-m-long arm with helium balloon links was proposed to carry small loads like cameras as shown in Fig. 1.1. The joint torques due to end effector reaction forces and gravity was passively counteracted by the buoyancy of helium. In [4], a 9.5-m-long modular arm with spring-based weight compensation mechanisms was

built for inspection of an ITER related nuclear fusion device. Additionally, some gravity compensating arm designs based on springs [9], [10] and weight [11] may also be used for designing passive force counteraction long arms. Regarding active force counteraction arms, in [6], [7] specialized coupled tendon-driven arms that can compensate gravity were proposed. In [5], [8], arms that apply water jets to counteract gravity were proposed. In [13]- [15], arms with passive joints driven by thrusters to counteract external reaction forces were proposed.

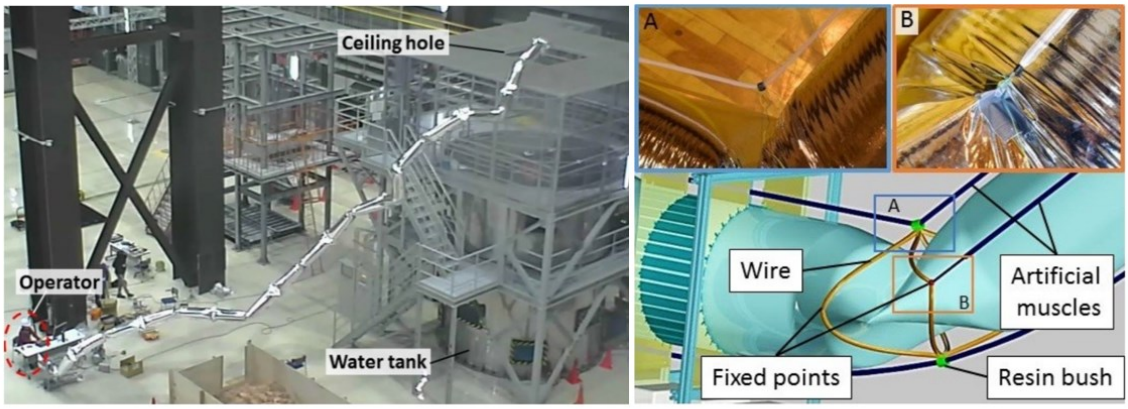

Fig. 1.1. An example of passive force counteraction long robotic arm. The arm is proposed in [3], called Giacometti Arm. (a) Demonstration of Giacometti Arm. (b) Detailed arm design of Giacometti Arm. This figure is adapted from [3] © 2017 IEEE.

However, specially designed long robotic arms have two major drawbacks. (1) They are difficult to be customized to different missions. (2) Their designs are difficult to be applied to other long arms. For example, the arm designed in [3] as shown in Fig. 1.1 can counteract gravity using helium buoyancy, which is useful for carrying sensors such as cameras. However, if we want the arm to push aside objects on the ground, whose reaction forces are horizontal, the arm may not be able to provide enough end effector forces. Therefore, it is difficult to customize the arm in [3] to different missions. For pushing objects aside, the arm design in [14] (as shown in Fig. 1.2) is suitable since it can counteract reaction forces in different directions using thrusters. However, adapting the arm design in [14] to the existing arm in [3] requires

significant mechanical modification. Therefore, it is difficult to apply the special long arm designs to other long arms.

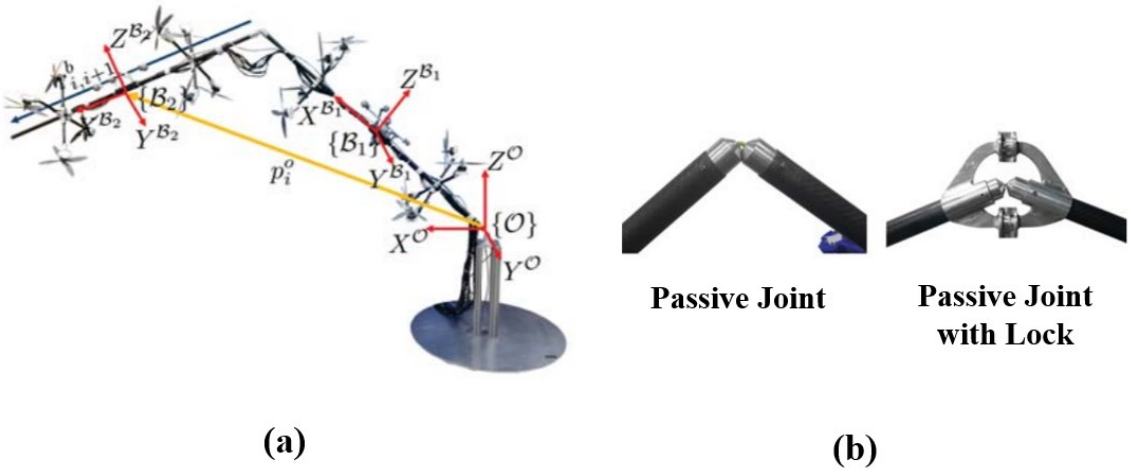

Fig. 1.2. An example of active force counteraction long robotic arm. The arm is proposed in [14], called LASDRA. (a) Overall view of LASDRA. (b) Passive joint design of LASDRA. This figure is adapted from [14] © 2018 IEEE.

To solve the fundamental problem of long robotic arms and overcome the drawbacks of specialized long robotic arms, the goal of this dissertation is to develop a watch-like thrust-generating attachable device, called flying watch (as shown in Fig. 1.3) [16], which can be attached to the links of a long robotic arm using a mission dependent attachment allocation and generate thrusts in cooperation with the original arm actuators to enhance arm strength.

We can see from Fig.1.3, just like a typical wristwatch, a flying watch also have a main watch body, removable and adjustable watch belt, and belt buckle. The major difference is that the main watch body of the flying watch have thrust-generating mechanisms (such as propellers) instead of timekeeping mechanisms.

Flying watch is useful and important for its two major applications. (1) Flying watch can significantly boost the strength and versatility of varieties of existing long robotic arms as

shown in Fig. 1.4 (a). (2) Flying watch provides a new option of designing reconfigurable long robotic arms as shown in Fig. 1.4 (b).

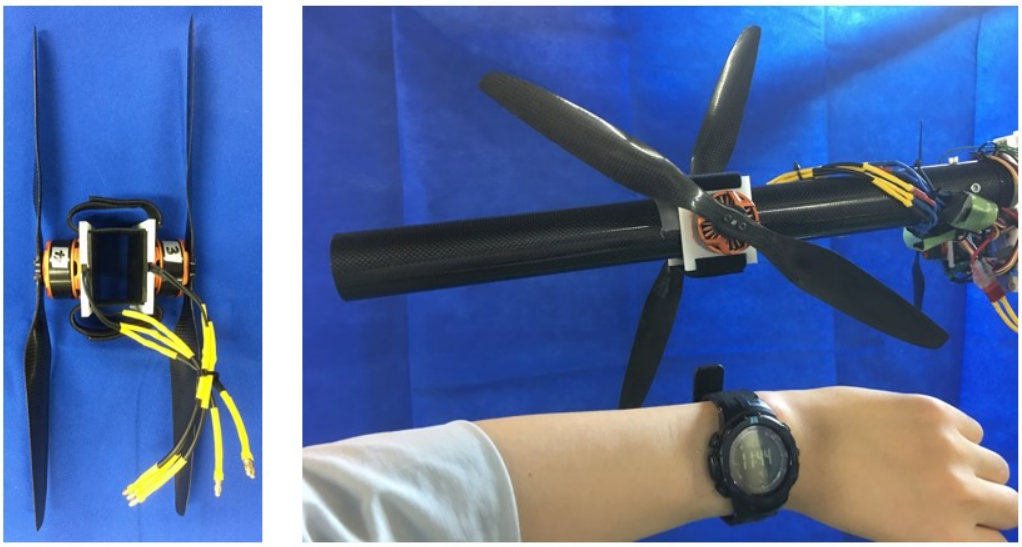

(a) (b)

Fig. 1.3. A flying watch prototype. (a) A flying watch before attachment. (b) A flying watch after attaching to the link of a robotic arm. This figure is adapted from [16].

Regarding the application of flying watch to boost the strength and versatility of long robotic arm, flying watches can be easily attached to the links of varieties of long arms and generate thrusts in cooperation with existing arm actuators to boost arm strength. Since flying watches are usually attached on distal links, the generated thrusts can result in significant enhancement torque on proximal joints due to long moment arms. In addition, different attachment allocations of flying watches can enhance the same long arm in different ways. If we customize the flying watch attachment allocation, we can enhance a long robotic arm in a mission-dependent way and therefore improve the versatility of the long robotic arm. For example, as shown in Fig.1.4 (a), when the mission is picking and placing, since end effector reaction forces is vertical, the two flying watches are attached to generate vertical thrusts. When the mission is debris removal, since debris needs to be picked and placed to other places or pushed or pulled on the ground to other places, both vertical and horizontal end effector

reaction forces are possible, one flying watch is attached to generate horizontal thrusts and the other flying watch is attached to generate vertical thrusts.

Regarding the application of flying watch to design reconfigurable long robotic arms, we can design a new long robotic arm whose property depends on the number and attachment allocation of deployed flying watches. As a result, such reconfigurable long robotic arms can adapt to diverse missions. For example, as shown in Fig. 1.4 (b), the basic arm configuration does not include any flying watch. As we attach more flying watches, the arm strength will be improved while the workspace will shrink, since flying watch can interfere with other links and limit the rotation range of corresponding joints. We can also imagine many more possible configurations of the long arm in Fig. 1.4 (b) by changing the number and attachment allocation of flying watches.

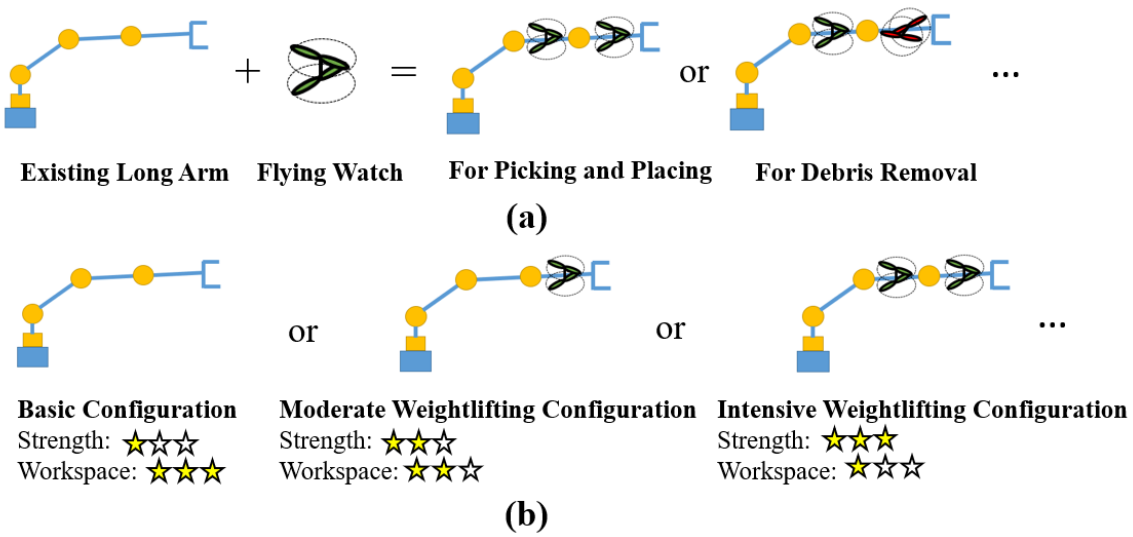

Fig. 1.4. Applications of Flying Watch. (a) Boosting strength and versatility of varieties of existing long robotic arms. (b) Building new reconfigurable long robotic arms.

In this dissertation, if there is no special explanation, “strength” means the ability of a robotic arm to exert forces through its end effector along a certain direction. Such ability can be quantitively measured by the maximum end effector reaction force along a certain direction.

In this dissertation, we will also discuss the material strength of some mechanical parts. In such situation, the dissertation will clearly state “material strength”.

1.2. Related Work

Thrust driven robotic arms [13]-[15], [5], [8] are closely related to flying watch. In [13], as shown in Fig. 1.5 (a), a 3 m long arm with parallelogram link and gravity-counteraction thrusters is proposed. In [15], as shown in Fig. 1.5 (b), a 6.6 m long arm with gravity-counteraction thrusters is proposed. Compared with [13], small thruster generating thrusts in horizontal directions are added to better stabilize the arm. In [14], as shown in Fig. 1.2, a robotic arm called LASDRA is proposed. Each link of the arm includes 8 propellers of different orientations to counteract end effector reaction forces in different directions. In addition to generating air thrust, [5] and [8] proposed water jet driven arms as shown in Fig. 1.6. Similar to flying watch, thrust-driven arms also generate thrusts with large moment arms to counteract reaction forces. However, there are two major differences. (1) Thrust-driven arms use thrusts

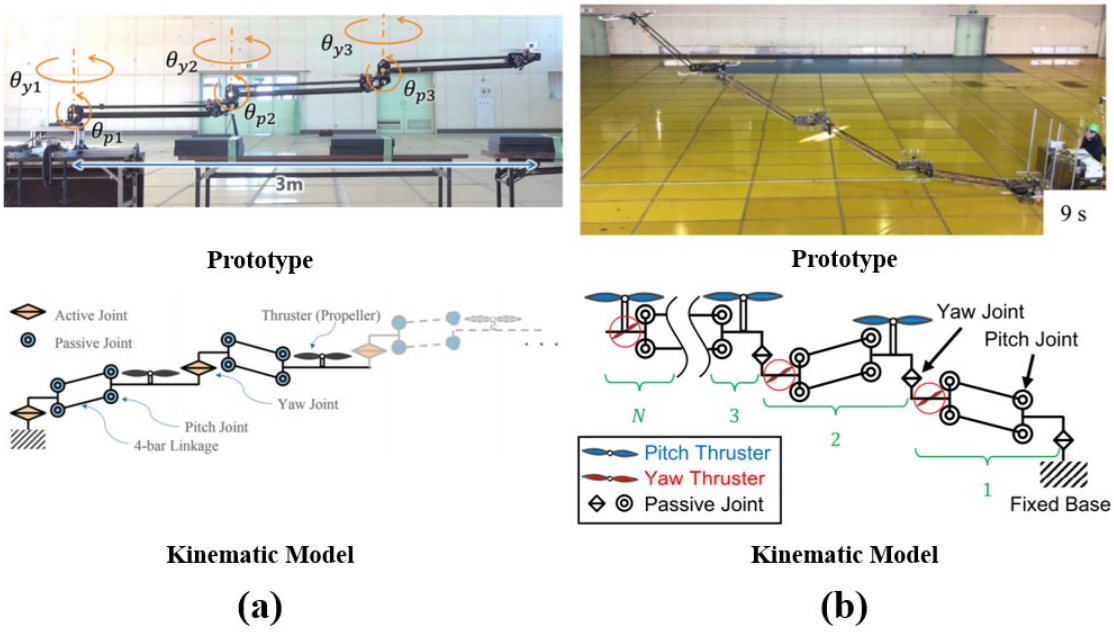

Fig. 1.5. Air thrust driven robotic arms. (a) Hiryu-I. (b) Hiryu-II. (a) is adapted from [13] © 2018 IEEE. (b) is adapted from [15] © 2020 IEEE

to drive only passive joints and there is no cooperation between thrusters and actuators. (2) The attachment allocation of flying watches can be customized to enhance a long arm according to a specific mission. However, the thruster allocation of thrust-driven arms cannot be easily changed. Because of those differences, we can regard a thrust-driven robotic arm as a special case of a flying watch enhanced robotic arm when all loads on passive joint are counteracted by flying watches and flying watch allocations are not allowed to be customized.

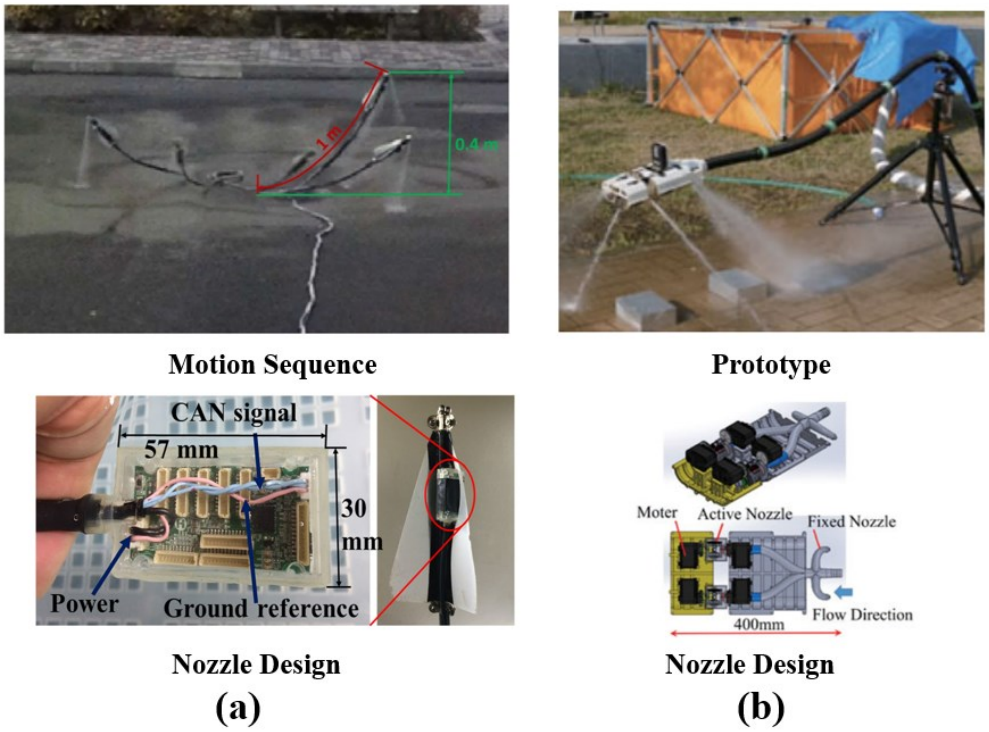

Fig. 1.6. Water-jet driven robotic arms. (a) Water-jet Probe. (b) Aerial Hose Type Robot. (a) is adapted from [5]. (b) is adapted from [8] © 2018 IEEE

Thrust-assisted robots [17]-[19] are also related to flying watch. In [17], [18], a humanoid robot called Jet-HR1 as shown in Fig. 1.7 (a), with ducted fans installed on feet is proposed. The ducted fan on the feet can generate thrusts to help the robot step over broad ditches. In [19], a serpentine robot, called Air-floating-type active scope camera as shown in Fig. 1.7 (b), is proposed. The serpentine normally uses cilia actuated by vibrating motor to move. However, when there is a high step, the nozzle on the head of the robot can generate thrusts to levitate the robot head in order to negotiate the high step. Thrust-assisted robots use thrusters to

enhance the performance of actuators. In such sense, robotic arms attached with flying watches can be seen as a type of thrust assisted robots. However, there are two major difference between previous thrust-assisted robots and flying watch. (1) the allocation of thrusters on previous thrust-assisted robots cannot be customized to different missions. (2) Previous thrust-assisted robots are not arm-type robots with fixed bases. Therefore, their dynamics are very different from flying watch enhanced robotic arms.

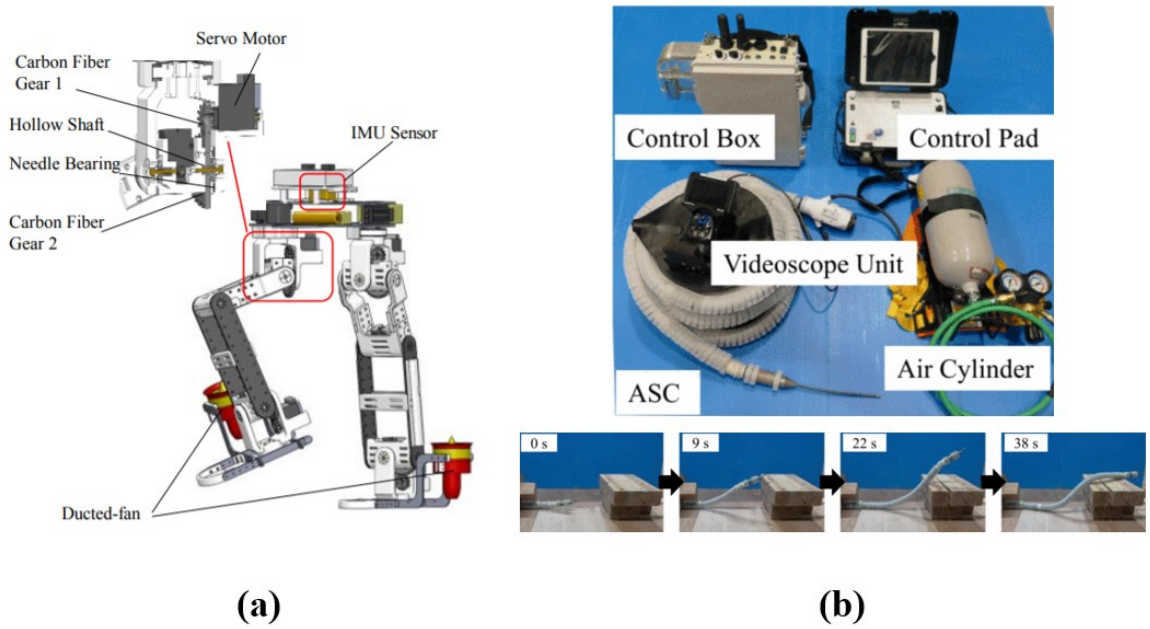

Fig. 1.7. Thrust-assisted robots. (a) Jet-HR1. (b) Air-floating-type Active Scope Camera. (a) is adapted from [18] © 2020 IEEE. (b) is adapted from [19] © 2019 IEEE

Aerial manipulation and aerial transformation systems are also related to flying watch. Those systems can be classified into three types. The first type is arm-based aerial manipulation systems [20]-[22] as shown in Fig. 1.8 which involves a UAV equipped with a robotic arm (or a robotic hand). In those aerial manipulation systems, a UAV acts as the base of the robotic arm and the robotic arm connected with the UAV interacts with environment. The second type is body-based aerial manipulation systems [23]-[26] as shown in Fig. 1.9, which involves aerial transformation of mechanically connected UAVs that can catch an object with the robot bodies. The third type is ground-aerial hybrid manipulation systems [27]-[29] as shown in Fig. 1.10, where an arm-based aerial manipulator cooperates with ground manipulator to manipulate an

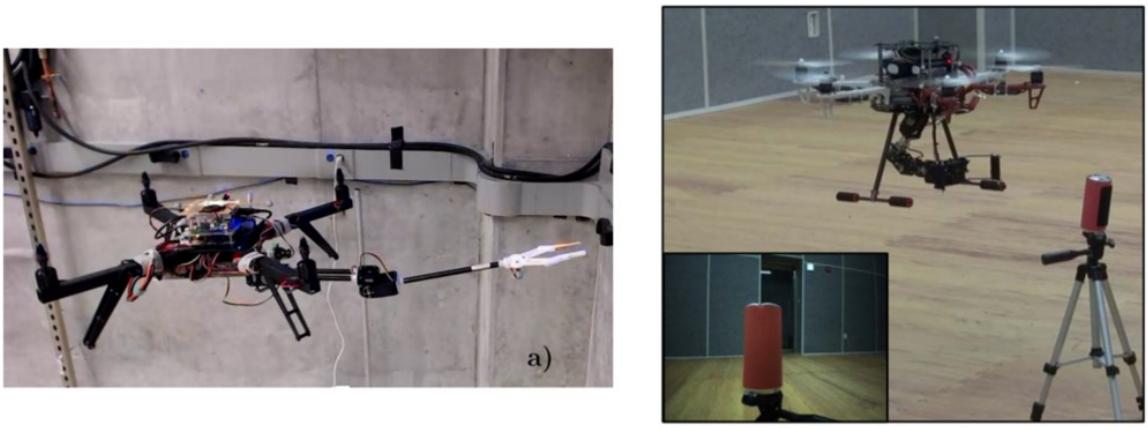

Fig. 1.8. Arm-based aerial manipulation systems. (a) aerial manipulation system proposed in [20]. (b) aerial manipulation system proposed in [21]. (a) is adapted from [20] © 2015 IEEE. (b) is adapted from [21] © 2017 IEEE

Fig. 1.9. Body-based aerial manipulation systems. (a) aerial manipulation system proposed in [23]. (b) aerial manipulation system proposed in [24]. (a) is adapted from [23] © 2018 IEEE. (b) is adapted from [24] © 2017 IEEE

object. All those three types of aerial manipulation are similar to flying watch attached robotic arms in that the thrusters need to cooperate with arm or body actuators. However, the differences are as follows. (1) All those UAVs still have to face UAV Energy Conundrum in contrast with flying watch connected with unlimited ground power supply. Secondly, the dynamics properties of these UAV systems and flying watch are very different. For the first and second type aerial manipulation systems, the whole systems are floating in the air and the major challenge is to stabilize the flying postures [22]. However, the base of a flying watch enhanced long robotic arm is fixed on the ground and the major challenge is to counteract large proximal joint torques. For the third type of aerial manipulation systems, although the base of

a ground manipulator is also fixed on the ground, the UAVs have much more flexible constraints since they do not need to be fixed on arm links as flying watches do.

Fig. 1.10. Ground-aerial hybrid manipulation systems. This figure is adapted from [27] © 2018 IEEE

Toque Unit Manipulator (TUM) [30], [31] as shown in Fig. 1.11 is also closely related to flying watch. All the joints of TUM are passive and actuated by reaction torques from rotating disks on the links. Similar to flying watch, the attachment allocation of rotating disks is potentially customizable. However, TUM is different from flying watch in the following two

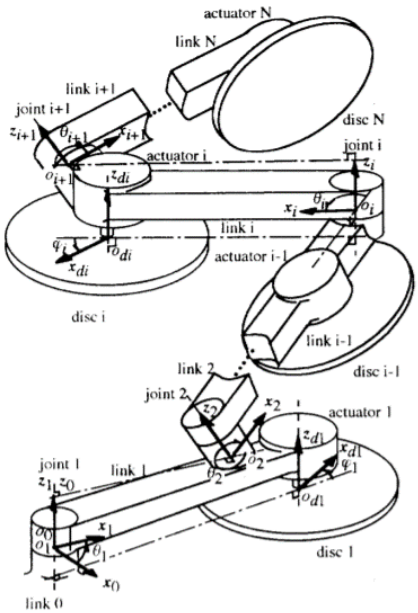

Fig. 1.11. Torque Unit Manipulator. This figure is adapted from [30] © 1994 IEEE

ways. (1) No systematic attachment allocation method is proposed for TUM and how to design mission-dependent attachment allocation of the rotating disks is not clear. (2) The rotating disks are essentially reallocating arm actuators instead of enhancing arm actuators. Since the disk induced torques equals corresponding disk actuation motor torques, such rotating disk units is just reallocating arm actuators from joints to links instead of enhancing arm actuators. And reallocating arm actuators does not help building or operating long arms.

1.3. Contribution and Dissertation Organization

The contributions of this dissertation are as follows.

(1) Proposing the concept, design, and dynamic model of flying watch and implement several flying watch prototypes.

(2) Proposing analysis tools including reduction rate, thrust drivability surface, and thrust drivability to evaluate the performance of flying watch attachment allocations and demonstrate those tools in simulations.

(3) Proposing an automated method called Allocation Optimization based on Weighted Situations (AOWS) for customizing flying watch attachment allocation to a specific mission and verifying its effectiveness using simulations.

(4) Proposing a model-based flying watch thrust planner, called Watch-Actuator Cooperation for Arm Enhancement (WACAE), and verifying its effectiveness using simulations.

(5) Proposing a model-free flying watch thrust planner, called Physical-gradient-based Optimization of Thrust (POT), and verify its effectiveness using physical demonstration.

The organization of this dissertation is as follows.

Chapter 2: This Chapter introduces the concept, design, application scope, and mathematical model of flying watch. The flying watch concept and varieties of flying watch designs and prototypes are firstly introduced. Then how to choose an appropriate flying watch for a specific long robotic arm is introduced. Finally, the Equation of Motion (EoM) of flying watch enhanced arms is derived, which is used in the following Chapters.

Chapter 3: After knowing flying watch designs and building several flying watches in Chapter 2, the next question would be how to attach flying watches for a specific mission and how to evaluate the performance of a certain flying watch attachment allocation. This Chapter answers those questions. More specifically, this Chapter will first introduce several analysis tools for understanding the performance of a flying watch attachment allocation. Then an automated design tool, called AOWS, will be introduced for generating an optimal flying watch attachment allocation according to a specific mission. With such customized attachment allocation, flying watch will be able to enhance a robotic arm in a mission-dependent way. Finally, AOWS will be verified in simulations.

Chapter 4: After building and properly attaching flying watches, the next important problem is to operate watch thrusts. This Chapter solves this problem by introducing an offline model-based thrust planner, called Watch-Actuator Cooperation for Arm Enhancement (WACAE). WACAE is an offline model-based method because it requires arm model and prior knowledge of a mission and the thrust planning is done before a mission. WACAE is suitable when we have a precise arm model and know exactly what will happen during a mission. The performance of WACAE is verified by simulations.

Chapter 5: This Chapter introduces an online model-free thrust planner, called Physical-gradient Optimization of Thrust (POT). POT requires no prior knowledge about the robotic arm, attachment allocation, and mission and the flying watch thrusts are determined during a

mission. POT can adapt to unexpected situations during a mission and is suitable when we do not know clearly what will happen during a mission. The performance of POT is verified by a physical demonstration.

Chapter 6: This Chapter summarize this dissertation and discuss possible future research directions of flying watch.

2. Flying Watch Concept and Design

What is a flying watch? How to build a flying watch? How to select a proper flying watch? What kind of motions do flying watches make? This Chapter answers those fundamental and important questions by introducing the mechanical design and dynamics of flying watch. More specifically, the concept of flying watch will firstly be explained. Then several flying watch designs and prototypes will be demonstrated. Next, several criteria for selecting appropriate flying watch designs will be introduced. Finally, the Equation of Motion (EoM) of flying watch enhanced robotic arms is derived.

2.1. Flying Watch Concept

People wear wristwatches in different kinds of missions (such as office work, sports, diving, military operations, etc.). In order to adapt to users' diverse wrist dimensions and different mission requirements, wristwatches come with different sizes, mechanism, and designs. Usually, a wristwatch is composed of a main watch body (i.e. timekeeping unit), adjustable and exchangeable watch belt, and watch buckles. Similarly, robotic arms have different dimensions and need to achieve different missions. Inspired by the wristwatch and thrust actuated arms [5], [8], [13]-[15], we imagine there could be a watch-like thrust-generating attachable device, named flying watch, that also come with different sizes, mechanisms, and designs in order to adapt to different robotic arms and missions.

More specifically, a flying watch is defined as a watch-like, thrust-generating, and attachable device that can be attached to links of robotic arms and generate thrusts in cooperation with original arm actuators to enhance arm strength. In addition, the attachment allocation of flying watches can be customized in order to enhance a robotic arm in a mission-dependent way. From the flying watch definition, we can understand a flying watch should

mainly be composed of Thrust-generating Units (TGU) and an attachment mechanism as shown in Fig. 2.1.

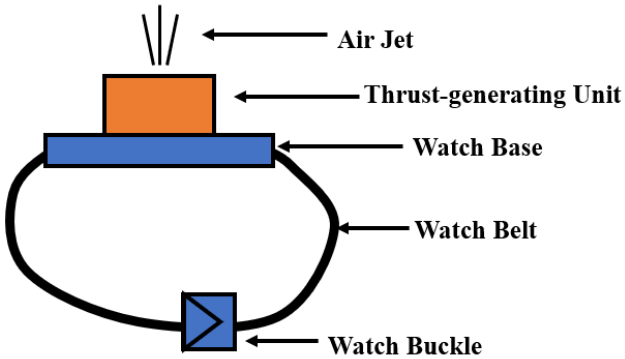

Fig. 2.1. The basic components of a flying watch.

The TGU is for generating controllable air thrusts that can cooperate with arm actuators. The attachment mechanism is composed of watch bases, watch belts, and watch buckles. The watch base is for connecting the TGU and watch belts. The watch belt should be adjustable for different link diameters of robotic arms and exchangeable in case of damage or unsuitable belt properties (e.g. length, friction, and material strength, etc.). The watch buckles enable fast deployment or allocation modification of flying watch. The watch base and watch belt need to withstand flying watch thrusts and provide enough friction to avoid sliding motion along the attached links.

2.2. Thrust Generating Unit Design

We show several example TGU design in Fig. 2.2. The arrows indicate possible thrust directions. The attachment mechanism is simply drawn as a blue watch belt since the details will be discussed in the next section.

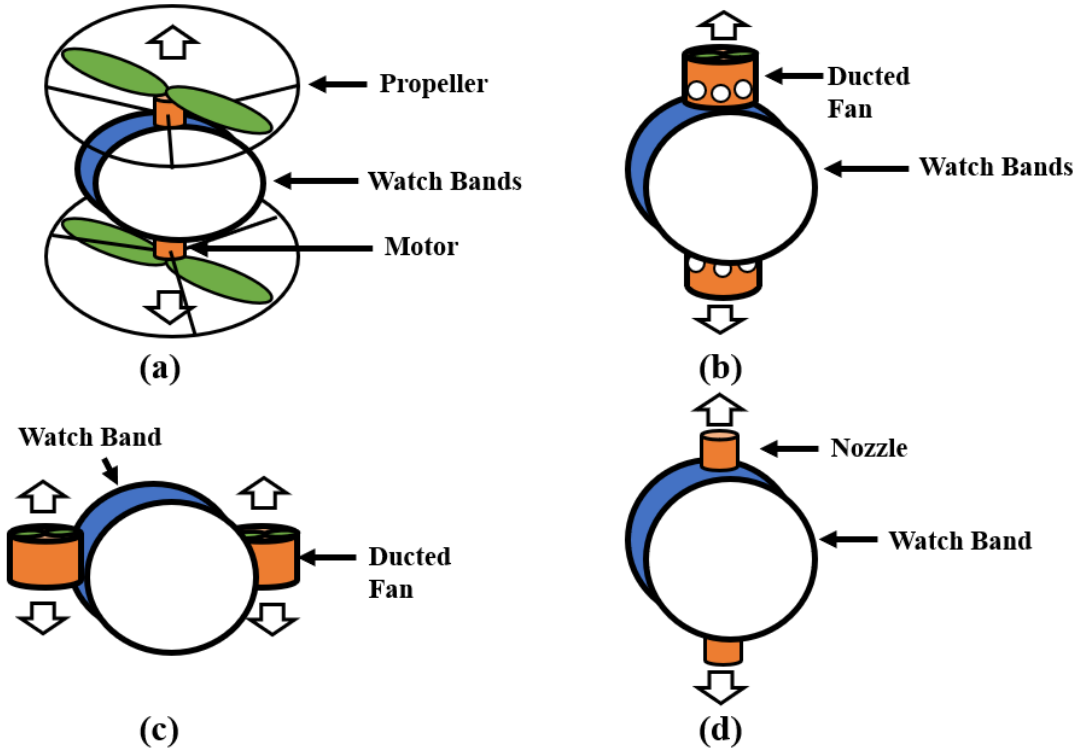

Fig. 2.2. Mechanisms of Thrust-generating Unit. This figure is modified from [32].

The TGU mechanisms can be classified based on their thrust generation principles as propeller TGU and propellerless TGU. Propeller TGUs use high-speed rotational motions of blades to generate thrusts. Propeller TGUs can be more specifically classified as ductless propeller TGUs (as shown in Fig. 2.2 (a)) and ducted fan TGUs (as shown in Fig. 2.2 (b), (c)) depending on whether ducts are installed. Compared with ductless propeller TGU, ducted fan TGU have the following advantages. (1) the duct is a safe shield that separate the high-speed propellers from the environment. (2) The duct improves propeller efficiency since it reduces propeller tip loss and avoids slipstream contraction [35]. (3) The duct can reduce noise [35]. However, it should also be noticed that the additional duct increases weight and cost. Please note that ductless propellers or ducted fans in practice may be designed to be efficient only in one thrust-generating direction. However, the thrust in the less efficient direction is still very

useful for enhancing an arm. In addition, it is also possible to design symmetrical ductless propellers or ducted fans that can generate bidirectional thrust with equal efficiency. Therefore, the design in Fig. 2.2 (a) and (c) are valid.

Propellerless TGUs generate thrusts by ejecting pressurized air (as shown in Fig. 2.2 (d)) and there is no moving part inside propellerless TGU. Compared with propeller TGUs, propellerless TGU are generally much more compact and lightweight.

The TGU arrangement on a flying watch can be classified as co-axial TGU arrangement and parallel TGU arrangement. In co-axial TGU arrangements, the thrust-generating directions of all TGUs coincide. In parallel TGU arrangements, the thrust-generating directions of all TGUs are parallel. The advantages and disadvantages of both arrangements can be seen in Table 2.1. The co-axial TGU arrangements help reducing watch size while the parallel TGU arrangements help improving watch efficiency.

Table 2.1. Advantages and Disadvantages of Different TGU Arrangements

	Coaxial TGU Arrangement	Parallel TGU Arrangement
Advantage	Reducing watch size when propeller TGUs are used since propellers share the same rotation axis.	Improved watch efficiency since the attached arm link does not obstruct thrusts.
Disadvantage	Reduced watch efficiency since the attached arm link obstructs thrusts.	Increasing watch size when propeller TGUs are used.

In this dissertation, we name flying watches based on their TGU mechanisms and arrangements (e.g. parallel ducted fan flying watch in Fig. 2.2 (c) and co-axial propellerless flying watch in Fig. 2.2 (d)).

The hardware system of propeller flying watches are shown in Fig. 2.3. The arm links are drawn using blue lines and the arm motors are drawn using orange cylinders. The PC needs to send thrusts commands (generated by an online or offline thrust planner) to microcontroller. Then the microcontroller converts thrust commends to PWM signals and send it to Electronic Speed Control (ESC) units. Then ESC regulates propeller rotation speeds of flying watches and thusly influence thrusts.

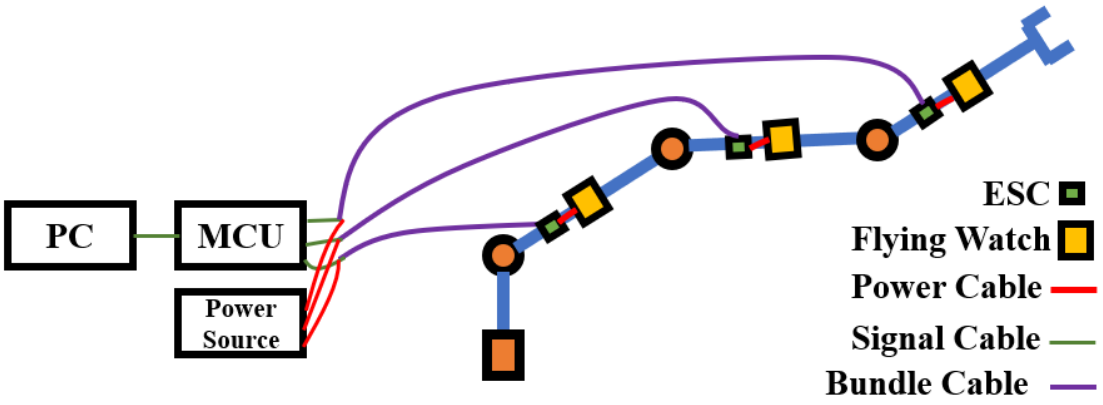

Fig. 2.3. The hardware system of propeller flying watches.

Propellerless TGU, as shown in Fig. 2.2 (d), has nozzles to directly eject pressurized air fed from a compressor near the arm base via air tubes. Each nozzle in Fig. 2.2 (d) is in charge of propulsion in one direction. Propellerless TGU has the following advantages. (1) Propellerless TGU is much safer since there is no high-speed rotating parts and no risk of sucking in objects. (2) Propellerless TGU is more lightweight and compact since heavy or large parts (motors, propellers, ESC, etc.) are removed. As a result, propellerless flying watches are suitable for enhancement of very light long robotic arms.

The hardware system of propellerless flying watches is shown in Fig. 2.4. An air compressor provides propellerless flying watch with pressurized air through air tubes. The pressure or air flow rate of the supplied air is controlled by a microcontroller and regulators. The PC calculates and sends thrust commands to the microcontroller.

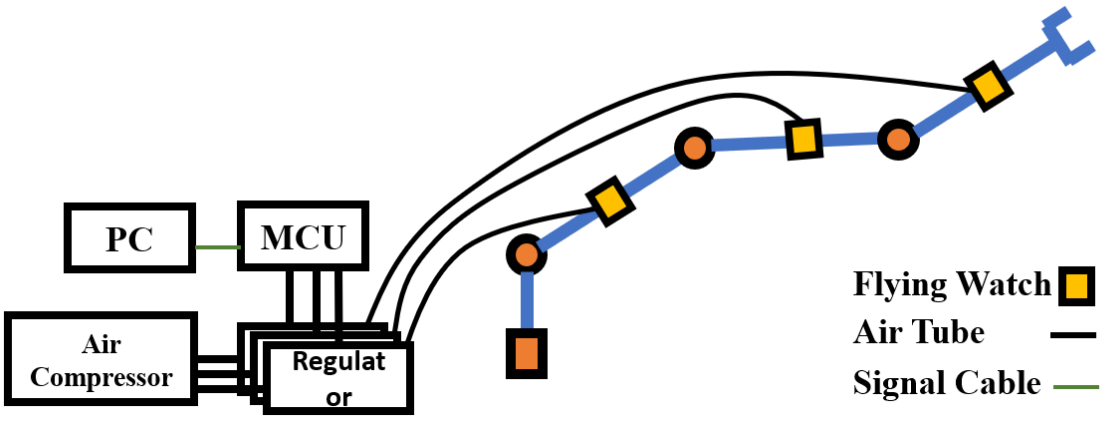

Fig. 2.4. The hardware system of propellerless flying watches. This figure is adapted from [33].

We can establish a theoretical thrust model for propellerless flying watch. Based on Newton's second and third law, the thrust of propellerless flying watch, s, can be expressed as follows [36].

$$s = \dot{m}_e v_e \tag{2.1}$$

In (2.1), $\dot{m}_e$ is the mass flow rate of the discharged air. v_e is the velocity of the discharged air. Since one control option is to regulate air flow rate Q, we rewrite (2.1) in term of Q.

$$s = \frac{\rho_{air} Q^2}{A} \tag{2.2}$$

In (2.2), ρ_{air} is the air density ($1.225 kg/m^3$ at 1013.25 hPa and $15°C$). A is the area of the nozzle. We can also write (2.2) in terms of difference of pressure inside and outside the flying watch (ΔP) as (2.4) using orifice flow equation (2.3).

$$Q = C_d A \left(\frac{2}{\rho_{air}} \Delta P\right)^{\frac{1}{2}} \tag{2.3}$$

In (2.3), C_d is the discharge coefficient, which depends on the shape of the nozzle and the direction of approaching flow.

$$s = 2C_d^2 A\Delta P \tag{2.4}$$

Equation (2.2) and (2.4) are very useful for determining the design parameters of propellerless TGU (such as nozzle size, flow rate, pressure difference, etc.).

2.3. Thrust Generating Unit Experiments

I did thrust experiments using the equipment shown in Fig. 2.5 to understand the maximum thrust of a propeller TGU. The equipment follows the mentioned system setup in Fig. 2.3 except the thrust commands is transmitted remotely by radio for safety reasons and the PC is only for data recording. The TGU is composed of a Tarot 4114 motors and Tarot 1555 propellers. The Tarot 4114 motor is a high power brushless motor for UAVs (maximum

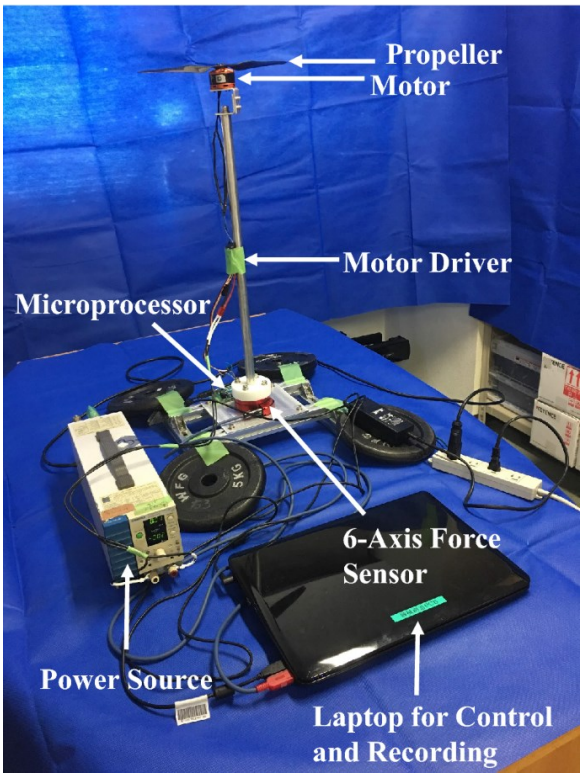

Fig. 2.5. The equipment for thrust experiment of propeller thrust-generating unit. This figure is adapted from [16].

power=423 W). It has a maximum rated voltage of 25.2 V and maximum rated thrust of 26.0 N (with a 15 inch propeller of 5.5 inch pitch). Tarot 1555 is a carbon fiber UAV propeller with a 15 inch diameter and 5.5 inch pitch. The propeller thrust is controlled by the duty ratio of PWM signal given to the motor driver. The reaction force and torque are measured by a DynPick 6-axis force sensor from WACOH Tech inc. Also the voltage given to the motor driver can influence the thrust.

I tested the maximum thrusts under different voltage and found when working at the maximum voltage (25.2 V), the motor easily overheats and loses speed due to heat protection. I finally selected 14.8 V for flying watches. With this voltage, the propeller can continuously generate a maximum thrust of 9.7 N with a reaction torque of 0.21 Nm. The reaction torque of one propeller is not negligible, which justifies our design of canceling reaction torque using two counter-rotating propellers in Fig. 2.2 (a). With two propellers, a watch can approximately double the maximum thrust of TGU and generate 19.4 N thrust. Although the actual propeller thrust is only 37% of the rated maximum thrust due to motor overheating, we will see later in Section 2.5 that the TGU thrust is enough to build a flying watch prototype with reasonable thrust-to-weight ratio.

I did thrust experiment using the equipments shown in Fig. 2.6 to understand the relation of the maximum thrust of a propellerless TGU with the air tube length and diameter. An ANEST IWATA SLP-07EED compressor is used to pump air into a 60 L ANEST IWATA SAT-60C-100 air tank. The compressor also contains a 5 L air tank inside. The compressor is set to pump air if the pressure in the contained air tank is below 0.6 MPa and to stop pumping air if the pressure in the contained air tank is beyond 0.7 MPa. The design of the TGU is shown in Fig. 2.7. The TGU has a 4 mm diameter inlet hole glued with air tube and a 3 mm diameter nozzle for ejecting air. The inlet hole and outlet nozzle are connected by a small air chamber. The TGU and watch base are designed as one piece in order to be lightweight and compact.

The TGU can be 3D printed as one part. The TGU is temporary glued to a weight meter to measure reaction thrusts.

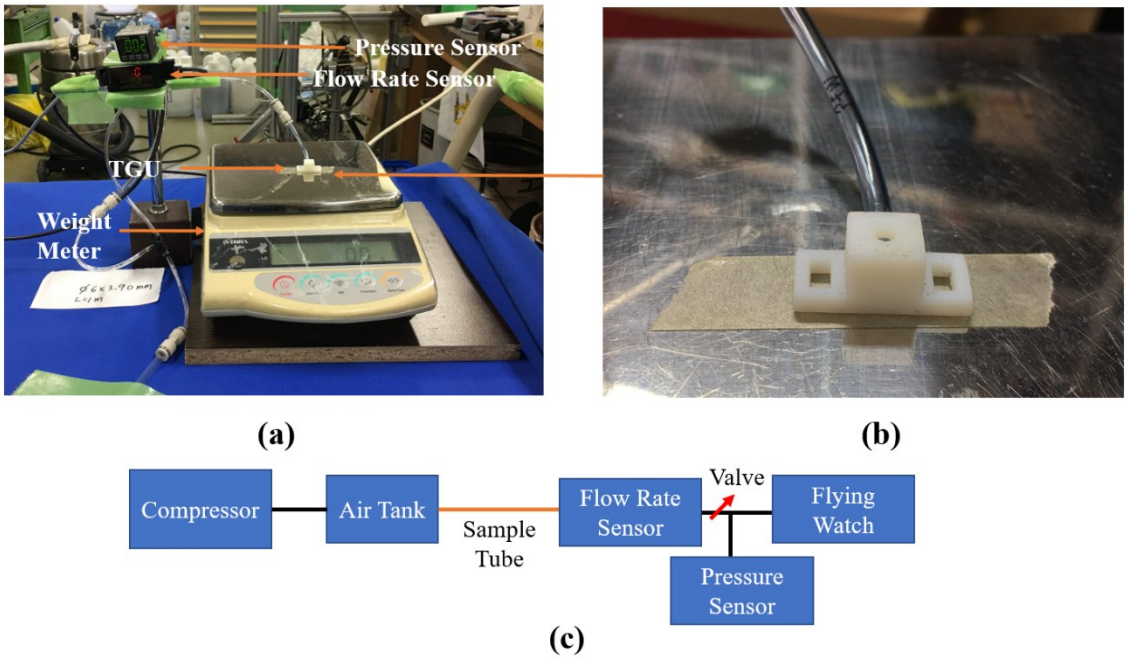

Fig. 2.6. The equipment for thrust experiment of propellerless thrust-generating unit. a. the whole equipment. b. magnified view of propellerless thrust-generating unit. c. structure of the equipment.

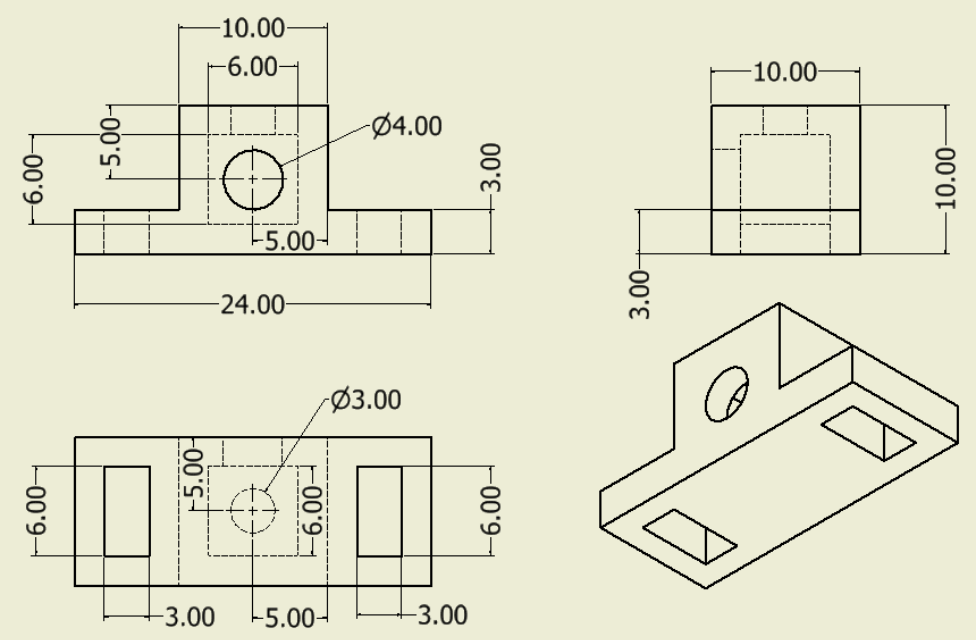

Fig. 2.7. Design of propellerless thrust-generating unit.

During the experiment, a sample tube with a certain length and diameter is installed. Then the valve is turned on and the thrust, flow rate, and pressure near flying watch inlet hole from 3 second to 5 second are recorded. Since the compressor can regulate the initial source pressure to be 0.6-0.7 MPa and the 60 L air tank can compensate source pressure, I assumed that the source pressure from 3s to 5s (a period very shortly after flying watch discharge) is approximately 0.6-0.7 MPa. Sample air tubes with lengths of 1 m, 4 m, 7 m, and 10m are tested. For each air tube length, the tube inner diameters of 2.5 mm, 4 mm, and 5 mm are tested. The maximum pressure of each sample tube is 0.8 MPa. The mass of sample tubes are 9g/m (inner diameter=2.5 mm), 19g/m (inner diameter=4 mm), and 36g/m (inner diameter=5 mm). The experimental results are shown in Fig. 2.8 and Table 2.2. Please note the volume flow rate in Table 2.2 is at 20 $°C$ and 101.3 kPa.

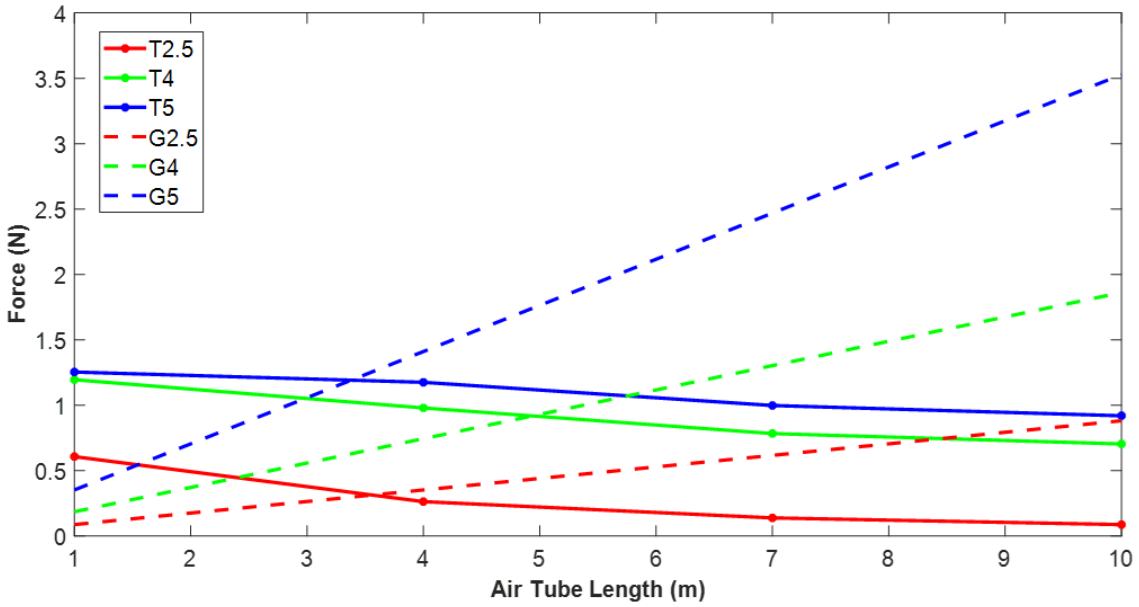

Fig. 2.8. Pure thrusts and gravity of propellerless flying watch.

In Fig. 2.8, thrust lines T5, T4, and T2.5 are pure flying watch thrusts when 5 mm, 4 mm, and 2.5 mm inner diameter sample tubes are used. Pure thrust means the flying watch gravity is excluded. The gravity of the propellerless flying watch prototype in Fig. 2.14 is used. Gravity lines G5, G4, and G2.5 are the gravity of a single sample air tube with inner diameter of 5 mm,

4 mm, and 2.5 mm. Supposing an arm is fully stretched horizontally and the watch is attached with the vertical thrust direction, the flying watch induced torque on the most proximal joint is the air tube length times watch thrust, which is the rectangle area defined by a point on thrust lines. Similarly, the air tube center of gravity is at the arm middle point and two air tubes of the same length are necessary for generating bidirectional thrust. As a result, the gravity induced torque on the most proximal joint is single air tube gravity times single air tube length, which is the rectangle area defined by a point on gravity lines. Therefore, the intersection point of thrust and gravity lines of the same inner diameter gives the air tube length at which gravity effect equals thrust effect. This air tube length is called maximum beneficial length. When the air tube length is smaller than the maximum beneficial length, the propellerless flying watch is beneficial for arm enhancement. When the air tube length is larger than the maximum beneficial length, the propellerless flying watch itself will be a load. At a certain air tube length, the vertical difference between a thrust line and corresponding gravity line is called beneficial thrust margin, which describes the pure enhancement ability of a propellerless flying watch excluding gravity effects.

Table 2.2. Results of Propellerless Flying Watch Thrust Test

Sample Tube Length (m)	Diameter (mm)	Thrust (g)	Flow Rate (L/min)	Pressure (MPa)
1	8x5	132.9	165	0.457
1	6x4	126.9	179	0.443
1	4x2.5	66.9	124	0.288
4	8x5	124.9	177	0.438
4	6x4	104.9	158	0.387
4	4x2.5	31.8	85	0.180
7	8x5	106.8	159	0.389
7	6x4	84.9	141	0.337
7	4x2.5	19.1	68	0.129
10	8x5	98.8	153	0.372
10	6x4	76.8	133	0.314
10	4x2.5	13.9	58	0.105

We can see the maximum beneficial lengths of air tube inner diameter of 5 mm, 4mm, and 2.5 mm are respectively 3.3 m, 4.9 m, and 3.6 m. For the tested flying watch, 4 mm air tube

diameter is recommended as it has the largest maximum beneficial length and beneficial thrust margin. Please note the concepts of maximum beneficial length and beneficial thrust margin are only meaningful when the propellerless flying watch is used to counteract gravity. If we only want to counteract horizontal environmental force, what matters is the maximum watch thrust.

From the pressure difference and flow rate in Table 2.2, the discharge coefficient C_d is estimated to be 0.32 ± 0.16. We can also see the flow rate is generally below 200 L/min. Many compressors in the market can continuously pump air at this rate. For example, Anest Iwata TFP37CF-10M5, Fuji compressor W37-P, and AIRWAVE SP-3300.

2.4. Attachment Mechanism Design

Similar to wristwatch, the attachment mechanism of a flying watch is composed of watch bases, watch belt, and watch buckle. The watch base needs to connect both TGU and watch belts as shown in Fig. 2.9. For propeller TGU, the watch base is connected with TGU using bolts. For propellerless TGU, the watch base and TGU can be designed and manufactured as one part. A watch base has two open slots for connecting watch belts, which is the same as wristwatch.

Wristwatch has many types of watch belts. Three major types are spring bar belt, Zulu belt, and NATO belt as shown in Fig. 2.9. However, wristwatch belt cannot be directly used for flying watch because of the following reasons. (1) wristwatch belt designs only assume one watch case. However, a flying watch usually have two watch bases for larger thrusts or bidirectional thrusts. (2) Preventing wristwatch from slide along arm link is not a major design consideration. However, a flying watch must be tightly fixed to arm link. In order to handle

those two differences, in the following, we propose three kinds of flying watch belts inspired by wristwatch belts as shown in Fig. 2.9.

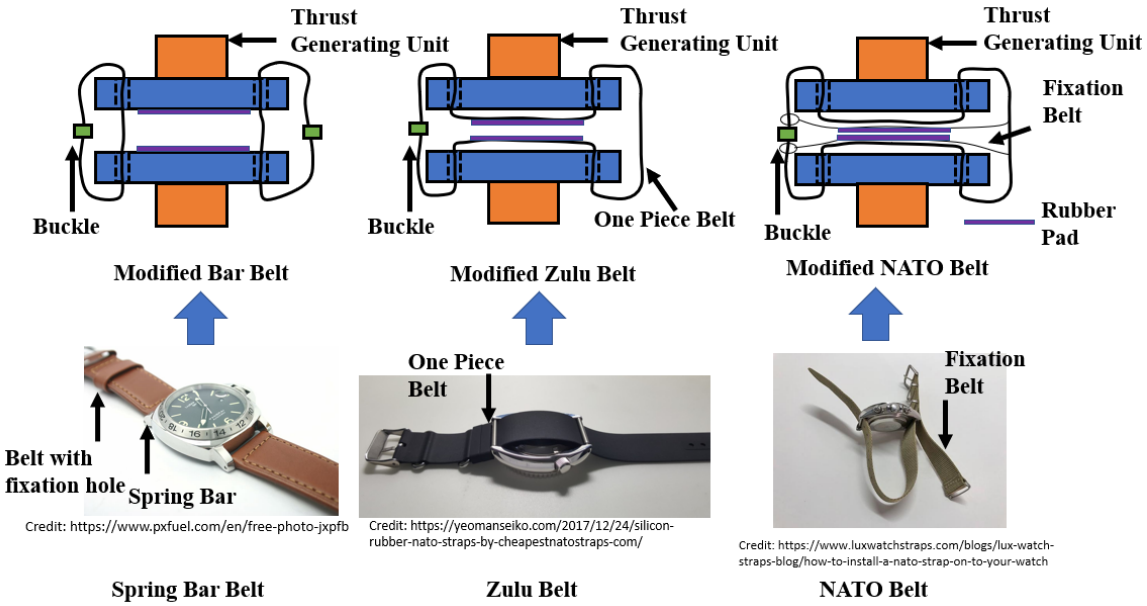

Fig. 2.9. Flying watch belt designs. This figure is adopted from [32].

Spring bar belt of wristwatch used an extractable spring bar to fix watch belt with fixation hole as shown in the left part of Fig. 2.9. The spring bar forms a hinge together with the watch base and watch belt. In modified bar belt, the fixation bar is not removable and the watch belt forms an openable loop going through the fixation bars of the two watch bases. Similar to spring bar belt, the watch base and watch belt still forms a hinge structure. Two rubber pads are glued to the back of watch bases to prevent sliding along the attached arm link. The advantage of modified bar belt is that the length of two watch belt can be independently adjusted. Also, the rubber pads and watch belts are separated so that the rubber pads do not influence watch belt adjustment. The disadvantage is that installation and removal of a flying watch requires one watch belt to be removed.

Zulu watch belt of wristwatch is a one-piece watch belt that does not require removable fixation bars. The sliding of watch case on watch belt is loosely prevented by friction. A modified Zulu belt for flying watch is still a one-piece belt that goes through four fixation bars

as shown in the middle of Fig. 2.9. Two removable rubber pads are attached on the watch belt to prevent arm link sliding. The advantage is that the installation and removal of a flying watch does not require removal of watch belt. The disadvantage is that the rubber pads on the belt may disrupt watch belt adjustment. Therefore, the rubber pads may need to be adjusted before adjusting watch belt.

NATO watch belt of wristwatch is also a one-piece watch belt that does not require removable fixation bars. As an improvement to Zulu watch belt, NATO watch belt has an additional fixation belt to fix watch cases. A modified NATO belt is still a one-piece belt that goes through four fixation bars as shown on the right of Fig. 2.9. Two fixation belts are used to fix the two watch bases. Also, two removable rubber pads are attached to prevent arm link sliding. Except for better watch base fixation, NATO belt and Zulu belt have similar advantages and disadvantages.

Regarding flying watch buckles, many existing buckle mechanisms, such as loop & hoop tape, lashing strap buckle, and Tri-glide buckle, as shown in Fig. 2.10 can be directly applied.

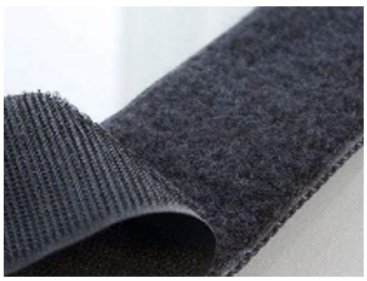

https://www.amazon.com/Diesel-Sticky-Back-Velcro-Fastener-Kwik-Stik/dp/B07GDTP8SF

Loop & Hook Tape

https://www.tunnelvisionhoops.com/lashing-strap-cam-buckle/

Lashing Strap Buckle

https://commons.wikimedia.org/wiki/File:Small_bra_strap_with_metal_tri-glide_slide.jpg

Tri-glide buckle

Fig. 2.10. Possible flying watch buckles.

The major load on the attachment mechanism is the thrust-induced reaction pulling force. Suppose (1) two TGUs are attached on a watch and (2) the TGU reaction forces are mainly counteracted by the supporting force from the arm link instead of friction force. For co-axial TGU arrangements, since the thrust-induced reaction force of one of the TGU is supported by

the arm link, we need to ensure that $\min(f_{belt}^{max}, f_{buckle}^{max}) \geq \frac{T_{TGU}^{max}}{2} s_{safe}$, where f_{belt}^{max} and f_{buckle}^{max} are respectively the maximum pulling material strength of watch belt and watch buckle and $s_{safe} > 1$ is a safety factor. For parallel TGU arrangement, since all thrust-induced reaction pulling forces are loaded on the watch belt, we need to ensure $\min(f_{belt}^{max}, f_{buckle}^{max}) \geq T_{TGU}^{max} s_{safe}$. Those pulling material strength requirements can be easily tested through pull test of watch belts and watch buckles using a force gauge.

In addition to pulling material strength requirements, appropriate tension force is necessary to secure enough friction to counteract watch gravity so that the watch does not slide along the arm link. In other words, $f_{watch}^{max} > G_{watch} s_{safe}$, where f_{watch}^{max} is the maximum friction force between the watch and link and G_{watch} is the watch gravity. In practice, the friction requirement can be tested simply by pulling the watch along the link using a force gauge and check whether the friction is larger than $G_{watch} s_{safe}$.

2.5. Flying Watch Prototypes

A flying watch prototype composed of propeller TGUs and modified bar belts are shown in Fig. 2.11. The TGU is exactly the same as the one used for the thrust test shown in Fig. 2.5. The watch belts are made of double side loop & hook band. Therefore, the maximum thrust is 19.4 N. The weight of the prototype is 450 g. The propeller diameter is 381 mm. Since ESC units also need to be attached closely to the flying watch, the total additional weight due to a

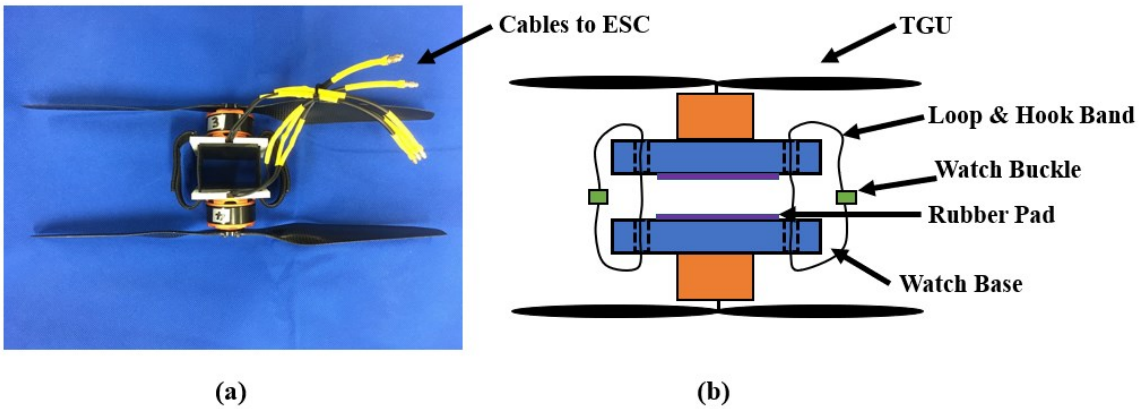

Fig. 2.11. Propeller flying watch prototype (propeller TGU + modified bar belt). a. Photo. b. design. This figure is adapted from [16].

flying watch is 542 g. Therefore, this propeller flying watch achieve a thrust-to-weight ratio of 3.65.

We can change the attachment mechanism of the prototype in Fig. 2.11 to modified Zulu belts (shown in Fig. 2.12 with a weight of 460g) and modified NATO belts (shown in Fig. 2.13 with a weight of 465g). In both situations, the watch belts are connected with rubber pads using loop & hook tapes. In the NATO belt, the fixation belt is connected with the main belt using loop and hook tapes.

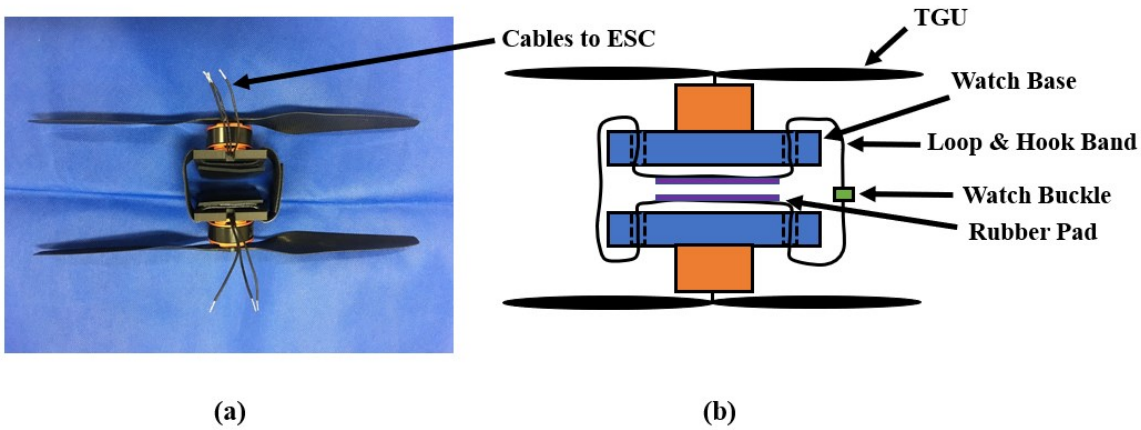

Fig. 2.12. Propeller flying watch prototype (propeller TGU + modified Zulu belt). a. Photo. b. design.

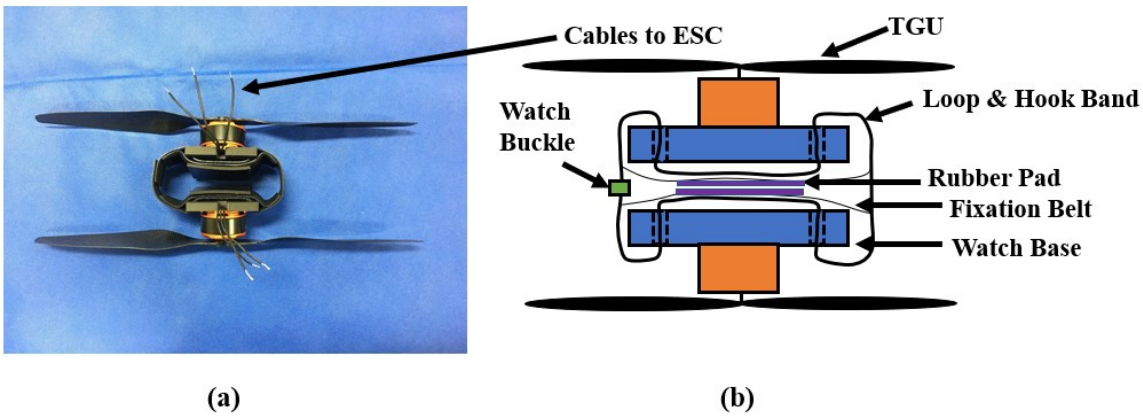

Fig. 2.13. Propeller flying watch prototype (propeller TGU + modified NATO belt). a. Photo. b. design.

Another propellerless flying watch prototype composed of two propellerless TGUs and a modified Zulu belt is shown in Fig. 2.14. Each TGU is in charge of generating thrust in one direction and two air tubes are used for supplying air. The total weight of that prototype is 4.9 g.

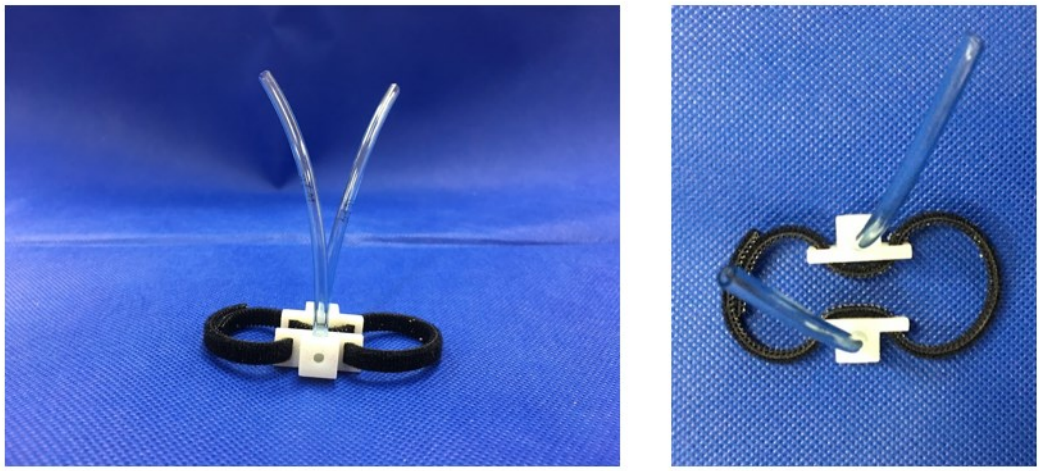

(a) (b)

Fig. 2.14. Propellerless flying watch prototype (propellerless TGU + modified Zulu belt). a. front view. b. top view.

2.6. Flying Watch Selection and Application Scope

Until now, several kinds of TGUs and attachment mechanisms and flying watch prototypes are introduced. As mentioned at the beginning of this Chapter, there could be flying watches with different sizes, mechanisms manufactured for different robotic arms and missions. However, how to properly select a flying watch for a mission or understanding the application scope of a flying watch is not clear. This Section solves those problems by proposing three flying watch selection factors.

The first factor, called Actuator Enhancement Factor (f_{ae}) is defined as follows.

$$f_{ae} = \frac{s_c l_{arm}}{\tau_a} \tag{2.5}$$

In (2.5), s_c is the maximum thrust of a flying watch, named characteristic thrust. l_{arm} is the length of a robotic arm. τ_a is the maximum actuator load exerted on arm joints. Actuator Enhancement Factor describes how much a flying watch can enhance the joint actuator.

The second factor, called Reaction Counteraction Factor (f_{rc}), is defined as follows.

$$f_{rc} = \frac{s_c l_{arm}}{\tau_r} \tag{2.6}$$

In (2.6), τ_r is the maximum torque due to reaction force from the environment including gravity. Reaction Counteraction Factor describes how much external reaction forces flying watch can counteract. In some situations, the payload is much smaller than the arm gravity and the main duty of actuator is to counteract gravity. Since $\tau_a \approx \tau_r = m_{arm} g l_{arm}/2$, the actuator enhancement factor and reaction factor can be approximated as $f_{ae} \approx f_{rc} = 2s_c/m_{arm}g$, where m_{arm} is the arm mass afforded by actuators and g is gravitational acceleration.

The third factor, called Workspace Factor (f_w), is defined as follows.

$$f_w = 1 - \frac{2}{\pi}\arcsin\left(\frac{2l_c}{l_{link}}\right) \tag{2.7}$$

In (2.7), l_c is the characteristic length of a flying watch, which is defined as the radius of the smallest circumscribed sphere of a flying watch when the watch is attached to an arm link. The circumscribed circle determines the boundary of a flying watch and its radius describes the size of the flying watch. For a propeller flying watch whose propeller is significantly longer than other parts, the characteristic length can be approximated as the radius of propeller. l_{link} is the length of an attached arm link. We can notice that f_w is always between 0 and 1.

The meaning of f_w is explained by Fig. 2.15. It is assumed that the flying watch is attached at the middle point of the arm link. When the circumscribed sphere (boundary of flying watch) touch the arm link, there is a potential threat of collision. We can calculate that at that moment, the obstruction angle $\theta_{link} = \arcsin(\frac{2l_c}{l_{link}})$. In the worst case, $\theta_{link} = \frac{\pi}{2}$. Therefore, we can understand that f_w describes the movable angle of arm links when a flying watch is attached. Or in other words, f_w describes the size of the arm workspace after the flying watch is attached.

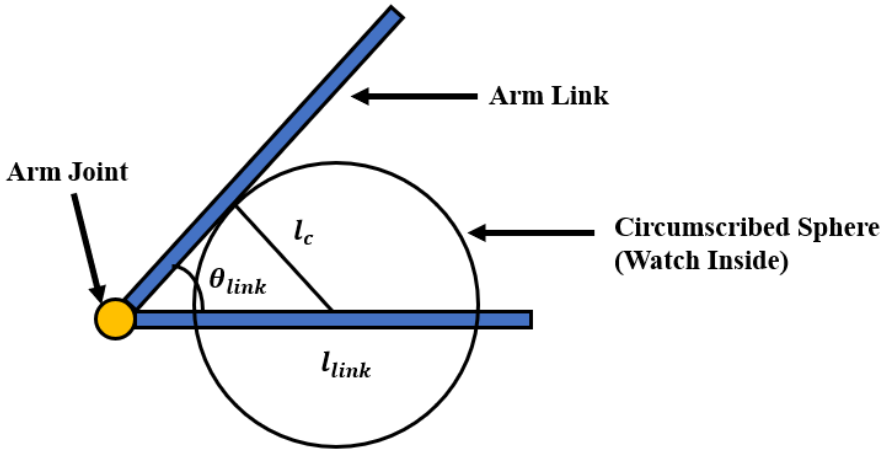

Fig. 2.15. Meaning of Workspace Factor.

After understanding the meaning of those factors, we can first understand higher factors means better corresponding performance. In practice, how high for those factors is enough is subject to the judgement of the users or designers. However, the author recommends that a reasonable flying watch choice should at least satisfy $f_{ae} \geq 0.1, f_{rc} \geq 0.1, f_w \geq 0.5$. Under those thresholds, flying watch actuation effect is more than 10 % of actuator effect and resistance effect and obstruction angle is smaller than 45 °. And the following relation should be satisfied to ensure the summation of flying watch effect and actuator effect is larger than resistance effect ($\tau_a + N_f s_c l_{arm} \geq \tau_r$). N_f is the number of flying watches to be attached.

$$\frac{1}{f_{ae}} + N_f \geq \frac{1}{f_{rc}} \tag{2.8}$$

From (2.8), we can further understand that when $f_{rc} > f_{ae}$, the flying watches will operate in the supportive enhancement situation, where the arm actuators alone can handle the reaction forces from the environment and the role of flying watches is further enhancing the arm strength for unexpected disturbances and improving arm robustness by increasing redundancy. When $f_{rc} < f_{ae}$, the flying watch will operate in the critical enhancement situation, where the arm actuators alone may not handle the reaction forces from the environment and flying watch failure may result in critical mission failure.

Equation (2.8) is only a necessary condition of an appropriate flying watch for rough initial flying watch selection. It is recommended that the users do simulations based on flying watch dynamics (will be introduced in Chapter 4) to further determine whether flying watches can properly work or not.

In the following, we will demonstrate the application of those three selection factors in two examples.

Firstly, let us determine what kind of flying watch is a reasonable choice for enhancing an existing arm in our lab, called Planar Inspection Arm (PIA), as shown in Fig. 2.16. PIA was originally a planar arm for inspection of completely horizontal plane using end effector and the

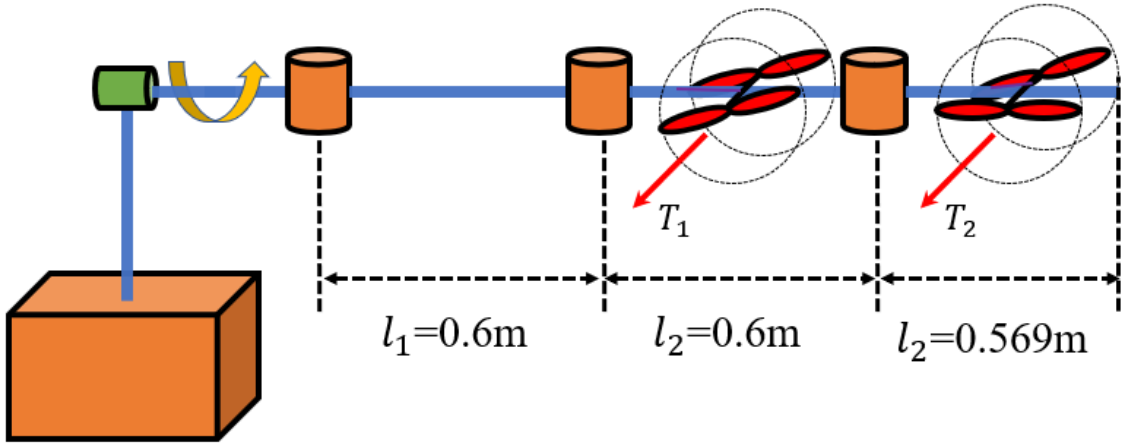

Fig. 2.16. Design of Planar Inspection Arm. This figure is from [34].

arm motors cannot actuate the arm when the workspace is a tilted plane. To solve this problem, we want to attach flying watches so that the workspace of PIA can be extended to tilted plane with slope angle within 30 °. We assume two flying watches will be deployed ($N_f = 2$). Each joint of PIA has a MAXON 267121 motors with maximum continuous torque is 25.5 mNm and a harmonic drive with gear ratio of 100. Therefore, $\tau_a = 2.55Nm$. The arm length is $l_{arm} = 1.77m$ and the arm mass is 3.46 kg. When horizontally stretched, the gravity torque on base joint is τ_r =15.0 Nm. We can solve from (2.5)-(2.8) and the recommended thresholds of selection factors that $s_c \geq 0.85N$ and $l_c \leq 0.21$ m.

We know from thrust experiments that the flying watch prototype in Fig. 2.11 has maximum thrust of 19.4 N and characteristic length of 0.19 m (approximately equals the propeller radius as mentioned). Its characteristic length and thrust falls within the desired range. We can calculate that $f_{ae} = 13.5 > 0.1$, $f_{rc} = 2.3 > 0.1$, $f_w = 0.56 > 0.5$, and (2.8) holds. We can notice that $f_{rc} < f_{ae}$, which means the flying watches will work in critical enhancement situation. Based on (2.5)-(2.8) and corresponding thresholds, we can choose the flying watch prototype in Fig. 2.11 for the PIA mission.

Secondly, let us calculate the application scope of the propellerless flying watch prototype shown in Fig. 2.14. We assume only one propellerless flying watch is deployed. Since the size of the watch is almost neglectable, we ignore workspace factor. We used the watch thrust with 10 m air tube with inner diameter of 4 mm and assume the propellorless flying watch is attached 10 m away from arm base. In such situation, $l_{arm} = 10\ m$. From $f_{rc} \geq 0.1$ and $f_{ae} \geq 0.1$, we can calculate that $m_{arm} \leq 1.536\ kg$, $\frac{l_{arm}}{\tau_a} \geq 0.13$, and $\frac{l_{arm}}{\tau_r} \geq 0.13$. We can see the arm should be very light. The Giacometti arm in Fig. 1.1 with a weight of 0.94 kg satisfies the weight condition. In fact, since the arm is filled with helium, the actual weight that actuators need to afford is much less than 0.94 kg. However, our lab found that a major problem for

Giacometti arm is wind disturbance due to heat circulation, even though Giacometti arm is only for indoor operation. The arm is very hard to control under such wind disturbance. Wind load (aerodynamic drag) can be calculated by drag equation $F_w = \frac{1}{2}\rho_{air} v^2 C_{dr} A$. C_{dr} is the drag coefficient and can be approximated as 1.2 for a cylinder [37]. Assuming the heat circulation wind speed is v =0.4 m/s, we can calculate that $\tau_r = 7.06$ Nm. The artificial muscle of Giacometti arm can generate a maximum torque of τ_a =0.3 Nm. We can calculate that for Giacometti arm, $f_{ae} = 25.1 > 0.1$, $f_{rc} = 1.1 > 0.1$, and (2.8) holds. Therefore, the propellerless flying watch prototype in Fig. 2.14 is a reasonable choice for the Giacometti arm.

2.7. Flying Watch Dynamics

Up to now, the concept, design, and selection of flying watch are introduced. But how will an arm attached with flying watch move? This Section answers this question by deriving the Equation of Motion (EoM) of a flying watch enhanced arm. The EoM is essential for flying watch simulations. Also, we will see later that the EoM is a theoretic foundation for flying watch attachment allocation customization (Chapter 3) and flying watch thrust planning (Chapter 4).

Let us suppose that we have a fully actuated K DoF arm attached with N_f flying watches. We start from the Lagrange's Equation of Motion [38].

$$\frac{d}{dt}\left(\frac{\partial L}{\partial \dot{\boldsymbol{q}}_k}\right) - \frac{\partial L}{\partial \boldsymbol{q}_k} = \boldsymbol{Q}_k \tag{2.9}$$

In (2.9), Lagrangian $L = E - U$. E is the total kinetic energy of the arm. U is the total potential energy of the arm. t is time. $\boldsymbol{q}$ is the generalized coordinate describing arm configuration and its k th component is $\boldsymbol{q}_k$. $\boldsymbol{Q}$ is the generalized force and its k th component is $\boldsymbol{Q}_k$.

The virtual forces $\boldsymbol{Q}$ in (2.9) need to be substituted with actual forces or torques in order to make (2.9) more useful. The relation of virtual forces and actual forces can be found through the definition of virtual work as follows.

$$\boldsymbol{\tau}^T \delta \boldsymbol{q} + \boldsymbol{F}_e^T \delta \boldsymbol{p} + \sum_k \boldsymbol{T}_k^T \delta \boldsymbol{r}_k = \boldsymbol{Q}^T \delta \boldsymbol{q} \tag{2.10}$$

$\boldsymbol{\tau}$ is the actuator load vector, whose real dimensions depend on the actuator mechanism (e.g. Nm for revolute actuators and N for prismatic actuators). Please note that we will use bold font to denote vector or matrix throughout this dissertation. $\boldsymbol{F}_e$ is the external reaction force and torque on the end effector. $\boldsymbol{p}$ is the position and orientation of the end effector. $\boldsymbol{T}_k$ is the thrust generated by the k th flying watch. $\boldsymbol{r}_k$ is the position vector of the k th flying watch. To simplify (2.10), we need to substitute $\delta \boldsymbol{p}$ and $\delta \boldsymbol{r}_k$ with changes of generalized coordinates $\delta \boldsymbol{q}$. This can be done using the following kinematics relations.

$$\delta \boldsymbol{p} = \boldsymbol{J} \delta \boldsymbol{q} \tag{2.11}$$

$$\delta \boldsymbol{r}_k = \boldsymbol{J}_k^f \delta \boldsymbol{q} \tag{2.12}$$

$\boldsymbol{J}$ and $\boldsymbol{J}_k^f$ are the Jacobian matrices of the end effector and the k th flying watch. Substituting $\delta \boldsymbol{p}$ and $\delta \boldsymbol{r}_k$ in (2.10) using (2.11) and (2.12), (2.10) can be simplified as follows.

$$\boldsymbol{\tau} + \boldsymbol{J}^T \boldsymbol{F}_e + \sum_k \boldsymbol{J}_k^{fT} \boldsymbol{T}_k = \boldsymbol{Q} \tag{2.13}$$

The kinetic energy in (2.9) can be written as follows.

$$E = \frac{1}{2} \dot{\boldsymbol{q}}^T \boldsymbol{M} \dot{\boldsymbol{q}} \tag{2.14}$$

$\boldsymbol{M}$ is the manipulator inertia tensor. Substituting E and $\boldsymbol{Q}$ in (2.9) using (2.13) and (2.14), (2.9) can be written as follows.

$$\boldsymbol{M}(\boldsymbol{q}) \ddot{\boldsymbol{q}} + \boldsymbol{h}(\boldsymbol{q}, \dot{\boldsymbol{q}}) - \boldsymbol{J}^T(\boldsymbol{q}) \boldsymbol{F}_e - \sum_k \boldsymbol{J}_k^{fT}(q) \boldsymbol{T}_k + \boldsymbol{g}(\boldsymbol{q}) = \boldsymbol{\tau} \tag{2.15}$$

In (2.15), to simplify the expression, we made the following definitions. The k th component of the velocity term $\boldsymbol{h}$ is as follows.

$$\boldsymbol{h}_k(\boldsymbol{q}, \dot{\boldsymbol{q}}) = \sum_{ij} \left(\frac{\partial \boldsymbol{M}_{kj}}{\partial \boldsymbol{q}_i} - \frac{1}{2}\frac{\partial \boldsymbol{M}_{ij}}{\partial \boldsymbol{q}_k}\right) \dot{\boldsymbol{q}}_i \dot{\boldsymbol{q}}_j \tag{2.16}$$

And the gravity term is as follows.

$$\boldsymbol{g}(\boldsymbol{q}) = \nabla U(\boldsymbol{q}) \tag{2.17}$$

Since a flying watch is rigidly attached to the arm, the thrust from the kth flying watch can be written as follows.

$$\boldsymbol{T}_k = \mathrm{s}_k \boldsymbol{a}_k(\boldsymbol{q}). \tag{2.18}$$

s_k and $\boldsymbol{a}_k$ are the scale and the unit direction vector of the thrust (minus sign of s_k indicates the thrust direction is opposite to $\boldsymbol{a}_k$). We can substitute $\boldsymbol{T}_k$ in (2.15) using (2.18) and obtain the following

$$\boldsymbol{M}(\boldsymbol{q})\ddot{\boldsymbol{q}} + \boldsymbol{h}(\boldsymbol{q}, \dot{\boldsymbol{q}}) - \boldsymbol{J}^T(\boldsymbol{q})\boldsymbol{F}_e - \sum_k \mathrm{s}_k \boldsymbol{J}_k^{fT}(q)\boldsymbol{a}_k(\boldsymbol{q}) + \boldsymbol{g}(\boldsymbol{q}) = \boldsymbol{\tau} \tag{2.19}$$

To further simplify (2.19), we can define an attachment style matrix as following.

$$\boldsymbol{R}(\boldsymbol{q}) = [\boldsymbol{J}_1^{fT}(\boldsymbol{q})\boldsymbol{a}_1(\boldsymbol{q}), \dots, \boldsymbol{J}_k^{fT}(\boldsymbol{q})\boldsymbol{a}_k(\boldsymbol{q}), \dots, \boldsymbol{J}_N^{fT}(\boldsymbol{q})\boldsymbol{a}_N(\boldsymbol{q})] \tag{2.20}$$

And (2.19) is simplified as following.

$$\boldsymbol{M}(\boldsymbol{q})\ddot{\boldsymbol{q}} + \boldsymbol{h}(\boldsymbol{q}, \dot{\boldsymbol{q}}) - \boldsymbol{J}^T(\boldsymbol{q})\boldsymbol{F}_e - \boldsymbol{R}(\boldsymbol{q})\boldsymbol{s} + \boldsymbol{g}(\boldsymbol{q}) = \boldsymbol{\tau} \tag{2.21}$$

In (2.21), $\boldsymbol{s} = [\boldsymbol{s}_1, \dots \boldsymbol{s}_N]^T$ is the collection of thrust magnitudes of all N_f flying watches. (2.19) is EOM of a fully actuated arm with N_f flying watch attached.

Equation (2.21) is different from typical robotic arm EoM in that it has an additional term $-\boldsymbol{R}(\boldsymbol{q})\boldsymbol{s}$ that represents the effect of a group of flying watches to actuator loads. $\boldsymbol{R}$, the attachment style matrix, is a function of generalized coordinates $\boldsymbol{q}$ parameterized by the attachment allocation parameters (the positions and orientations of flying watches referring to

local frames of arm links). It incorporates all the information about the attachment position and orientation of flying watches. $\boldsymbol{s}$, on the other hand, incorporates all information about thrust magnitudes. Now we have understood the dynamics of flying watch in general cases. In quasistatic situations, (2.21) can be simplified as

$$-\boldsymbol{J}^T(\boldsymbol{q})\boldsymbol{F}_e - \boldsymbol{R}(\boldsymbol{q})\boldsymbol{s} + \boldsymbol{g}(\boldsymbol{q}) = \boldsymbol{\tau} \tag{2.22}$$

Since different arm actuators may have different specifications, it is necessary to normalize joint loads before comparing them. Normalized joint loads is defined as $\tilde{\boldsymbol{\tau}} = \boldsymbol{H}\boldsymbol{\tau}$, where $\boldsymbol{H} = diag(1/\tau_{p1}, \dots, 1/\tau_{pK})$ is the normalization matrix and $\tau_{p1}, \dots, \tau_{pK}$ are the maximum permitted loads of the K joints. When all arm actuators have the same specification, for simplicity, we can make $\boldsymbol{H}$ an identity matrix. By multiplying both sides of (2.22) with $\boldsymbol{H}$, and defining $\tilde{\boldsymbol{J}} = \boldsymbol{J}\boldsymbol{H}$, $\tilde{\boldsymbol{R}} = \boldsymbol{H}\boldsymbol{R}$, and $\tilde{\boldsymbol{g}} = \boldsymbol{H}\boldsymbol{g}$, we can obtain the follows.

$$-\tilde{\boldsymbol{J}}^T(\boldsymbol{q})\boldsymbol{F}_e - \tilde{\boldsymbol{R}}(\boldsymbol{q})\boldsymbol{s} + \tilde{\boldsymbol{g}}(\boldsymbol{q}) = \tilde{\boldsymbol{\tau}} \tag{2.23}$$

2.8. Summary

This Chapter introduces the concept, design, selection, and dynamic model of flying watch. Firstly, the definition of flying watch is introduced. Then the designs of thrust generating unit and attachment mechanism are explained in detail. After that, several flying watch prototypes are built. Since flying watches come with different mechanisms and dimensions, several selection factors are introduced for preliminary selection of appropriate flying watch for a mission or understanding the application scope of a flying watch. Finally, we derive the equation of motion of flying watch, which will be the foundation of following Chapters.

3. Flying Watch Attachment Allocation Optimization

In Chapter 2, the mechanical design of flying watch is explained. However, the attachment allocation still needs to be determined to install flying watches. Since flying watches in different attachment allocations can enhance the same robotic arm very differently, flying watch attachment allocation can be customized in order to enhance a robotic arm in a mission-dependent way. For example, in Fig 3.1 (a), when the mission of a long arm is to pick up a heavy object, we can attach four flying watches with thrust generating directions in vertical planes containing the corresponding attached links to counteract the gravity of the arm and the heavy object. When the mission of the arm is to push or pull a heavy object on the ground in

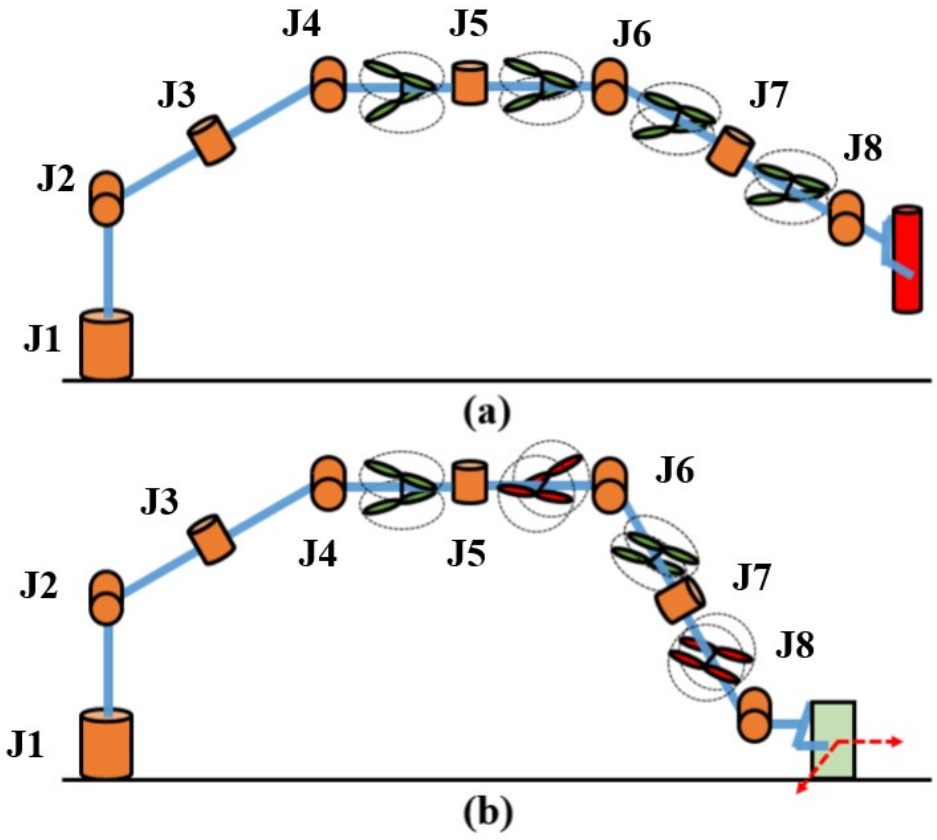

Fig. 3.1. Customization of flying watch attachment allocation. (a) Flying watches help a long arm pick up an object. (b) Flying watches help a long arm push debris on the ground in different directions. Rotation axes of red flying watches are on horizontal planes. Rotation axes of green flying watches are on vertical planes containing the corresponding attached links. J1,…,J8 are joint numbers.

different directions, we can attach two flying watches with thrust generating directions in the horizontal planes and another two flying watches with thrust generating directions in the vertical planes containing the corresponding attached links. Such flying watch attachment allocation helps counteracting vertical arm gravity and horizontal frictions of the heavy object.

However, toward mission-dependent long robotic arm enhancement, two significant problems remain. Firstly, for a certain mission, there is no clear performance metric for flying watch attachment allocations. As a result, given a flying watch attachment allocation, we do not know how to analyze its characteristics and compare it with other attachment allocations. Although there are researches about robotic kinematic and dynamic performance metrics such as manipulability [39]-[42], mobility [43] [44], and dexterity [45] [46]. These metrics cannot evaluate thrust enhancement effect to reduce joint loads. Secondly, although we can roughly design the flying watch attachment allocation based on human experience and knowledge as we did in for the arm in Fig. 3.1, we will demonstrate later in this Chapter that the human-experience-based designs are far from optimal designs. Also, human-experience-based allocation design may take lots of efforts and time, which impedes swift deployment of flying watches. The difficulties of human-experience-based allocation design can be more severe as the degree of freedom of the arm and mission complexity increase. For example, designing a flying watch attachment allocation for the redundant long arm in Fig. 3.1 moving a heavy object from one place to another place in a windy environment would be difficult for human designers since the both the trajectory of the redundant arm and the external reaction forces (e.g. wind loads, end effector reaction forces, and arm gravity, etc.) are very complicated.

In addition, it is highly demanded that the evaluation metric and automated design method for flying watch attachment allocation can consider unexpected end effector reaction forces, whose exact directions and magnitudes cannot be predicted before a mission. Such unexpected end effector reaction forces happen very often due to winds, interaction with unknown

environment, and collision. We will call those unexpected end effector reaction forces as unexpected effect and call known end effector reaction force and arm gravity as known effects. A flying watch attachment allocation design without considering unexpected end effector reaction forces may fail to enhance a long arm when the directions and magnitudes of the unexpected end effector reaction forces fall within the design weakness. When such enhancement failure happens, even small unexpected end effector reaction forces can overload proximal joints and cause very serious consequences. For example, although the four flying watches in Fig. 3.1 (a) can enhance the arm to counteract gravity, if an unexpected side wind happens, the horizontal wind force may overload the 1st and 3rd joints and result in arm failure.

To facilitate mission-dependent long arm enhancement, in this Chapter, reduction rate is firstly introduced in Section 3.1, which is a performance metric of a flying watch attachment allocation counteracting known external forces (i.e. arm gravity and end effector reaction forces). Then a graphical representation of enhancement performance of flying watch attachment allocation counteracting unexpected end effector reaction forces, called Thrust Drivability Surface (TDS), is proposed in Section 3.2. Then based on TDS, another novel performance metric, called Thrust Drivability is proposed in Section 3.3, which measures the ability of flying watch attachment allocation to counteract unexpected end effector reaction forces. Then based on Thrust Drivability, in Section 3.4, an automated design method, called Allocation Optimization based on Weighted Situations (AOWS) is proposed, for designing mission-dependent flying watch attachment allocations that can counteract both unexpected and known external forces (including arm gravity). Finally, in Section 3.5, based on simulations, designing flying watch attachment allocations using AOWS is demonstrated for a static object holding mission and an object manipulation mission and it is shown that AOWS based allocation designs can counteract both known and unexpected external forces much better than human-experience-based allocation designs.

3.1. Reduction Rate

The reduction rate is defined as follows.

$$\zeta = \frac{\|\tilde{\boldsymbol{\tau}}_{bm}(\boldsymbol{s}^*_{bm})\|_\infty - \|\tilde{\boldsymbol{\tau}}_{coi}(\boldsymbol{s}^*_{coi})\|_\infty}{\|\tilde{\boldsymbol{\tau}}_{bm}(\boldsymbol{s}^*_{bm})\|_\infty} \tag{3.1}$$

$\|\tilde{\boldsymbol{\tau}}_{bm}(\boldsymbol{s}^*_{bm})\|_\infty$ is the infinity norm of the normalized joint load vector for a benchmark case, given optimized flying watch thrusts $\boldsymbol{s}^*_{bm}$. $\|\tilde{\boldsymbol{\tau}}_{coi}(\boldsymbol{s}^*_{coi})\|_\infty$ is the infinity norm of the normalized joint load vector for a case of interesting, given optimized flying watch thrusts $\boldsymbol{s}^*_{coi}$. One way to obtain $\boldsymbol{s}^*_{coi}$ and $\boldsymbol{s}^*_{bm}$ is to solve Problem 3.1, which will be used throughout this dissertation for computing reduction rate if there is no special indication.

Problem 3.1: Thrust Optimization (Infinity Norm and Hard Constraint)

$$\min_{\boldsymbol{s}} \|\tilde{\boldsymbol{\tau}}(\boldsymbol{s})\|_\infty \text{ s.t. } \boldsymbol{s}_l \leq \boldsymbol{s} \leq \boldsymbol{s}_u$$

In Problem 3.1, $\tilde{\boldsymbol{\tau}}$ is the normalized joint load vector calculated using (2.23). $\boldsymbol{s}_l$ and $\boldsymbol{s}_u$ are the lower and upper bounds of the flying watch thrust magnitude vector. Problem 3.1 optimizes flying watch thrusts to minimize the infinity norm of the normalized joint load vector, subject to thrust upper and lower bounds. This optimization problem can be solved by interior point method [47]. Interior point method is chosen for the following reasons. (1) Interior point method can handle both equality and inequality constraints. (2). Interior point method is a large-scale method, which means it uses linear algebra that does not need to store or operate on full matrices. This feature can help saving computer memory. (3). Interior point method does not require the user to provide gradient. For the same reasons, I will later also use interior point method to solve flying watch attachment allocation problem. Reduction rate can be used as a metric to measure the performance of flying watch attachment allocations to counteract

known effects. However, the drawback of reduction rate is that it cannot measure the performance of flying watch attachment allocations to counteract unexpected effects since we must know end effector reaction force to optimize flying watch thrusts using (2.23).

3.2. Thrust Drivability Surface

Since unexpected end effector reaction forces (resulting from object manipulation, collision, wind, etc.) happen very often in practice and reduction rate cannot measure the performance of flying watch attachment allocations to counteract unexpected end effector reaction forces, TDS is proposed based on reduction rate to solve this problem. Firstly, since the performance of flying watch attachment allocations to counteract known arm gravity and known end effector reaction force can be evaluated using reduction rate, we focus on unexpected end effector reaction force by separating flying watch EoM (2.23) as follows.

$$-\tilde{\boldsymbol{J}}^T(\boldsymbol{q})\boldsymbol{F}_k - \tilde{\boldsymbol{R}}(\boldsymbol{q})\boldsymbol{s}_k + \tilde{\boldsymbol{g}}(\boldsymbol{q}) = \tilde{\boldsymbol{\tau}}_k \tag{3.2}$$

$$-\tilde{\boldsymbol{J}}^T(\boldsymbol{q})\boldsymbol{F}_u - \tilde{\boldsymbol{R}}(\boldsymbol{q})\boldsymbol{s}_u = \tilde{\boldsymbol{\tau}}_u \tag{3.3}$$

In (3.2) and (3.3), $\boldsymbol{F}_e = \boldsymbol{F}_k + \boldsymbol{F}_u$, where $\boldsymbol{F}_k$ is the known end effector reaction forces and $\boldsymbol{F}_u$ is the unexpected end effector reaction forces. $\boldsymbol{s} = \boldsymbol{s}_k + \boldsymbol{s}_u$, where $\boldsymbol{s}_k$ is the flying watch thrusts for counteracting known arm gravity and known end effector reaction forces and $\boldsymbol{s}_u$ is the flying watch thrust magnitude vectors for counteracting unexpected end effector reaction forces. $\tilde{\boldsymbol{\tau}} = \tilde{\boldsymbol{\tau}}_k + \tilde{\boldsymbol{\tau}}_u$, where $\tilde{\boldsymbol{\tau}}_k$ are the joint loads resulted from known arm gravity and known end effector reaction forces and $\tilde{\boldsymbol{\tau}}_u$ is joint loads resulted from unexpected end effector reaction forces. Then let us optimize the thrust magnitude vector in (3.3) by solving the following Problem 3.2.

Problem 3.2: Thrust Optimization (2-Norm and Soft Constraints)

$$\min_{s} \left\| -\tilde{\boldsymbol{J}}^T \boldsymbol{F}_u - \tilde{\boldsymbol{R}} \boldsymbol{s}_u \right\|_2^2 + \lambda^2 \|\boldsymbol{s}_u\|_2^2$$

Problem 3.2 intends to minimize the 2-norm squares of both normalized torque vector and flying watch thrusts vector. Problem 3.2 can be solved using damped least squares method [48], [49] as follows.

$$\boldsymbol{s}_u^+ = -\tilde{\boldsymbol{R}}^+ \tilde{\boldsymbol{J}}^T \boldsymbol{F}_u = -\tilde{\boldsymbol{R}}^T \boldsymbol{b} \tag{3.4}$$

where

$$\boldsymbol{b} = \left(\tilde{\boldsymbol{R}}\tilde{\boldsymbol{R}}^T + \lambda^2 \boldsymbol{I}\right)^{-1} (\tilde{\boldsymbol{J}}^T \boldsymbol{F}_u) \tag{3.5}$$

In (3.4), $\tilde{\boldsymbol{R}}^+ = \tilde{\boldsymbol{R}}^T \left(\tilde{\boldsymbol{R}}\tilde{\boldsymbol{R}}^T + \lambda^2 \boldsymbol{I}\right)^{-1}$ is the damped pseudoinverse matrix of the normalized attachment style matrix $\tilde{\boldsymbol{R}}$. Since $\tilde{\boldsymbol{R}}^+$ includes the inverse of $\left(\tilde{\boldsymbol{R}}\tilde{\boldsymbol{R}}^T + \lambda^2 \boldsymbol{I}\right)^{-1}$, which could be a large matrix for redundant long arms with many degrees of freedom, directly computing $\tilde{\boldsymbol{R}}^+$ is computationally intensive. Therefore, an intermediate load vector $\boldsymbol{b}$ is introduced, which is the solution of $(\tilde{\boldsymbol{R}}\tilde{\boldsymbol{R}}^T + \lambda^2 \boldsymbol{I})\boldsymbol{b} = \tilde{\boldsymbol{J}}^T \boldsymbol{F}_u$. Such linear equation can be efficiently solved using LU decomposition.

We optimize flying watch thrusts for TDS and Thrust Drivability by solving Problem 3.2 instead of Problem 3.1 for the following two reasons. (1) TDS and Thrust Drivability are intrinsic properties of a flying watch attachment allocation characterizing its ability to counteract uncertain end effector reaction forces. Therefore, TDS and Thrust Drivability should not depend on flying watch specifications (such as the maximum thrust of a specific flying watch). Therefore Problem 3.2 with soft constraints on flying watch magnitudes is better than Problem 3.1 with hard constraints enforcing specific flying watch thrust capacity. (2) Problem 3.2 with a concise analytical solution (3.4), (3.5) can be solved much more efficiently than

Problem 3.1 solved with iterative interior point method [47]. We will later see that this advantage is the basis of computing TDS with high resolution and incorporating Thrust Drivability into the cost function of AOWS, both of which optimize flying watch thrusts intensively.

Now we can evaluate how much $\boldsymbol{s}_u^+$ can reduce $\|\tilde{\boldsymbol{\tau}}_u\|_\infty$ compared with no thrust case given an unexpected unit end effector reaction force $\boldsymbol{F}_u = \boldsymbol{e}(\theta, \phi)$. θ and ϕ are respectively polar and azimuthal angles of the unexpected unit end effector reaction force. From (3.3), we can obtain the follows.

$$\rho(\theta, \phi) = \frac{\left\|-\tilde{\boldsymbol{J}}^T \boldsymbol{e}(\theta, \phi)\right\|_\infty - \left\|-\tilde{\boldsymbol{J}}^T \boldsymbol{e}(\theta, \phi) - \tilde{\boldsymbol{R}} \boldsymbol{s}_u\right\|_\infty}{\left\|-\tilde{\boldsymbol{J}}^T \boldsymbol{e}(\theta, \phi)\right\|_\infty} \tag{3.6}$$

In (3.6), $\rho(\theta,\phi)$ gives the relative ratio of $\|\tilde{\boldsymbol{\tau}}_u\|_\infty$ that $\boldsymbol{s}_u^+$ can reduce compared with no thrust case. It is interesting to observe that even when the magnitude of $\boldsymbol{F}_u$ is not 1, $\rho(\theta, \phi)$ is still achievable by multiply $\boldsymbol{s}_u^+$ with the magnitude of $\boldsymbol{F}_u$. This means $\rho(\theta,\phi)$ is the lower bound of the relative ratio of $\|\tilde{\boldsymbol{\tau}}_u\|_\infty$ that flying watches can reduce for unexpected end effector reaction forces with different magnitudes in direction of $\boldsymbol{e}(\theta, \phi)$.

Now let us look at another interpretation of $\rho(\theta,\phi)$ from the perspective of total joint load. Let $\zeta = (\|\tilde{\boldsymbol{\tau}}_{bm}^*\|_\infty - \|\tilde{\boldsymbol{\tau}}_k^*\|_\infty)/\|\tilde{\boldsymbol{\tau}}_{bm}^*\|_\infty$, where $\tilde{\boldsymbol{\tau}}_{bm}^*$ is the joint loads of the benchmark allocation due to known effects corresponding to $\boldsymbol{s}_{bm}^*$ solved from Problem 3.1 without constraints and $\tilde{\boldsymbol{\tau}}_k^*$ is the joint loads of the current allocation due to known effect corresponding to $\boldsymbol{s}_k^*$ solved from Problem 3.1 without constraints. Also let $\rho = (\|\tilde{\boldsymbol{\tau}}_u^0\|_\infty - \|\tilde{\boldsymbol{\tau}}_u^+\|_\infty)/\|\tilde{\boldsymbol{\tau}}_u^0\|_\infty$, where $\tilde{\boldsymbol{\tau}}_u^0$ is the joint loads when there is no flying watch due to unexpected effects and $\tilde{\boldsymbol{\tau}}_u^+$ is the joint loads of the current allocation due to unexpected effects corresponding to $\boldsymbol{s}_u^+$ solved from Problem 3.2. $\tilde{\boldsymbol{\tau}}^*$ is the joint loads of the current allocation due to both known and unknown

effects corresponding to $\boldsymbol{s}^*$ solved from Problem 3.1 with no constraints. We can derive the following relations.

$$\|\tilde{\boldsymbol{\tau}}^*\|_\infty \leq \|\tilde{\boldsymbol{\tau}}_k^* + \tilde{\boldsymbol{\tau}}_u^+\|_\infty \leq \|\tilde{\boldsymbol{\tau}}_k^*\|_\infty + \|\tilde{\boldsymbol{\tau}}_u^+\|_\infty = \|\tilde{\boldsymbol{\tau}}_{bm}^*\|_\infty(1-\zeta) + \|\tilde{\boldsymbol{\tau}}_u^0\|_\infty(1-\rho) \tag{3.7}$$

First inequality is due to minimum definition. The second inequality is due to norm property. If we divide both sides of (3.7) with $\|\tilde{\boldsymbol{\tau}}_{bm}^*\|_\infty + \|\tilde{\boldsymbol{\tau}}_u^0\|_\infty$, we can obtain the follows assuming $k = \frac{\left\|\tilde{\boldsymbol{\tau}}_u^0\right\|_\infty}{\|\tilde{\boldsymbol{\tau}}_{bm}^*\|_\infty + \left\|\tilde{\boldsymbol{\tau}}_u^0\right\|_\infty}$.

$$\frac{\|\tilde{\boldsymbol{\tau}}^*\|_\infty}{\left\|\tilde{\boldsymbol{\tau}}_{bm}^*\right\|_\infty + \left\|\tilde{\boldsymbol{\tau}}_u^0\right\|_\infty} \leq (1-k)(1-\zeta) + k(1-\rho) \leq \max(1-\zeta, 1-\rho) \tag{3.8}$$

From (3.8), we can see that $\max(1-\zeta, 1-\rho)$ is the upper bound of relative value of optimal total joint torque given no constraints on flying watch thrusts. This means given strong enough flying watches, reducing reduction rate ζ and ρ can helps reducing total joint torques.

As shown in Fig. 3.2, if we regard ρ as radial distance then (3.6) is actually the parametric equation of a closed surface. We called this surface Thrust Drivability Surface (TDS). We can uniformly sample $\theta \in [0, \pi], \phi \in [0, 2\pi]$ with certain resolution and calculate $\rho(\theta, \phi)$ to visualize TDS. TDS can visualize the ability of a flying watch attachment allocation to counteract unexpected end effector reaction forces with different magnitudes and directions.

3.3. Thrust Drivability

It is desirable to derive a quantitative metric from TDS to measure the ability of a flying watch attachment allocation to counteract unexpected end effector reaction forces with different magnitudes and directions.

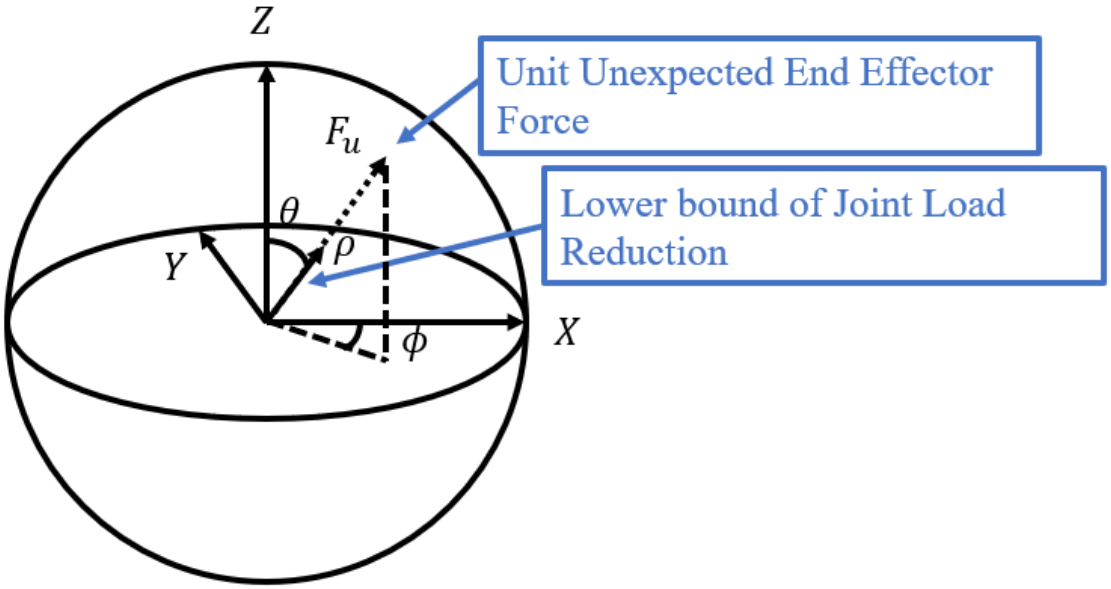

Fig. 3.2. Thrust Drivability Surface.

Let us first consider what an ideal TDS looks like. The ideal situation is that a flying watch attachment allocation can counteract 100% unexpected end effector reaction force in any direction with any magnitude. In other words, $\left\|-\tilde{\boldsymbol{J}}^T \boldsymbol{e}(\theta,\phi) - \tilde{\boldsymbol{R}}\boldsymbol{s}_u\right\|_\infty$ in (3.6) is always zero regardless of θ and ϕ. In this ideal situation, the TDS is a unit sphere. Based on this observation, we can obtain a quantitative metric by comparing the volume of a TDS with a unit sphere. To measure the ability of a flying watch attachment allocation to counteract unexpected end effector reaction forces within a polar angle range $\theta \in [\theta_l, \theta_u]$ and azimuthal angle range $\phi \in [\phi_l, \phi_u]$, we can compare the corresponding volumes of the TDS and unit sphere as follows.

$$D = \frac{V_{TDS}(\boldsymbol{\omega})}{V_{unit}(\boldsymbol{\omega})} \tag{3.9}$$

In (3.9), $\boldsymbol{\omega} = [\theta_l, \theta_u, \phi_l, \phi_u]$ is the direction region of the unexpected end effector reaction force. $V_{TDS}(\boldsymbol{\omega})$ and $V_{unit}(\boldsymbol{\omega})$ are respectively the volume of TDS and unit sphere inside the direction region defined by $\boldsymbol{\omega}$. The ratio of those two volumes is defined as Thrust Drivability, denoted as D throughout this dissertation. Thrust Drivability is a quantitative

metric of the ability of a flying watch attachment allocation to counteract unexpected end effector reaction forces with directions in $\boldsymbol{\omega}$ and unknown magnitudes. In spherical coordinate, since the infinitesimal volume can be written as $dV = \rho^2 sin\theta d\theta d\phi d\rho$, we can write (3.7) as follows.

$$D = \frac{\int_{\theta_l}^{\theta_u} \int_{\phi_l}^{\phi_u} \rho^3(\theta,\phi) sin\theta d\theta d\phi}{(cos\ \theta_l - cos\theta_u)(\phi_u - \phi_l)} \tag{3.10}$$

We can discretize (3.10) as follows to make it easier for numerical calculation.

$$D = \frac{\sum_{\theta_l}^{\theta_u} \sum_{\phi_l}^{\phi_u} \rho^3(\theta,\phi) sin\theta d\theta d\phi}{(cos\ \theta_l - cos\theta_u)(\phi_u - \phi_l)} \tag{3.11}$$

Up to now, we derived TDS and Thrust Drivability only considering unexpected end effector reaction forces. Therefore, the TDS and Thrust Drivability we derived are more specifically Force TDS and Force Thrust Drivability. However, we can also derive Torque TDS and Torque Thrust Drivability by applying similar derivation process to unexpected end effector reaction torques. Without special indications, TDS and Thrust Drivability in this dissertation refer to the Force TDS and Force Thrust Drivability.

3.4. Allocation Optimization based on Weighted Situations (AOWS)

In this Section, a novel automated design method for designing mission-dependent flying watch attachment allocation, called Allocation Optimization based on Weighted Situations (AOWS) is proposed. Firstly a mission model, called Weighted Situation Model (WSM) and a convenient description of flying watch attachment allocation based on Denavit–Hartenberg convention (DH Convention) [50], called DH-Allocation Description (DHAD) are introduced. Then based on WSM and DHAD, AOWS is proposed. Finally, the systematic attachment allocation design procedure is introduced.

3.4.1. Weighted Situation Model

In a robotic arm manipulation mission, an arm may experience a combination of static and moving processes and different kinds of external forces may be exerted on the end effector. A mission can be described by a 2-tuple $\boldsymbol{\Pi} = (\boldsymbol{E}, \boldsymbol{P})$, where $\boldsymbol{E} = \{\boldsymbol{e}_1, \dots, \boldsymbol{e}_W\}$ is a set of W representative situations during a mission and $\boldsymbol{P} = \{p_1, \dots, p_W\}$ is a set of importance factors corresponding to situations in $\boldsymbol{E}$. The i th situation is defined as a 2-tuple $\boldsymbol{e}_i = (\boldsymbol{q}_i, \boldsymbol{F}_{ki})$, where $\boldsymbol{q}_i$ is the generalized coordinates defining the arm configuration in the situation and $\boldsymbol{F}_{ki}$ is the known end effector reaction force at this situation. A situation depicts an arm status at a representative moment during a mission. The importance factor of a situation describes the significance of a situation, which may be determined by the probability of a situation or designers' judgement. For example, the designer may assign a high importance factor to a rare situation that may cause serious consequences.

3.4.2. DH-Allocation Description

To optimize flying watch attachment allocation, an intuitive way is to directly optimize the absolute positions and orientations of flying watches regarding the fixed base frame. However, since flying watch must be fixed on arm links as the arm moves, optimizing such absolute allocation description will result in complicated constraints. To simplify the allocation optimization problem, we propose to use a relative allocation description based on DH Convention. In DH Convention, the i th DH frame is attached to the i th arm link. The allocation of a flying watch on the i th link is defined by a vector of 6 elements, $\boldsymbol{\mu}_f = [\boldsymbol{\mu}_d, \boldsymbol{\mu}_\eta] = [\mu_{d1}, \mu_{d2}, \mu_{d3}, \mu_{\eta 1}, \mu_{\eta 2}, \mu_{\eta 3}]$. $\boldsymbol{\mu}_d = [\mu_{d1}, \mu_{d2}, \mu_{d3}]$ is the position of the flying

watch regarding the i th DH frame. $\boldsymbol{\mu_\eta} = [\mu_{\eta1}, \mu_{\eta2}, \mu_{\eta3}]$ is the unit direction vector regarding the i th DH frame. We call such kind of description as Full DH Allocation Description (full DHAD). And $\boldsymbol{\mu_f}$ is called Full DHAD vector. We can easily convert $\boldsymbol{\mu_d}$ and $\boldsymbol{\mu_\eta}$ to position vector $\boldsymbol{d} = \boldsymbol{R_i^{DH}\mu_d} + \boldsymbol{r_i^{DH}}$ and unit direction vector $\boldsymbol{a} = \boldsymbol{R_i^{DH}\mu_\eta}$ regarding the base frame, where $\boldsymbol{R_i^{DH}}$ and $\boldsymbol{r_i^{DH}}$ are respectively the rotation matrix and position vector of the i th DH frame. The absolute positions and directions of flying watches are necessary for computing the attachment style matrix or visualizing flying watches.

Under the following assumptions, which are often applicable in practice, it is possible to simplify the full DHAD description. (1) All links are straight and perpendicular to their joint axes. (2) All joints are rotary. DHAD vector of a flying watch attached to the i th link can be further simplified as a vector with two elements, $\boldsymbol{\mu_s} = (\mu_{sd}, \mu_{s\eta})$. μ_{sd} is the coordinate of the flying watch on X axis of the i th DH frame, which reflects the position of the flying watch. $\mu_{s\eta}$ is the angle between the flying watch thrust vector and Y axis of the i th DH frame which reflects the orientation of the flying watch. We call such simplified description as Simplified DHAD. And $\boldsymbol{\mu_s}$ is called simplified DHAD vector. We can use $\boldsymbol{\mu_f} = [\mu_{sd}, 0, 0, 0, cos\mu_{s\eta}, sin\mu_{s\eta}]$ to simply convert $\boldsymbol{\mu_s}$ to $\boldsymbol{\mu_f}$. The advantage of DHAD is that it separates all allocation information (flying watch attachment position and orientation) from robotic arm configuration and thusly significantly simplifies constraints in attachment allocation optimization process.

3.4.3. Allocation Optimization based on Weighted Situations

AOWS is an automated design method for designing mission-dependent flying watch attachment allocation considering both known arm gravity, known end effector reaction forces, and unexpected end effector reaction forces. AOWS solves the following problem.

Problem 3.3: Allocation Optimization based on Weighted Situations (AOWS)

$$\min_{\boldsymbol{s}_1,\dots,\boldsymbol{s}_W}(1-\beta)\sum_{i=1}^{W}\frac{p_i\|\tilde{\boldsymbol{\tau}}_{ki}(\boldsymbol{\mu},\boldsymbol{s}_i,\boldsymbol{q}_i\boldsymbol{F}_{ki})\|_\infty}{\|\tilde{\boldsymbol{\tau}}^0_{ki}(\boldsymbol{q}_i,\boldsymbol{F}_{ki})\|_\infty}+\beta\sum_{i=1}^{W}p_i\sum_{j=1}^{V}\alpha_j\left(1-D_{ij}(\boldsymbol{\mu},\boldsymbol{q}_i,\boldsymbol{\omega}_j)\right)\ s.t.\ \boldsymbol{\mu},\boldsymbol{s}_1,\dots,\boldsymbol{s}_W\in\boldsymbol{C}$$

In Problem 3.3, $\boldsymbol{\mu}$ is the DHAD vector describing the flying watch allocation. We used simplified DHAD in this dissertation for simplicity. $\boldsymbol{s}_1,\dots,\boldsymbol{s}_W$ are the corresponding flying watch thrust magnitude vectors of W situations. $\boldsymbol{q}_1,\dots,\boldsymbol{q}_W$ are the corresponding generalized coordinates vectors describing arm configurations in the W situations. $\boldsymbol{F}_{k1},\dots,\boldsymbol{F}_{kW}$ are the corresponding known end effector reaction forces of the W situations. $\tilde{\boldsymbol{\tau}}_{k1},\dots,\tilde{\boldsymbol{\tau}}_{kW}$, which can be reduced by optimizing $\boldsymbol{\mu}$ and $\boldsymbol{s}_1,\dots,\boldsymbol{s}_W$, are the corresponding normalized joint load vectors of the W situations resulting from arm gravity (including flying watch gravity) and known end effector reaction forces. $\tilde{\boldsymbol{\tau}}^0_{k1},\dots,\tilde{\boldsymbol{\tau}}^0_{kW}$ are the corresponding joint load vectors of the W situations assuming zero flying watch thrusts and initial flying watch attachment allocation. We used the infinity norm of $\tilde{\boldsymbol{\tau}}^0_{k1},\dots,\tilde{\boldsymbol{\tau}}^0_{kW}$ to normalize the infinity norm of $\tilde{\boldsymbol{\tau}}_{k1},\dots,\tilde{\boldsymbol{\tau}}_{kW}$ to range between 0 and 1. $p_1,\dots,p_W$ are the corresponding importance factors of the W situations. β is the unexpected effect weight factor. $D_{i1},\dots,D_{iV}$ are the drivabilities for the i th situation in the corresponding V direction regions $\boldsymbol{\omega}_1,\dots,\boldsymbol{\omega}_V$ that we want to maximize. $\alpha_1,\dots,\alpha_V$ are the drivability weight factors. $\boldsymbol{C}$ is the constraints of $\boldsymbol{\mu}$, $\boldsymbol{s}_1,\dots,\boldsymbol{s}_W$ considering robotic arm and flying watch specifications.

AOWS is minimizing the weighted summation of two terms. The first term (known effect term) is trying to minimize the infinity norm of the joint load vector of each representative situations. The second term (the unknown effect term) is a weighted summation of $1-D_{ij}$.

Therefore, the purpose of the second term is to maximize Thrust Drivability. We can imagine that there is a trade-off between these two terms since maximizing Thrust Drivability tend to increase the orientation diversity of flying watches while counteracting certain known effect tend to reduce the orientation diversity of flying watches so that all flying watches can focus on counteracting the same known forces. The unexpected effect weight factor β allows the user to handle this trade-off. We can see from EoM (3.2), that the joint load vector $\tilde{\boldsymbol{\tau}}_{ki}$ depends on both flying watch thrust magnitudes and flying watch attachment allocations. As a result, the flying watch thrusts must be optimized together with flying watch attachment allocations. Therefore, both DHAD vector $\boldsymbol{\mu}$ and flying watch thrust magnitude vectors $\boldsymbol{s}_1, \ldots, \boldsymbol{s}_W$ are the optimization variables. Based on our analysis, we can understand that Problem 3.3 is solving the flying watch allocation $\boldsymbol{\mu}$, which has optimal balanced performance for counteracting both known arm gravity (including flying watch gravity) and known end effector reaction forces as well as unexpected end effector reaction forces. Problem 3.3 can be solved using interior point method [47].

3.4.4. Overall Allocation Design Process

Up to now, we have introduced reduction rate as a metric measuring the ability of flying watch attachment allocations to counteract known arm gravity (including flying watch gravity) and known end effector reaction force. Also, we introduced Thrust Drivability as a metric of flying watch attachment allocations measuring their ability to counteract unknown end effector reaction forces. Based on Thrust Drivability, we proposed AOWS as an automated design tool for designing mission-dependent flying watch attachment allocation. In this Section, we discuss how to put all those components together as a systematic design process. Those tools can be put together as shown in Fig. 3.3. The first step is to do mission planning, where the

trajectory of the robotic arm during a mission is generated. Then we need to select representative arm situations in the mission and decide their corresponding important factors to form a WSM $\boldsymbol{\Pi} = (\boldsymbol{E}, \boldsymbol{P})$. Also we need to determine the direction regions $\boldsymbol{\omega}_1, \dots, \boldsymbol{\omega}_V$ of unexpected end effector reaction forces and their corresponding drivability weight factors $\alpha_1, \dots, \alpha_V$ as well as the unexpected effect weight factor β. The mentioned parameters (WSM, direction regions, drivability weight factors, and unexpected effect weight factor) are design parameters. Then those initial parameters are fed to the AOWS to generate an optimal flying watch attachment allocation. Next we need to evaluate the performance of the obtained optimal allocation. The following three methods with different features can be used. (1) Reduction rate is a metric to measure the performance of a flying watch attachment allocation to counteract known arm gravity (including flying watch gravity) and known end effector reaction forces. (2) TDS is a graphical method visualizing the ability of a flying watch attachment allocation to counteract unexpected end effector reaction forces with different magnitudes and directions. (3) Thrust Drivability is a numerical metric measuring the ability of a flying watch attachment allocation to counteract unexpected end effector reaction forces with uncertain magnitudes in

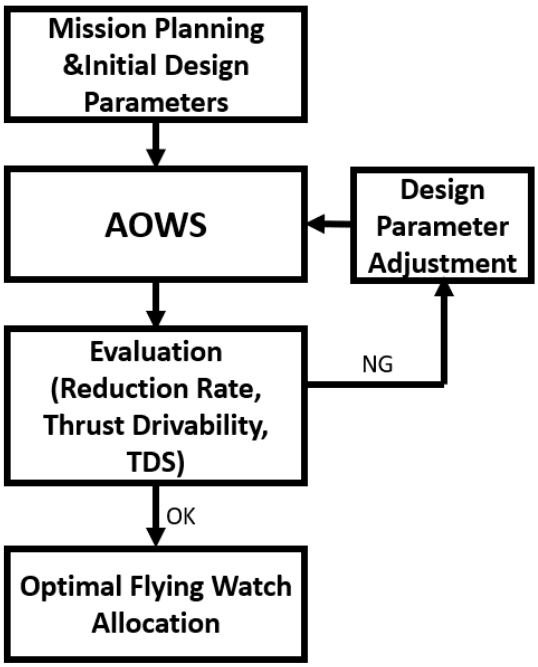

Fig. 3.3. The overall design process of flying watch allocation

a direction region. After evaluation using those three methods, if some performance is not satisfactory, we can adjust the design parameters and run AOWS again. For example, if the obtained allocation cannot counteract unexpected wind forces on the end effector well enough, we can increase unexpected effect weight factor β. If the obtained allocation cannot counteract known end effector reaction forces in horizontal directions well enough, we can increase importance factors of corresponding situations that include the horizontal forces. This redesign process is repeated until a satisfactory allocation is obtained.

3.5. Simulation Verification

In this Section, we simulate a 9-DoF long-reach robotic arm doing two typical arm missions to test the effectiveness of AOWS. The first mission is a static object holding mission, where an arm is required to hold an object with 15 N gravity statically. The second mission is an object manipulation mission, where the arm is required to move the same object from one position to another position along a trajectory. These two typical missions are the components of many more complicated missions. During these two missions, the robotic arm needs to counteract its own gravity, the object gravity, and occasional 10 N side wind on the object in horizontal directions (assuming wind forces on other parts of the arm are neglectable). We will design mission-dependent flying watch allocations for these two missions using AOWS and compare the AOWS-based allocations with human-experience-based allocations. In the rest of this subsection, the arm and flying watch specification is firstly introduced. Then the human-experience-based allocation design is introduced. Finally, we will introduce some common implementation details for these two missions.

The arm specification is shown in Fig. 3.4. The arm is a 9-Dof redundant arm with a motor in each joint. The arm links are made of CFRP with inner diameter of 31 mm and thickness of 2mm. The arm joint mass (including motors, gears, and housing) is 0.59 kg. The total mass of the arm is 8.81 kg. The base frame is represented by purple arrows and the end effector frame is represented by red arrows. Please note that all coordinate systems in this dissertation are right-handed coordinate systems. The arm design is derived from an existing long-reach arm in our lab [7] and our feasibility investigation on motors and gears in the market.

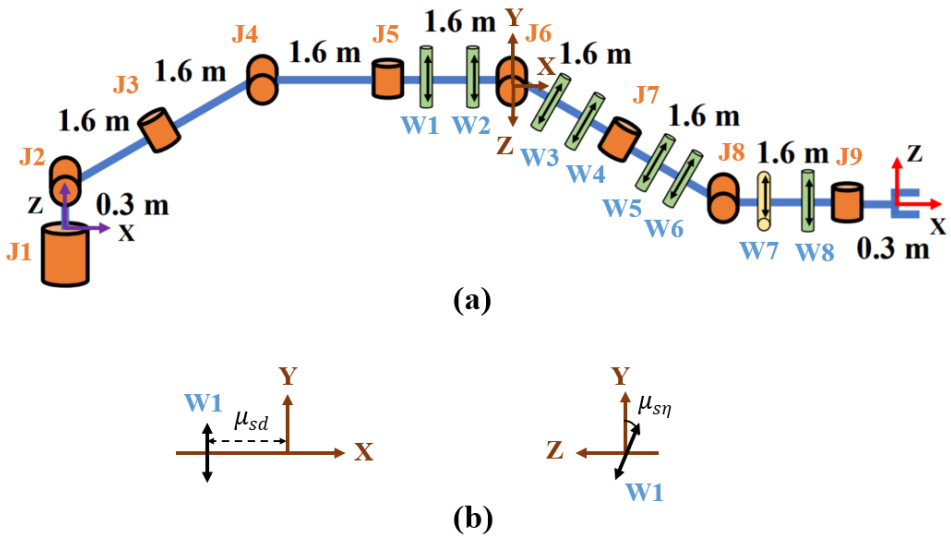

Fig. 3.4. Specification of the simulation arm and the human-experience-based design of flying watch allocation.

The specification of flying watch is the same as the physical prototype in Fig. 2.11. The propeller diameter of a flying watch is 381 mm and the maximum thrust of one flying watch is 18 N (slightly smaller than the maximum thrust to avoid overheating). The mass of one flying watch is 542 g. The dimension of a flying watch (not including propellers) is length (66 mm), width (56 mm), and height (48 mm). The human-experience-based flying watch allocation is also shown in Fig. 3.4. The flying watches are represented by cylinders for simplicity. The thrust generating direction of a flying watch is represented by the arrow on the cylinder. Under the arm configuration of Fig. 3.4 when all links are in the same vertical plane, green cylinders

represent flying watches with thrust generating directions in the vertical link plane and yellow cylinders represent flying watches with thrust generating directions in horizontal planes. Using flying watch 1 as an example, Fig. 3.4 (b) shows the meaning of flying watch position μ_{sd} and orientation $\mu_{s\eta}$ as defined by simplified DHAD. The brown frame is the DH frame of the link that flying watch 1 is attached to. Since the gravity of the arm is 88.1N and the thrust of a flying watch is 12.58 N higher than its gravity, about 7 flying watches are necessary to counteract the arm gravity. We attached 7 flying watches to distal links with thrust generating directions in the vertical link plane for counteracting arm gravity and other vertical end effector reaction forces. We also attached one flying watch on the eighth link with the thrust generating direction in the horizontal plane for counteracting end effector reaction forces in horizontal planes. The distance between a flying watch and its closest joint is 0.4 m. We index the flying watches from 1 to 8 from the most proximal one to the most distal one.

The common implementation details for the static object holding mission and object manipulation mission are as follows. We used Matlab R2019a to simulate the 9-DoF arm and implement AOWS based on the optimization toolbox of Matlab. For simplicity, we assumed the motor on each joint are identical. As a result, we used identity matrix as the normalization matrix. For AOWS, we constrain the minimum distance between the flying watch attachment point and its closest joint to be 0.3 m. We can derive from this minimum distance and flying watch dimensions that to avoid collision, the maximum rotation of the fifth and ninth joints should not exceed $135.5°$ and the maximum rotation of the sixth, seventh, eighth joints should not exceed $96.1°$. $5°$ safety margins are included when calculating these joint constraints. For the second to fourth joints, 10 degrees margin is left to ensure adjacent links will not collide. The base joint is free to rotate. Those joint constraints are guaranteed when computing inverse kinematics and generating arm path. We also constrain that the two flying watches to be attached on both sides of the middle point of corresponding links. The minimum distance

between a flying watch and the middle point on the same link is 0.23 m. Therefore, no collision will happen for the flying watches on the same link. We used the human-experience-based flying watch allocation with no flying watch thrusts as the initial value of AOWS. When calculating the intermediate load vector using (3.5), we used $\lambda = 0.01$. Please note if there is no special indication, all coordinates in this Section are referring to the base frame of the simulation arm.

3.5.1. Static Object Holding Mission

In this mission, the robotic arm will hold an object with gravity of 15 N at [11,2,0.8] m with the end effector frame coincides with the base frame. A 10 N wind load with direction of positive y axis direction of the base frame (probability=30%) and negative y axis direction of the base frame (probability=30%) will act on the end effector. We choose [11,2,0.8] as the end effector position since it is far from base frame and the large torques on proximal joints are challenging for the long arm. To use AOWS, we need to construct a WSM. We firstly solve an inverse kinematics problem with joint constraints to obtain the robot configuration $\boldsymbol{q}_{m1}$ = [0.00,−0.07,0.39,0.02,−0.02,−0.01,−0.49,0.05,0.12]. Then based on the known end effector reaction forces, we can find the following three representative situations. (1) $\boldsymbol{e}_1 = (\boldsymbol{q}_1, \boldsymbol{F}_1)$, where $\boldsymbol{q}_1 = \boldsymbol{q}_{m1}$ and $\boldsymbol{F}_1 = [0,0,-15]N$. (2) $\boldsymbol{e}_2 = (\boldsymbol{q}_2, \boldsymbol{F}_2)$, where $\boldsymbol{q}_2 = \boldsymbol{q}_{m1}$ and $\boldsymbol{F}_2 = [0,10,-15]N$. (3) $\boldsymbol{e}3 = (\boldsymbol{q}_3, \boldsymbol{F}_3)$, where $\boldsymbol{q}_3 = \boldsymbol{q}_{m1}$ and $\boldsymbol{F}_3 = [0,-10,-15]N$. Based on those three representative situations, we can construct a WSM $\boldsymbol{\Pi}_{m1} = (\boldsymbol{E}_{m1}, \boldsymbol{P}_{m1})$, where $\boldsymbol{E}_{m1} = \{\boldsymbol{e}_1, \boldsymbol{e}_2, \boldsymbol{e}_3\}$ and $\boldsymbol{P}_{m1} = \{0.4, 0.3, 0.3\}$. Here we used the probabilities of events as the corresponding importance factors. Although we know the arm needs to counteract its own gravity, the object gravity, and wind forces, we also hope the arm to be able to counteract unexpected environmental forces from varieties of directions due to unexpected wind and

collisions. Therefore, we set the direction region of unexpected end effector reaction forces as $\boldsymbol{\omega}_{m1} = [0, \pi, 0, 2\pi]$ with drivability weight factor $\alpha_{m1} = 1$. We set the unexpected effect weight factor $\beta_{m1} = 0.5$.

We input those design parameters to AOWS. The AOWS-based allocation and the human-experience-based allocation are shown in Table 3.1. The flying watch positions and orientations are described using simplified DHAD.

Table 3.1. AOWS-BASED AND HUMAN-EXPERIENCE-BASED ALLOCATIONS OF STATIC MISSION

Flying Watch Index	1	2	3	4	5	6	7	8
AOWS (Position) (m)	-1.14	-0.42	-1.14	-0.41	-1.19	-0.41	-1.11	-0.39
AOWS (Orientation) (°)	-1.46	19.15	101.34	50.71	-20.87	6.17	87.74	102.89
Human-Experience (Position) (m)	-1.20	-0.40	-1.20	-0.40	-1.20	-0.40	-1.20	-0.40
Human-Experience (Orientation) (°)	0.00	0.00	90.00	90.00	0.00	0.00	0.00	90.00

The human-experience-based allocation and AOWS-based allocation in the second representative situation ($\boldsymbol{e}_2 = (\boldsymbol{q}_2, \boldsymbol{F}_2)$, where $\boldsymbol{q}_2 = \boldsymbol{q}_{m1}$ and $F_2 = [0,10,-15]N$) are shown in Fig. 3.5-3.8. We also calculate TDSs for both allocations and show them in Fig. 3.5-3.8. In this Section, we define front view (the same view as that of Fig. 3.4) as the view when seeing along positive Y axis direction of the base frame, back view as the view when seeing along negative Y direction of the base frame, top view as the view when seeing along negative Z direction of the base frame, and down view as the view when seeing along the positive Z direction of the base frame. When drawing TDS alone, the center of TDS is moved to the origin of base frame so that the reader can more easily understand the dimensions of TDS. The positive directions of X, Y, Z axes of the base frame are respectively shown using magenta, green, and cyan lines. The blue lines indicate the links of the arm and the black dots indicate

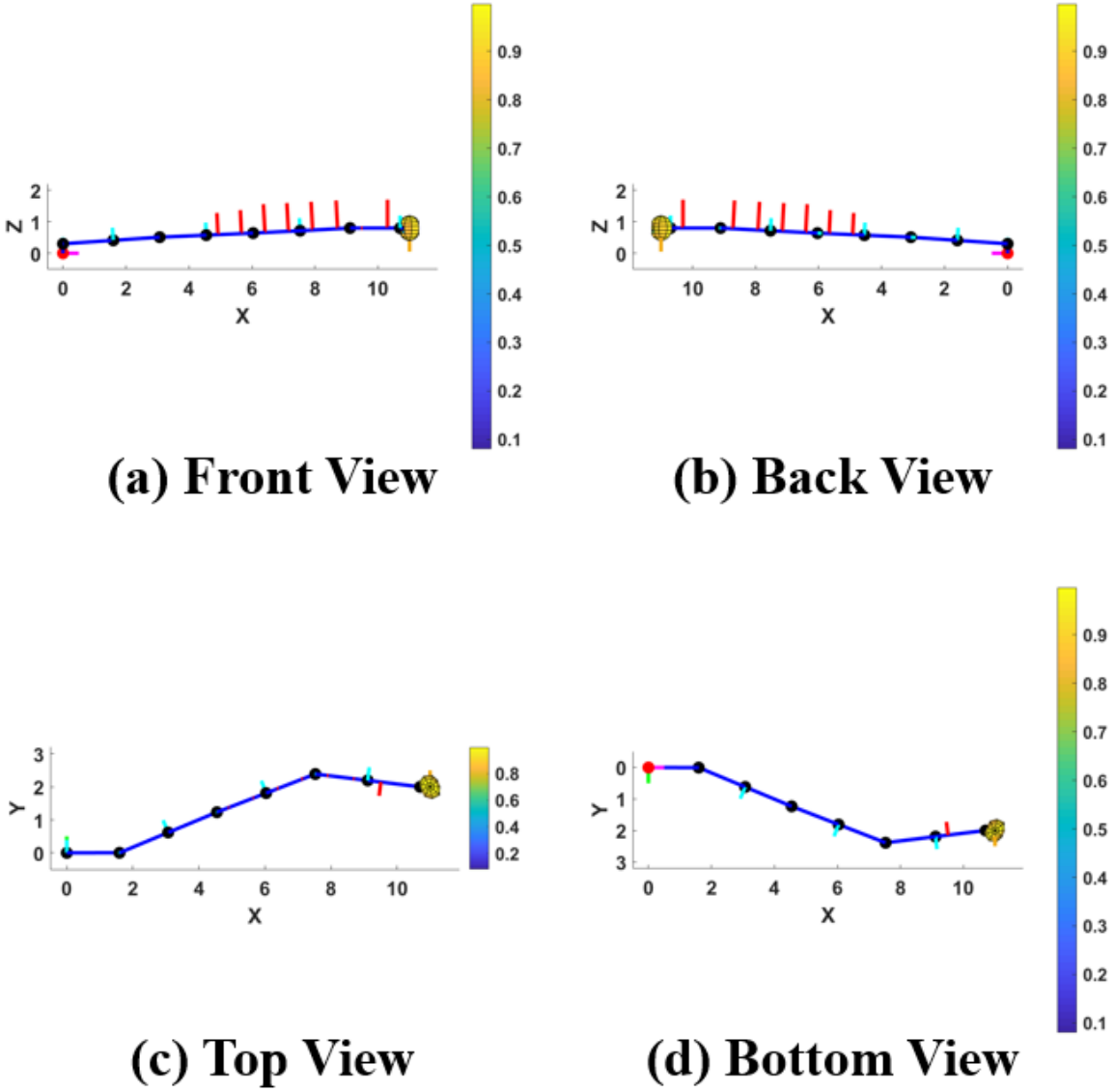

Fig. 3.5. Human-experience-based flying watch allocation in the static object holding mission. (a) Front view. (b) Back view. (c) Top view. (d) Bottom view.

the position of the joints. The cyan lines on the joints indicate the joint rotation axes. The end effector reaction force is shown using orange lines. The corresponding optimized flying watch thrusts are also shown using red lines.

From Table 3.1 and Fig. 3.5-3.8, we can firstly see that compared with the human-experience-based design, AOWS moves several flying watches (1st ,3rd ,7 th) significantly closer (≥ 5cm) to the end effector to increase moment arms. Also, in the human-experience-based design, only the 7th flying watch is attached with thrust generating direction in the

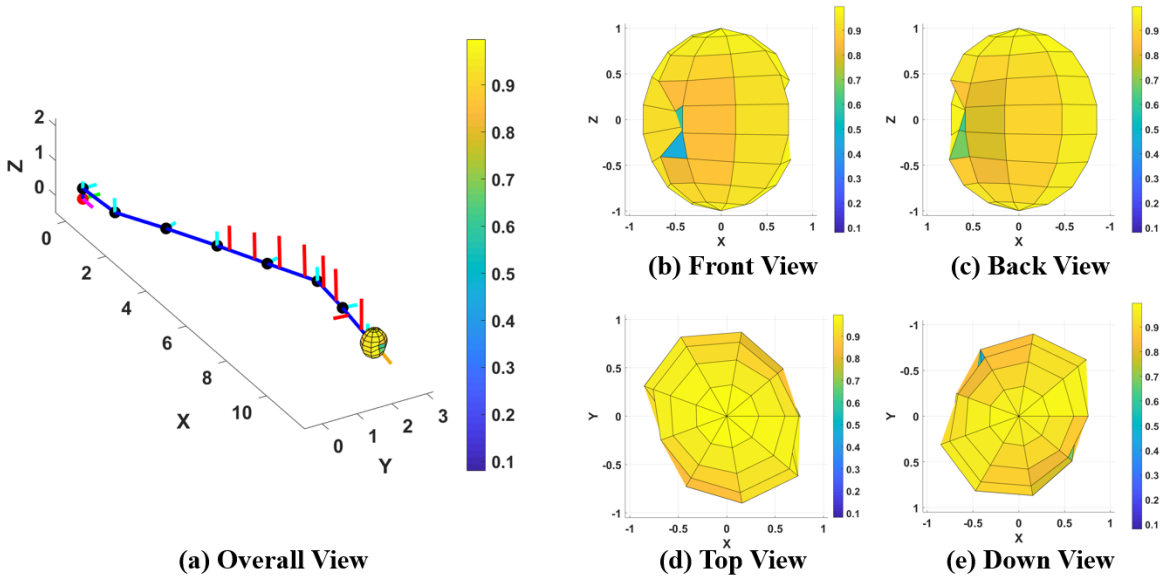

Fig. 3.6. Thrust Drivability Surface of human-experience-based flying watch allocation in the static object holding mission. (a) Overall view of flying watch allocation, end effector reaction force, and the corresponding average TDS. (b) Front view of TDS. (c) Back view of TDS. (d) Top view of TDS. (e) Down view of TDS.

horizontal plane and all other flying watches are attached with thrust generating directions in the vertical planes containing the corresponding attached links (when the arm is observed in Fig. 3.4 configuration). However, in the AOWS based design, the thrust generating direction of the 4th flying watch is partially tilted (50.71°) to the horizontal plane and all other flying watch have thrust generating directions close to vertical plane containing the corresponding attached links (when the arm is observed in Fig. 3.4 configuration). This means AOWS choose to use the 4th flying watch instead of the 7th one to counteract horizontal wind, which is better for two reasons. Firstly, since vertical external forces (arm gravity=88.1N and vertical end effector reaction force=15N) influence the arm much more significantly than the horizontal external force (wind load=10N), it is better to use distal flying watches with longer moment arms to counteract vertical external forces. Other slightly tilted flying watch can also help counteracting horizontal wind force. Secondly, the partially tilted 4th flying watch can also counteract vertical external forces when there is no wind. However, in human-experience-

based design, since the thrust generating direction of the 7 th flying watch is on the horizontal plane, when there is no horizontal wind, the 7th flying watch itself will be a load to the arm.

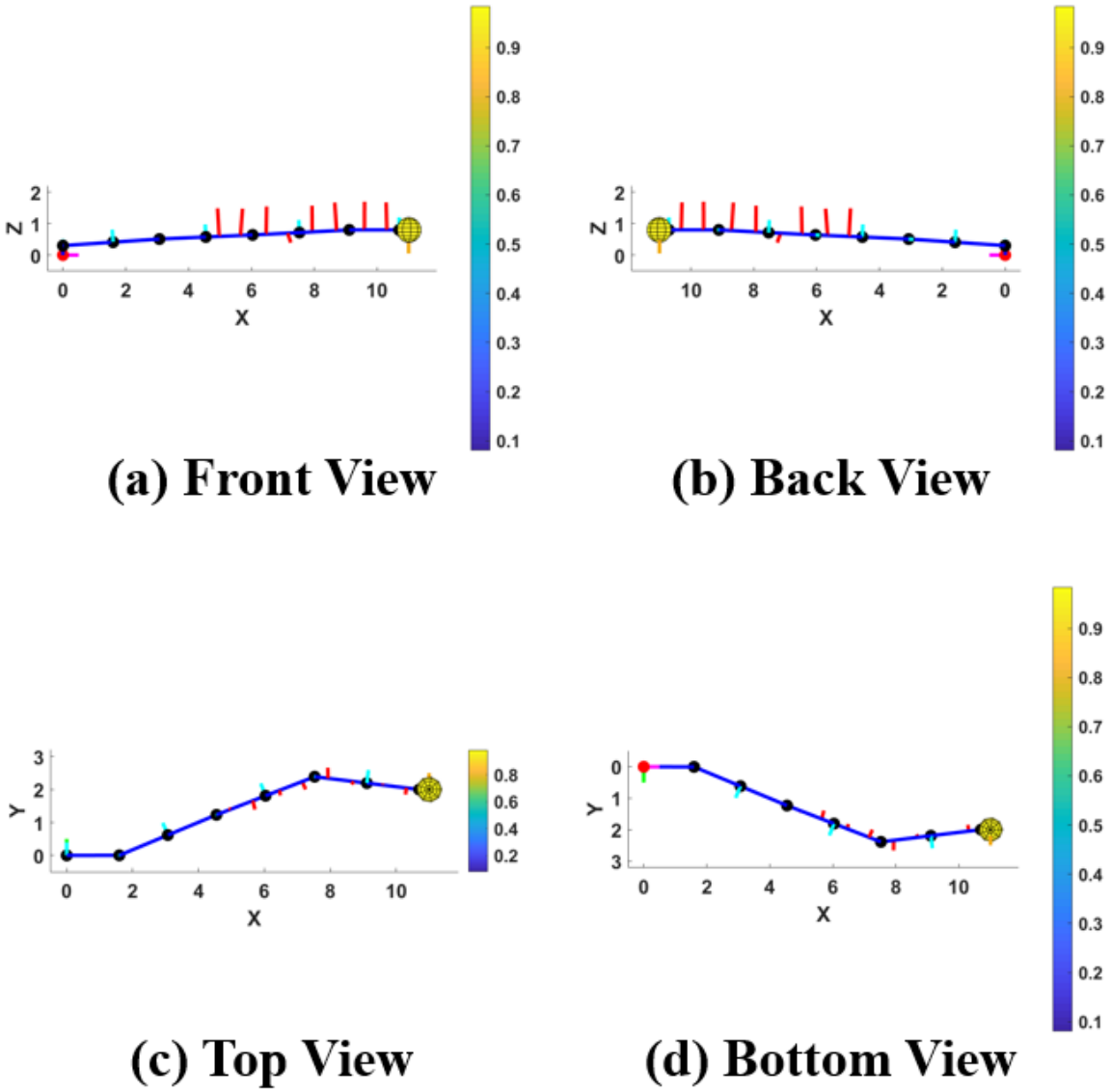

Fig. 3.7. AOWS-based flying watch allocation in the static object holding mission. (a) Front view. (b) Back view. (c) Top view. (d) Bottom view.

Also, we can observe from Table 3.1 and Fig. 3.5-3.8 that in the AOWS based allocation, the thrust generating directions of the two flying watches on the same link forms skew lines (lines that are not parallel and not intersecting). As a result, the generated thrusts along the skew lines are capable to form equivalent forces and torques (regarding the DH frame of the closest proximal joint) with diverse directions and magnitudes, which can counteract

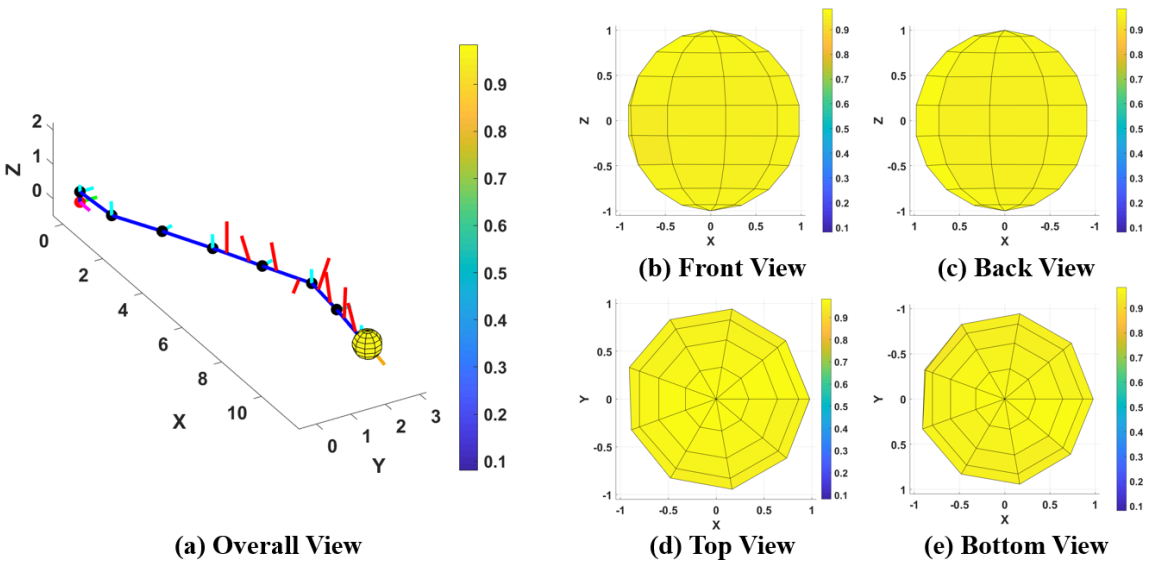

Fig. 3.8. Thrust Drivability Surface of AOWS-based flying watch allocation in the static object holding mission. (a) Overall view flying watch allocation, end effector reaction force, and the corresponding average TDS. (b) Front view of TDS. (c) Back view of TDS. (d) Top view of TDS. (e) Down view of TDS.

unexpected effect induced forces and torques and prevent them from further propagating to more proximal links. However, in the human-experience-based design, the thrust generating directions of flying watches on the same link (except the 8th link) are parallel. For a given arm configuration, the resulting parallel thrusts can only form equivalent forces and torques (regarding the DH frame of the closest proximal joint) with fixed directions, which may fail to counteract unexpected effect induced forces and torques with unknown directions and magnitudes. The advantage of the AOWS design for counteracting unexpected effect can also be seen from TDSs in Fig. 3.5-3.8. The TDS of AOWS design is clearly closer to a unit sphere than that of human-experience-based design. We can learn from the AOWS design that the diversity of thrust generating directions of flying watches is very important for counteracting unexpected end effector reaction forces.

To quantitively evaluate the ability of the AOWS based allocation to counteract known effects (the arm gravity, the object gravity, and the known wind loads), we used the human-experience-based allocation as the benchmark case and compute the average reduction rate of

all representative situations based on (3.1). We found the average reduction rate of the AOWS based allocation over the human-experience-based allocation is 37.43%. Therefore, the AOWS based allocations can counteract known effects significantly better than the human-experience-based allocation.

To quantitively evaluate the ability of the AOWS based allocation to counteract unknown end effector reaction forces, we calculated the Thrust Drivability of AOWS based allocation and human-experience-based allocation in all directions ($\boldsymbol{\omega}_{all}$ = [0, π, 0,2π]), in the left region ($\boldsymbol{\omega}_{left}$ = [$\frac{\pi}{4}$, $\frac{3\pi}{4}$, $\frac{3\pi}{4}$, $\frac{5\pi}{4}$]), in the right region ($\boldsymbol{\omega}_{right}$ = [$\frac{\pi}{4}$, $\frac{3\pi}{4}$, 0, $\frac{\pi}{4}$] ∩ [$\frac{\pi}{4}$, $\frac{3\pi}{4}$, $\frac{7\pi}{4}$, 2π]), in the front region ($\boldsymbol{\omega}_{front}$ = [$\frac{\pi}{4}$, $\frac{3\pi}{4}$, $\frac{5\pi}{4}$, $\frac{7\pi}{4}$]), in the back region ($\boldsymbol{\omega}_{back}$ = [$\frac{\pi}{4}$, $\frac{3\pi}{4}$, $\frac{\pi}{4}$, $\frac{3\pi}{4}$]), in the top region ($\boldsymbol{\omega}_{top}$ = [0, $\frac{\pi}{4}$, 0,2π]), and in the bottom region ($\boldsymbol{\omega}_{bottom}$ = [$\frac{3\pi}{4}$, π, 0,2π]). The Thrust Drivability results are shown in Table 3.2. From Table 3.2, we can see AOWS-based design performs better than human-experience-based design in counteracting unknown effect in different directions. The Thrust Drivability of all directions of the AOWS based design (0.946) is 31.6% higher than that of the human-experience-based design (0.719). Such direct comparison between TDs of different allocations is meaningful because according to (3.6), both Thrust Drivability used the same benchmark, which is the arm in configuration $\boldsymbol{q}_{m1}$ with no flying watch assistance. We can also understand the strong and weak regions of one allocation by comparing Thrust Drivability of different regions of the allocation itself. We can observe from Table 3.2 that the strong regions of both human-experience-based allocation and AOWS-based allocation are top and bottom regions. The human-experience-based allocation is relatively weak in left and right regions while the AOWS-based allocation is relatively weak in front and back regions. Such information is helpful for arm operation since the operator

should pay attention to avoid obstacles or other disturbances that may result in end effector reaction forces in weak regions of the deployed flying watch attachment allocation.

Table 3.2. THRUST DRIVABILITY OF STATIC OBJECT HOLDING MISSION

Direction Region	All	Top	Bottom	Left	Right	Front	Back
Human-Experience	0.719	0.859	0.859	0.558	0.539	0.801	0.710
AOWS	0.946	0.969	0.969	0.927	0.951	0.923	0.917

Finally, we simulate static holding missions under four more combinations of end effector positions (for orientation, the end effector frame is always aligned with the base frame) and known end effector reaction forces (more specifically object gravity). There are two purposes for doing that. Firstly, it helps verifying that AOWS can stably generate reasonable flying watch attachment allocations for static object holding missions under different conditions. Secondly, it helps understanding AOWS performance of object manipulation missions under different conditions as well. We will evaluate AOWS performance in an object manipulation mission in the next subsection and from Problem 3.3, we can see that AOWS essentially treats an object manipulation mission as a combination of multiple static object holding mission components. As a result, we can imagine the AOWS performance of an object manipulation mission depends on AOWS performance of the corresponding static object holding mission components. The reduction rate (ζ) and Thrust Drivability in all directions (D_{all}) of all five conditions up to now for static object holding missions are summarized in Table 3.3. Please note that since we always use the same initial parameters for the inverse kinematics, the arm configurations only depend on the end effector positions.

Table 3.3. AOWS PERFORMANCE UNDER DIFFERENT CONDITION

Object Gravity (N)	End Effector Position (m)	ζ (Reduction Rate)	D_{all} (Human Experience)	D_{all} (AOWS)
10	[11,2,0.8]	2.16%	0.719	0.947
15	[5,2,0.8]	64.35%	0.775	0.909
15	[8,2,0.8]	23.28%	0.791	0.928
15	[11,2,0.8]	37.43%	0.719	0.946
20	[11,2,0.8]	35.58%	0.719	0.946

From Table 3.3, we can firstly see that AOWS-based designs perform better than the human-experience-based design in counteracting both known reaction forces and unexpected end effector reaction forces under different conditions. Secondly, it is interesting to notice that for the same end effector position of [11,2,0.8], when the object gravity changes from 20 N to 15 N, there is no significant change in reduction rate and when the object gravity changes the same amount from 15 N to 10 N, the reduction rate drops significantly. We analyzed the joint loads under different object gravity and found the reason is that the human-experience-based design can counteract object gravity under 10 N very well and there is very small room left for AOWS to improve. However, when the object gravity is larger than 10 N, the joint loads of the human-experience-based allocation increase very rapidly and there is larger room for AOWS to improve. Therefore, when the object gravity is small enough, the AOWS-based design and the human-experience-based design will have similar performance for counteracting known reaction forces.

3.5.2. Object Manipulation Mission

In this mission, the arm will manipulate an object with 15 N gravity from position [7,2,0] to position [7,-2,0] following an ellipse trajectory with parametric equation of $(x, y, z) = (7, 2cos(\pi\xi_{m2}), sin(\pi\xi_{m2}))$, where $\xi_{m2} \in [0,1]$. The end effector frame will always

coincide with the base frame. During the mission, a 10 N wind load with a direction of positive Y axis direction of the base frame (probability=30%) and negative Y axis direction of the base frame (probability=30%) will act on the end effector. To use AOWS, we need to construct a WSM for the mission. We firstly do trajectory planning. Since there is no obstacle, trajectory planning can be done by generating a sequence of arm configurations and interpolating those configurations with certain time function. We evenly discretize ξ_{m2} with a step size of 0.1 to generate 11 trajectory sample points and then solve inverse kinematics for these points while forcing the configurations of adjacent points to be as close as possible to generate a sequence of arm configurations. Since a WSM does not concern when a representative situation happens, time interpolation of the sequence of arm configuration is not necessary. The set of arm configurations $\boldsymbol{Q}_{m2} = \{\boldsymbol{q}_1, \dots, \boldsymbol{q}_{11}\}$ is shown in Fig. 3.9.

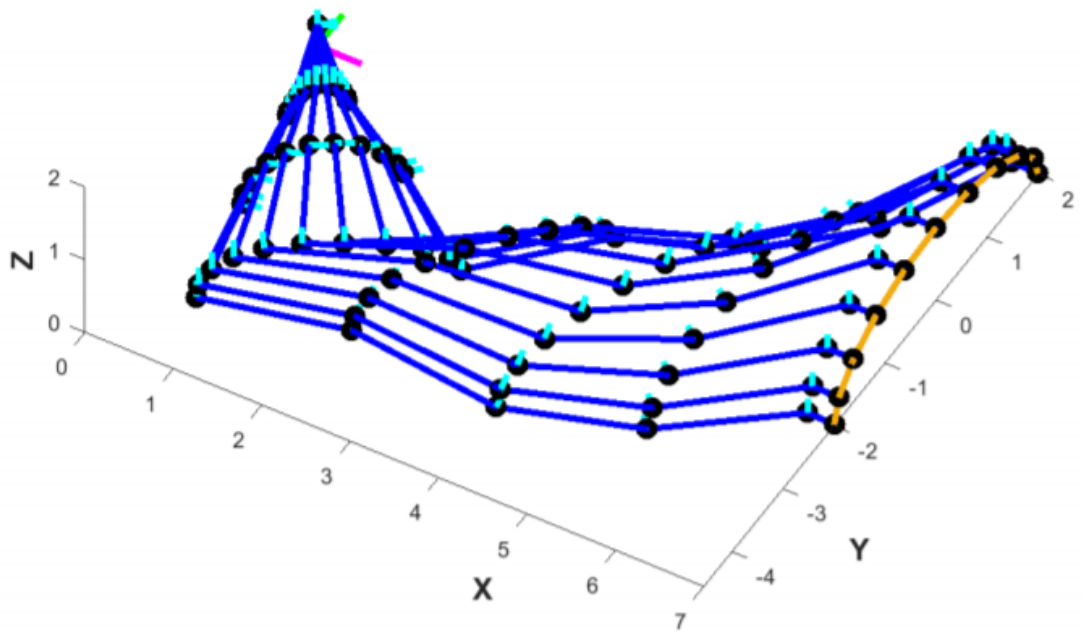

Fig. 3.9. The sequence of arm configurations in the object manipulation mission.

The set of possible end effector reaction forces is $\boldsymbol{F}_{m2} = \{\boldsymbol{F}_1, \boldsymbol{F}_2, \boldsymbol{F}_3\}$, where $\boldsymbol{F}_1 = [0,0,-15]N$, $\boldsymbol{F}_2 = [0,10,-15]N$, $\boldsymbol{F}_3 = [0,-10,-15]N$. The set of representative

situations is $\boldsymbol{E}_{m2} = \boldsymbol{Q}_{m2} \times \boldsymbol{F}_{m2}$, where "$\times$" is Cartesian product. We assume the configurations in $\boldsymbol{Q}_{m2}$ are equally important and the importance of each possible end effector reaction forces depends on their probabilities. Therefore, for the 33 representative situations in $\boldsymbol{E}_{m2}$, those situations include $\boldsymbol{F}_1$ have importance factors of $1/11 \times 0.4 = 2/55$ and those situations include $\boldsymbol{F}_2$ or $\boldsymbol{F}_3$ have importance factors of $1/11 \times 0.3 = 3/110$. After defining the importance factor set $\boldsymbol{P}_{m2}$, we can construct a WSM $\boldsymbol{\Pi}_{m2} = (\boldsymbol{E}_{m2}, \boldsymbol{P}_{m2})$. In addition to those known effects, such as the arm gravity, the object gravity, and the known wind load, we also hope that the flying watch allocation can counteract unexpected effects, such as unexpected wind loads and unexpected collisions. Therefore, we set the direction region of unexpected end effector reaction forces as $\boldsymbol{\omega}_{m2}$ = [0, π, 0, 2π] with drivability weight factor $\alpha_{m2} = 1$. We set the unexpected effect weight factor $\beta_{m2} = 0.5$.

We input these design parameters to AOWS and the AOWS-based allocation and the human-experience-based allocation are shown in Table 3.4 for comparison. The flying watch positions and orientations are described using simplified DHAD. We also draw human-experience-based allocation and AOWS-based allocation in the 17th representative situation ($\boldsymbol{e}_{17} = (\boldsymbol{q}_6, \boldsymbol{F}_2)$, where $\boldsymbol{q}_6 = [-1.06, -0.41, -0.04, 0.27, 1.56, 0.26, 0.54, -0.28, -0.98]$ rad

Table 3.4. AOWS-BASED AND HUMAN-EXPERIENCE-BASED ALLOCATIONS OF OBJECT MANIPULATION MISSION

Flying Watch Index	1	2	3	4	5	6	7	8
AOWS (Position) (m)	-1.12	-0.48	-1.16	-0.38	-1.20	-0.42	-1.14	-0.41
AOWS (Orientation) (°)	-3.24	-10.95	86.39	125.00	179.76	-1.81	80.51	96.41
Human-Experience (Position) (m)	-1.20	-0.40	-1.20	-0.40	-1.20	-0.40	-1.20	-0.40
Human-Experience (Orientation) (°)	0.00	0.00	90.00	90.00	0.00	0.00	0.00	90.00

and $\boldsymbol{F}_2 = [0,10,-15]\ N$) in Fig. 3.10-3.13. The meaning of colors is the same as that of Fig. 3.5-3.8.

From Table 3.4 and Fig. 3.10-3.13 and compared with the human-experience-based allocation, we can observe several patterns of AOWS similar to that of the static object holding mission. Firstly, AOWS moves the 1st, 3rd , and 7th flying watches significantly closer (≥ 4 cm) to the end effector to obtain longer moment arms. Secondly, AOWS makes the thrust generating directions of all flying watches close to the vertical planes containing the corresponding attached links and tilts the thrust generating directions of the 2nd , 4th , and 7th flying watches to the horizontal planes (≥ 9°) (when the arm is observed in Fig. 3.4 configuration). In such allocation, all flying watches focus more on counteracting the much larger vertical effect (vertical end effector reaction forces and arm gravity) while the tilted flying watches can also counteract horizontal wind force. Thirdly, the thrust generating directions of flying watches on the same link also form skew lines. As we have discussed in the static object holding mission, such diversified thrust generating directions of flying watches can help counteracting unknown end effector reaction forces. The advantage of diversifying flying watch orientation can also be seen from TDSs in Fig. 3.10-3.13. The TDS of the AOWS design is clearly closer to a unit sphere than that of the human-experience-based design. To quantitively evaluate the performance of AOWS based design to counteract known end effector reaction forces, we calculated the average reduction rates in the same way as in the static object holding mission. The average reduction rate of the AOWS based design (using the human-experience-based design as benchmark) is 22.01%. Therefore, AOWS based design performs better than human-experience-based design in counteracting known end effector reaction forces.

To quantitatively evaluate the performance of AOWS based design to counteract unknown end effector reaction forces, we also calculated Thrust Drivability in different direction regions

as shown in Table 3.5. The definition of these direction regions is the same as that of the static object holding mission. We can see from Table 3.5 that the all-direction Thrust Drivability of AOWS based design (0.922) is 24.6% higher than that of the human-experience-based design (0.740). We can also understand the strong and weak regions of each design by comparing Thrust Drivability of the design itself. For the human-experience-based allocation, the weak regions are the left and right regions and the strong regions are the front and back regions. For the AOWS based allocation, the weak regions are the front and back regions and the top, bottom, left, and right regions have similar Thrust Drivability.

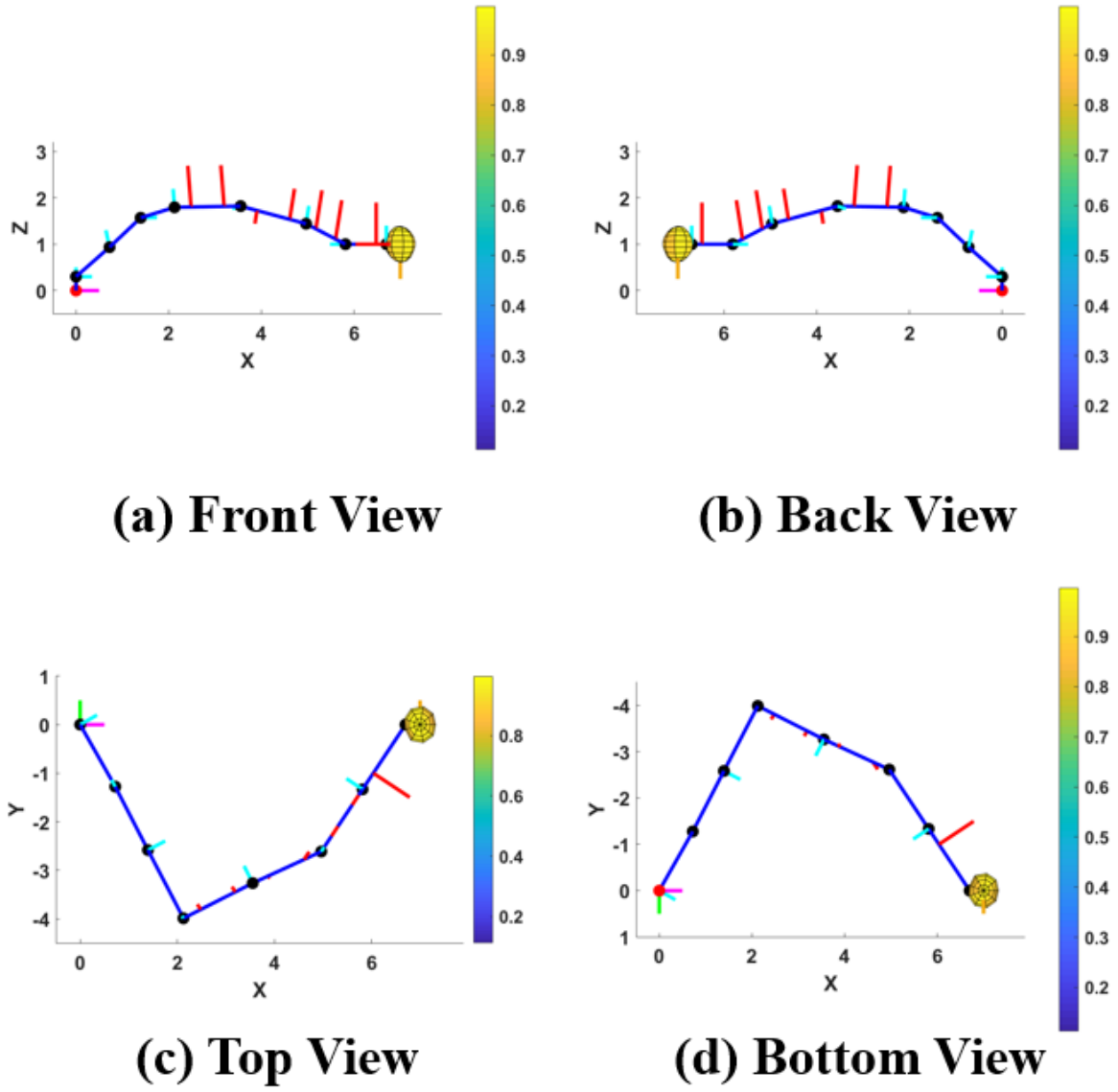

Fig. 3.10. Human-experience-based flying watch allocation in the object manipulation mission. (a) Front view. (b) Back view. (c) Top view. (d) Bottom view.

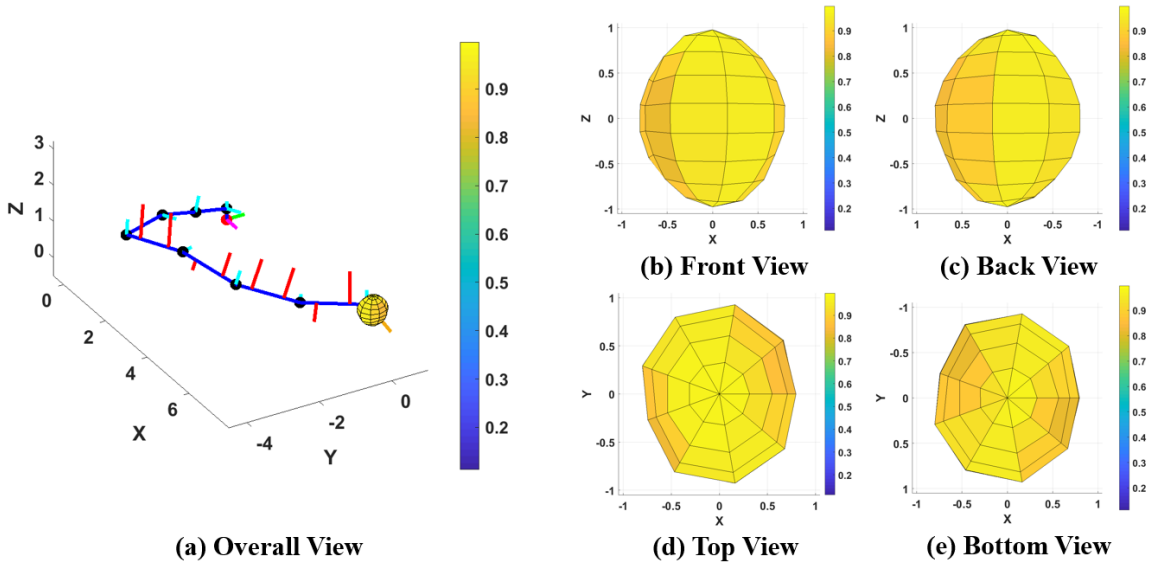

Fig. 3.11. Thrust Drivability Surface of human-experience-based flying watch allocation in the object manipulation mission. (a) Overall view of flying watch allocation, end effector reaction force, and the corresponding average TDS. (b) Front view of TDS. (c) Back view of TDS. (d) Top view of TDS. (e) Down view of TDS.

Table 3.5. THRUST DRIVABILITY OF OBJECT MANIPULATION MISSION

Direction Region	All	Top	Bottom	Left	Right	Front	Back
Human-Experience	0.740	0.800	0.806	0.587	0.617	0.847	0.861
AOWS	0.922	0.938	0.937	0.927	0.939	0.881	0.876

3.6. Summary

In this Chapter, to facilitate mission-dependent long-reach robotic arm enhancement, an automated design method for designing attachment allocations of flying watches, called Allocation Optimization based on Weighted Situations (AOWS) is proposed. Given a mission

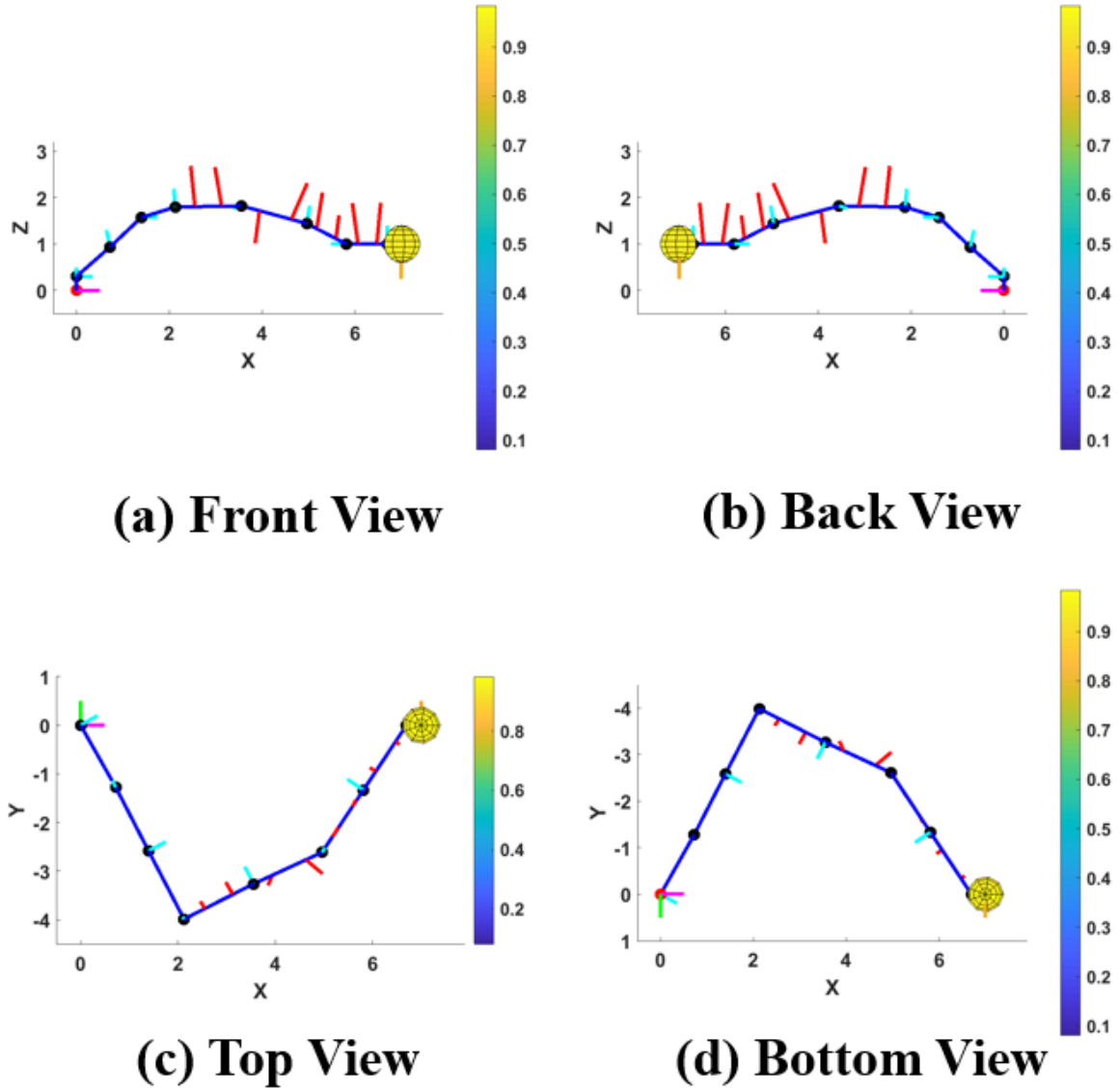

Fig. 3.12. AOWS-based flying watch allocation in the object manipulation mission. (a) Front view. (b) Back view. (c) Top view. (d) Bottom view.

description, AOWS can generate flying watch attachment allocations counteracting both known and unexpected end effector reaction forces as well as arm gravity. The ability of AOWS to consider unexpected end effector reaction forces attributes to a novel performance metric proposed in this dissertation, called Thrust Drivability, which measures the ability of a flying watch attachment allocation to counteract unknown end effector reaction forces. AOWS enables fast customization of flying watch attachment allocations for different missions. To the best of our knowledge, no such automated design method like AOWS and performance metric like Thrust Drivability have been explored in the literature. Based on simulations of two typical

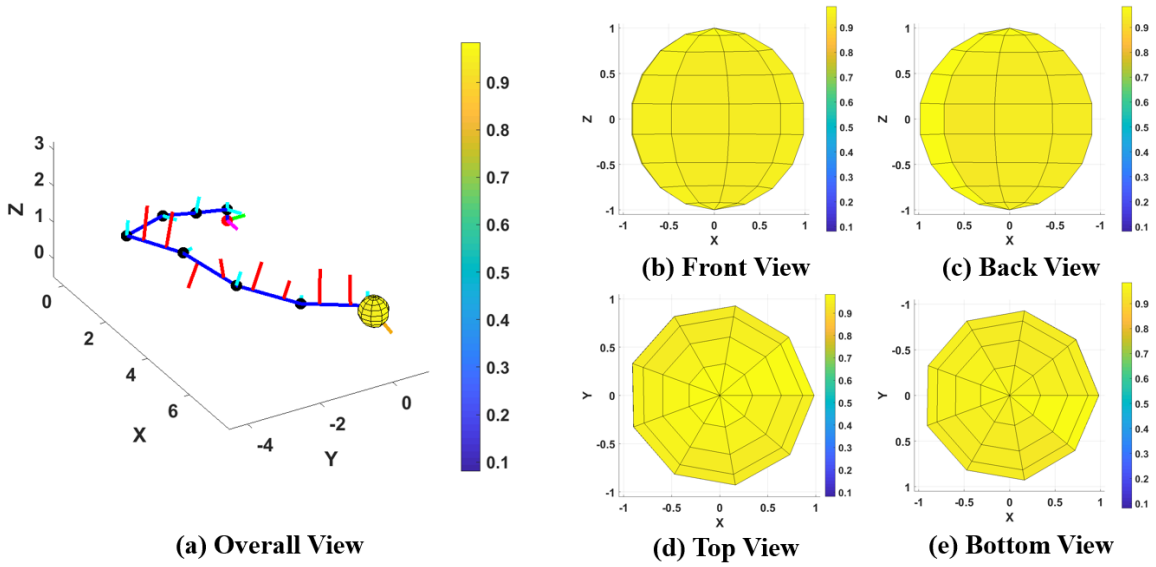

Fig. 3.13. Thrust Drivability Surface of AOWS-based flying watch allocation in the object manipulation mission. (a) Overall view of flying watch allocation, end effector reaction force, and the corresponding average TDS. (b) Front view of TDS. (c) Back view of TDS. (d) Top view of TDS. (e) Down view of TDS.

arm missions (static object holding mission and object manipulation mission), We have shown that AOWS based flying watch attachment allocations have much better performance than human-experience-based allocations.

There are several interesting potential research directions related to thrust drivability theory and AOWS. Firstly, as we mentioned in Chapter 1, thrust-driven robotic arms, like Hiryu [13], [15] and LASDRA [14], can be regarded as special cases of flying watch enhanced arm when all loads on passive joint are counteracted by flying watches and flying watch allocations are not allowed to be customized. As a result, the thrust drivability theory and AOWS should be applicable to those thrust-driven arms. It would be interesting to use thrust drivability theory to analyze the properties of those existing thrust-driven arms and use AOWS to design new thrust-driven arms that are robust to unexpected environmental perturbation. Secondly, although we have verified the performance of AOWS using simulations, it would be interesting to test AOWS-based flying watch attachment allocations on physical robotic arms. Thirdly, TDS and Thrust Drivability currently only considers unexpected end effector reaction force on

the end effector. However, in practice unexpected reaction force due to wind and collision may also be exerted on the arm body. It would be interesting to extend TDS and Thrust Drivability to consider unexpected reaction forces on the arm body.

In addition, the AOWS-based flying watch allocation designs are currently compared with the human-experience-based allocation designed by me. In the future, to more objectively evaluate AOWS, the AOWS-based flying watch allocation designs should be compared with human-experience-based allocations designed by several well-trained mechanical engineers who understand the working principle of a flying watch.

Although the objectivity of AOWS evaluation needs improvement, it can be acknowledged that the current human-experience-based flying watch allocation is a reasonable design based on its design rationale (described in the third paragraph in subsection 3.5). Since the simulations shows AOWS stably generates better designs compared with that human-experience-based design, it is safe to acknowledge AOWS, as an automated design tool, can quickly generate flying watch allocation design with reasonable quality.

4. Model-based Flying Watch Thrust Planning

In previous Chapters, the mechanical design and attachment allocation of flying watch are introduced. The next important problem would be how to regulate the thrusts of flying watches. In this Chapter, a model-based offline thrust planner called Watch-Actuator Cooperation for Arm Enhancement (WACAE), will be proposed to answer this question. WACAE requires a precise Equation of Motion of a robotic arm, arm trajectory in a mission, and end effector reaction forces in the mission to calculate desired thrusts that can reduce arm joint loads. Then flying watches are controlled to generate the desired thrusts.

We will see that WACAE features two levels of watch actuator cooperation. Also, since all watch thrusts are calculated before a mission, WACAE can be used to rehearse a mission and determine whether a mission will succeed or not.

4.1. Watch Actuator Cooperation for Arm Enhancement

In order to enhance arm strength, the loads of the actuators need to be reduced using the effects of flying watches. As understood from the flying watch EoM (2.21) in Section 2.6, the effect of flying watch on actuator loads depends on two factors. The position and orientation of flying watches (as represented by attachment style matrix $\boldsymbol{R}$) and the thrust magnitudes (as represented by $\boldsymbol{s}$). From those two factors, we can imagine two levels of cooperation between watch and arm actuators. The first level WACAE (WACAE-I) is only flying watches adapt their thrust magnitudes to minimize the actuator loads. In such case, only the magnitudes of flying watch thrusts are optimized. The second level WACAE (WACAE-II) is not only do watches adapt their thrusts but also actuators corporately position the watches to the optimal positions and orientations to minimize the actuator loads. In such cases, both watch thrust

magnitudes and watch positions and orientations are optimized. This higher level of cooperation would more effectively reduce the actuator loads. However, it cannot be applied when the arm is not redundant or when the operator wants more control on the arm configuration. We formulate the mentioned two levels cooperation problem as follows and call such problem as Watch Actuator Cooperation for Arm Enhancement (WACAE).

Problem 4.1: Watch-Actuator Cooperation for Arm Enhancement

$$\min_{\boldsymbol{s},\boldsymbol{q}} \|\tilde{\boldsymbol{\tau}}(\boldsymbol{s},\boldsymbol{q})\|_\infty \;\; s.t.\; \boldsymbol{s}_l \le \boldsymbol{s} \le \boldsymbol{s}_u, \boldsymbol{q}_l < \boldsymbol{q} < \boldsymbol{q}_u, \boldsymbol{p}_d = f(\boldsymbol{q})$$

$\boldsymbol{s}_l$ and $\boldsymbol{s}_u$ are the lower and upper bounds of thrust magnitudes $\boldsymbol{s}$. $\boldsymbol{q}_l$ and $\boldsymbol{q}_u$ are the lower and upper bounds of generalized coordinates $\boldsymbol{q}$ resulting from mechanism constraints. $\boldsymbol{p}_d$ is the desired end effector position and orientation. f is a function representing forward kinematics. For the first level cooperation, generalized coordinates $\boldsymbol{q}$ can be regard as a constant. $\tilde{\boldsymbol{\tau}}$ is the normalized joint load vector computed from (2.23) (we assume quasistatic static condition in this Chapter). In the rest of this Section, for simplicity, the cost function $\|\tilde{\boldsymbol{\tau}}(\boldsymbol{s},\boldsymbol{q})\|_\infty$ is denoted as $C(\boldsymbol{s},\boldsymbol{q})$.

WACAE is about optimizing thrust magnitudes and generalized coordinates constrained by forward kinematics, watch thrust capacity, and arm mechanism in order to minimize the maximum normalized actuator load. The WACAE solution makes the watches cooperate with arm actuators to reduce actuator loads.

WACAE is a nonconvex and nonlinear optimization problem. For such problem, a local optimal solution can theoretically be found by several existing optimization methods, such as SNOPT [51] and LOQO [52], as well as arm configuration optimization methods EEIK [53] and ODLS [54]. Since proposing a new optimization solver or comparing the performance of existing optimization methods is not the interest of this dissertation, for simplicity, we used a modification of our previous arm configuration optimization methods EEIK [53] and ODLS

[54] to solve WACAE. In the following, we present this modification as an example solution of WACAE in order to show the solvability of WACAE and for future comparison and improvement. The major difference between the example WACAE solution and EEIK and ODLS is that the example solution includes additional procedures to optimize thrusts and handle upper and lower bounds of thrusts and generalized coordinates.

In order to make this dissertation self-contained, we will first briefly explain Lockable Inverse Kinematics (LIK) and Automatic Optimizable Dimension Searching (AODS) proposed in [53], [54], which are components of EEIK and ODLS. After that we will present the example solution of WACAE.

Firstly, regarding LIK, it is about solving inverse kinematics while fixing certain generalized coordinates to given values. LIK is previously solved by Lockable Damped Least Squares method (LDLS) in [53], [54]. However, there is no bound on generalized coordinates. Those bound are necessary for solving WACAE in this dissertation. Therefore, we write LIK as the following optimization problem and use interior point method to solve it. For simplicity, we express the process of solving LIK as $\boldsymbol{q} = \text{LIK}(\boldsymbol{I}_l, \boldsymbol{L}, \boldsymbol{p}_d, \boldsymbol{V}_l, \boldsymbol{V}_u)$.

Problem 4.2: Lockable Inverse Kinematics (LIK):

$$\min_{\boldsymbol{V}} \|\boldsymbol{p}_d - f(\boldsymbol{V}; \boldsymbol{L})\|_2 \;\; s.t. \; \boldsymbol{V}_l < \boldsymbol{V} < \boldsymbol{V}_u$$

$\boldsymbol{I}_l$ is the index of the locked generalized coordinates. $\boldsymbol{V}$ is the unlocked generalized coordinates and $\boldsymbol{L}$ is the locked generalized coordinates. $\boldsymbol{q}$ is a vector including all generalized coordinates. $f(\boldsymbol{V}; \boldsymbol{L})$ is the forward kinematics, which is a function of $\boldsymbol{V}$ parameterized by $\boldsymbol{L}$. $\boldsymbol{V}_l$ and $\boldsymbol{V}_u$ are vectors respectively representing the lower and upper bounds of $\boldsymbol{V}$. The optimization problem tries to minimize the Euclidean distance between the desired and current end effector positions and orientations given the bounds on unlocked generalized coordinates $\boldsymbol{V}$. $\boldsymbol{q} = \text{LIK}(\boldsymbol{I}_l, \boldsymbol{L}, \boldsymbol{p}_d, \boldsymbol{V}_l, \boldsymbol{V}_u)$ essentially gives the relation between locked generalized

coordinates (e.g. locked joint angles) and end effector position and orientation. In WACAE, LIK will be used to lock independent redundant joint angles of a redundant arm. That helps simplify optimization variable from full dependent joint angles $\boldsymbol{q}$ to fewer independent redundant joint angles $\boldsymbol{L}$.

We will also need Inverse Kinematics (IK) with generalized coordinate bounds to compute arm configuration when the arm configuration does not need optimization. Similarly, we can write IK with bounds as the following optimization problem and use interior point method to solve it. $f(\boldsymbol{q})$ is still the forward kinematics, which we express it as a function of $\boldsymbol{q}$.

Problem 4.3: Inverse Kinematics (IK):

$$\min_{\boldsymbol{q}} \|\boldsymbol{p}_d - f(\boldsymbol{q})\|_2 \ \ s.t.\ \boldsymbol{q}_l < \boldsymbol{q} < \boldsymbol{q}_u$$

Secondly, regarding AODS, it is a method to automatically search for optimizable dimensions of the generalized coordinates. More specifically, given the desired end effect position and orientation $\boldsymbol{p}_d$ and the arm configuration $\boldsymbol{q}$, AODS searches for N_r dimensions of generalized coordinates indexed by $\boldsymbol{\xi}$ that can be optimized to minimize a certain cost function C.

The pseudocode of AODS is shown in Algorithm 4.1. Initially, in step 1, AODS uses LIK to add a small value ϵ to each dimension of $\boldsymbol{q}$ and record how much the cost function changes

Algorithm 4.1 (AODS): $\boldsymbol{\xi}$=AODS ($\boldsymbol{p}_d, \boldsymbol{q}, N_r, \boldsymbol{q}_l, \boldsymbol{q}_u$)

STEP 1 (Compute Dimensional Impact $\boldsymbol{\eta}$ of $\boldsymbol{q}$ on C):

FOR i=1: LENGTH($\boldsymbol{q}$)

$\boldsymbol{s} = \boldsymbol{0}$

$\boldsymbol{\eta}(i) = (C(\boldsymbol{s}, \text{LIK}(i, \boldsymbol{q}(i) + \epsilon, \boldsymbol{p}_d, \boldsymbol{q}_l(i^c), \boldsymbol{q}_h(i^c))) - C(\boldsymbol{s}, \text{LIK}(i, \boldsymbol{q}(i), \boldsymbol{p}_d, \boldsymbol{q}_l(i^c), \boldsymbol{q}_u(i^c))))/\epsilon$

END_FOR

STEP 2 (Select Optimizable Dimensions):

Select N_r non-zero dimensions of $\boldsymbol{\eta}$ and the corresponding index vector is $\boldsymbol{\xi}$.

compared to the added small value. i^c means the complement index of i, which is the index of all generalized coordinates other than i. For a certain dimension, if the change is not zero, this dimension can influence the cost function and is optimizable. Then in step 2, N_r optimizable dimensions of $\boldsymbol{q}$ indexed by $\boldsymbol{\xi}$ are selected.

After reviewing LIK and AODS, we move forward to introduce the example WACAE solution. The major difficulty of solving WACAE is that the generalized coordinates $\boldsymbol{q}$ are constrained by nonlinear and nonconvex forward kinematics and each dimension of $\boldsymbol{q}$ is not independent. We firstly used LIK to eliminate the forward kinematics and simplify WACAE to the following problem.

Problem 4.4: Simplified WACAE:

$$\min_{\boldsymbol{s},\boldsymbol{q}_r} \left\| \tilde{\boldsymbol{\tau}}\left(\boldsymbol{s}, \mathrm{LIK}\left(\boldsymbol{\xi}, \boldsymbol{q}_r, \boldsymbol{p}_d, \boldsymbol{q}_l(\boldsymbol{\xi}^c), \boldsymbol{q}_u(\boldsymbol{\xi}^c)\right)\right) \right\|_\infty \; s.t. \; \boldsymbol{s}_l \le \boldsymbol{s} \le \boldsymbol{s}_u, \boldsymbol{q}_l(\boldsymbol{\xi}) \le \boldsymbol{q}_r \le \boldsymbol{q}_u(\boldsymbol{\xi})$$

In the simplified WACAE, $\boldsymbol{\xi}$ is the index of the optimizable redundant dimensions $\boldsymbol{q}_r$, which can be obtained using AODS. After simplification, the optimization variables are changed from $\boldsymbol{q}$ to $\boldsymbol{q}_r$, each dimension of which is independent. The simplified WACAE only has box shape constraints on $\boldsymbol{s}$ and $\boldsymbol{q}_r$ and can be solved with gradient descent. Since $\boldsymbol{s}$ and $\boldsymbol{q}_r$ have different physical meanings and could be high dimensional, in order to avoid ill-conditioned hessian matrix and reduce the dimension of each optimization step, we update $\boldsymbol{s}$ and $\boldsymbol{q}_r$ iteratively using gradient descent. The pseudocode of the example solution is shown in Algorithm 4.2.

Algorithm 4.2: $\{\boldsymbol{s}^*, \boldsymbol{q}^*\}$ =WACAE_SOLUTION $(\boldsymbol{p}_d, \boldsymbol{s}_l, \boldsymbol{s}_u, \boldsymbol{q}_l, \boldsymbol{q}_u, \boldsymbol{\xi})$

STEP 1 (Initiation):

Set $\boldsymbol{q}_l(\boldsymbol{\xi}) \leq \boldsymbol{q}_0(\boldsymbol{\xi}) \leq \boldsymbol{q}_u(\boldsymbol{\xi}), \boldsymbol{s}_l \leq \boldsymbol{s} \leq \boldsymbol{s}_u$

$\boldsymbol{q}$ = LIK($\boldsymbol{\xi}$, $\boldsymbol{q}_0(\boldsymbol{\xi})$, $\boldsymbol{p}_d, \boldsymbol{q}_l(\boldsymbol{\xi}^c), \boldsymbol{q}_u(\boldsymbol{\xi}^c)$)

STEP 2 (Update $\boldsymbol{s}$):

$\boldsymbol{s}_{back} = \boldsymbol{s}$

$\boldsymbol{\delta}_s = \nabla_s C(\boldsymbol{s}, \boldsymbol{q})$

t_{WACAE}=BLS($\boldsymbol{s}$, -$\boldsymbol{\delta}_s, C(\boldsymbol{s}, \boldsymbol{q})$)

FOR i=1:LENGTH($\boldsymbol{s}$)

$\boldsymbol{s}(i) = \boldsymbol{s}(i) - t_{WACAE}\boldsymbol{\delta}_s(i)$

IF $\boldsymbol{s}(i)$ goes beyond $[\boldsymbol{s}_l(i), \boldsymbol{s}_u(i)]$

$\boldsymbol{s}(i) = \boldsymbol{s}(i) + t_{WACAE}\boldsymbol{\delta}_s(i)$

END_IF

END_FOR

IF $C(\boldsymbol{s}, \boldsymbol{q}) > C(\boldsymbol{s}_{back}, \boldsymbol{q})$

$\boldsymbol{s} = \boldsymbol{s}_{back}$

END_IF

STEP 3 (Update $\boldsymbol{q}$):

$\boldsymbol{q}_{back} = \boldsymbol{q}, \quad \boldsymbol{q}_r = \boldsymbol{q}(\boldsymbol{\xi})$

$\boldsymbol{\delta}_{q_r} = \nabla_{q_r} C(\boldsymbol{s}, \text{LIK}(\boldsymbol{\xi}, \boldsymbol{q}_r, \boldsymbol{p}_d, \boldsymbol{q}_l(\boldsymbol{\xi}^c), \boldsymbol{q}_u(\boldsymbol{\xi}^c)))$

t_{WACAE}= BLS($\boldsymbol{q}_r$, -$\boldsymbol{\delta}_{q_r}, C(\boldsymbol{s}, \text{LIK}(\boldsymbol{\xi}, \boldsymbol{q}_r, \boldsymbol{p}_d, \boldsymbol{q}_l(\boldsymbol{\xi}^c), \boldsymbol{q}_u(\boldsymbol{\xi}^c))))$

FOR i=1:LENGTH($\boldsymbol{q}_r$)

$\boldsymbol{q}_r(i) = \boldsymbol{q}_r(i) - t_{WACAE}\boldsymbol{\delta}_{q_r}(i)$

IF $\boldsymbol{q}_r(i)$ goes beyond $[\boldsymbol{q}_l(i), \boldsymbol{q}_u(i)]$

$\boldsymbol{q}_r(i) = \boldsymbol{q}_r(i) + t_{WACAE}\boldsymbol{\delta}_{q_r}(i)$

END_IF

END_FOR

$\boldsymbol{q}$ = LIK($\boldsymbol{\xi}, \boldsymbol{q}_r, \boldsymbol{p}_d, \boldsymbol{q}_l(\boldsymbol{\xi}^c), \boldsymbol{q}_u(\boldsymbol{\xi}^c)$)

IF $C(\boldsymbol{s}, \boldsymbol{q}) > C(\boldsymbol{s}, \boldsymbol{q}_{back})$

$\boldsymbol{q} = \boldsymbol{q}_{back}$

END_IF

STEP 4 (Repetition) :

Repeat STEP2-STEP3 until $C(\boldsymbol{s}, \boldsymbol{q})$ is small enough. Then $\boldsymbol{q}^* = \boldsymbol{q}, \boldsymbol{s}^* = \boldsymbol{s}$

In this pseudocode, the example solution takes desired end effector position and orientation

($\boldsymbol{p}_d$), constraints ($\boldsymbol{s}_l, \boldsymbol{s}_u, \boldsymbol{q}_l, \boldsymbol{q}_u$), and index of optimizable generalized coordinates ($\boldsymbol{\xi}$) as input and outputs the optimal thrust scales ($\boldsymbol{s}^*$) and generalized coordinates $\boldsymbol{q}^*$. In step 1, $\boldsymbol{s}$ and $\boldsymbol{q}$ are initialized to satisfy constraints. $\boldsymbol{q}$ can also be initiated by IK instead of LIK. In step 2-3, $\boldsymbol{s}$ and $\boldsymbol{q}$ are updated iteratively. BLS$(\boldsymbol{x}, \boldsymbol{dir}, \gamma(\boldsymbol{x}))$ in these steps means to search an appropriate step size of $\boldsymbol{x}$ along $\boldsymbol{dir}$ for minimizing γ using backtracking line search [47]. Two kinds of restoring process are added to gradient descent in order to satisfy the box constraints on $\boldsymbol{s}$ and $\boldsymbol{q}$. (1) In updating processes, if some dimension of $\boldsymbol{s}$ or $\boldsymbol{q}_r$ goes beyond constraints, that dimension is restored to its original value. (2) After updating $\boldsymbol{s}$ or $\boldsymbol{q}$, if the cost function increases, then $\boldsymbol{s}$ or $\boldsymbol{q}$ goes back to the original values. With no loss of generality, we explain these restoring processes using step 2. The first kind of restoring process is equivalent to constructing an updating direction $\boldsymbol{\psi}$ by setting some dimensions of the opposite gradient $-\boldsymbol{\delta}_s$ to zero so that $\boldsymbol{s}$ cannot go beyond constraints in those dimensions. If we use a small enough step size $t > 0$ so that the cost function can be linearly approximated, the cost function after updating is $C(\boldsymbol{s} + t\boldsymbol{\psi}, \boldsymbol{q}) \approx C(\boldsymbol{s}, \boldsymbol{q}) + \boldsymbol{\delta}_{\boldsymbol{s}}^{\mathrm{T}}(\boldsymbol{s} + t\boldsymbol{\psi} - \boldsymbol{s}) = C(\boldsymbol{s}, \boldsymbol{q}) + t\boldsymbol{\psi}^{\boldsymbol{T}}\boldsymbol{\delta}_{\boldsymbol{s}}$. Since $\boldsymbol{\psi}^{\boldsymbol{T}}\boldsymbol{\delta}_{\boldsymbol{s}} \leq 0$, $C(\boldsymbol{s} + t\boldsymbol{\psi}, \boldsymbol{q}) \leq C(\boldsymbol{s}, \boldsymbol{q})$. Therefore, if the updating step size $t > 0$ is small enough for linear approximation of the cost function, the first kind of restoring process can reduce the cost function and ensure the box constraints. The second kind of restoring process check whether the updated cost function really decreases in case that the step size is not small enough. In step 4, the iteration stops when some criteria are met. Some simple criteria include setting the maximum number of iterations and the minimum acceptable decrease of the cost function. For the first level watch-actuator cooperation, step 3 can be skipped.

4.2. Simulation Verification

In this Section, we simulate a redundant arm attached with flying watches and check whether the flying watches can reduce the maximum normalized actuator load through watch-actuator cooperation. In the simulations, we applied varieties of external reaction forces to the end effector under different end effector positions and evaluate the effect of flying watches on the maximum normalized actuator loads. In the following, we will first introduce the simulation setup. Then we will detail the simulation process. Finally, we will present and discuss the simulation results.

Regarding the simulation setup, we used Matlab to simulate a 9-DoF arm with 8 flying watches attached as shown in Fig. 4.1. The base frame is represented by purple arrows and the end effector frame is represented by red arrows. The rotation axes of flying watches are represented by arrows on cylinders. Green cylinders represent flying watches with rotation axes on vertical planes. Yellow cylinders represent flying watches with rotation axes on horizontal planes. The distance between two flying watches on the same link is 0.5 m. Since this distance is larger than the diameter of the propeller (0.381 m), the two flying watches on the same link do not collide with each other. The distance between a flying watch and the closest joint is 0.3 m. Under this distance, we can calculate the safe joint rotation range that prohibits the flying watches on both sides of a joint colliding is from -101.2 to 101.2 degrees. The arm is made of CFRP and has an inner diameter of 96 mm and thickness of 2 mm. The joint mass is 1 kg and link mass is 0.95 kg. The total arm mass is 16.4 kg. The simulation arm design is derived from an existing long-reach arm in our lab [7]. We assume that all joints of the simulation arm are identical. We set the maximum thrust of flying watch to 18 N based on our thrust test in Section 2.3.

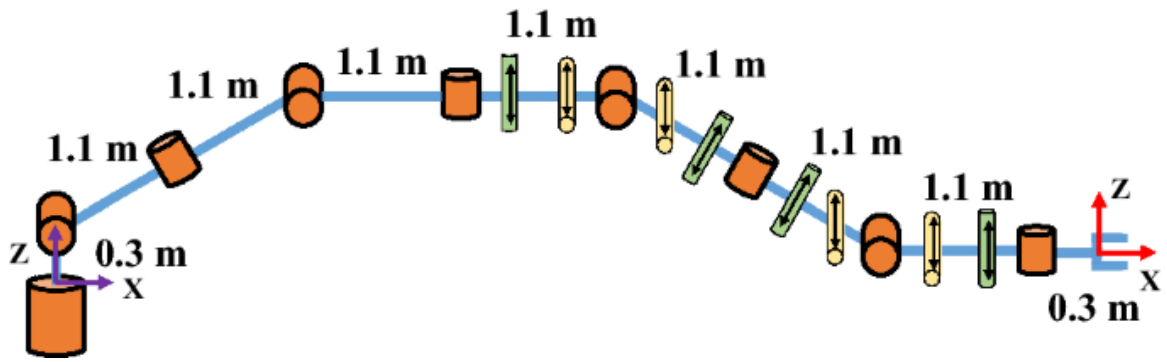

Fig. 4.1. The setup of the simulation robotic arm and flying watches.

Regarding the simulation process, in a simulation case, we positioned the end effector at a certain position and applied a certain force on the end effector. Then we compare the maximum joint loads with and without flying watch attached. More specifically about the end effector positions, since the first joint of the simulation arm rotates in yaw direction, for simplicity, the end effector is positioned on XOZ plane of the base frame. In different cases, the X coordinate of the end effector ranges from 2 m to 8 m with a step size of 1 m and the Z coordinate ranges from -7.7 m to 8.3 m with a step size of 2 m. Both coordinates referred to the base frame. The end effector frame always coincides with the base frame. More specifically about the force applied on the end effector, in different cases, the force ranges from 0 N to 125 N with a step size of 25 N and has directions along positive or negative direction of X, Y, or Z of the base frame. When flying watches are attached, since joint 6-8 have flying watches on both sides, we ensure that these joints range from -90 to 90 degrees. Since this range is narrower than the safe joint rotation range (from -101.2 to 101.2 degrees), the flying watches on both sides of a joint do not collide. For joint 1 (base joint), the range is from negative infinity to positive infinity since it is not related to flying watch collision. For other joints, the ranges are from -165 to 165 degrees so that adjacent links do not overlap. When no flying watch is attached, joint 6-8 range from -165 to 165 degrees. Other joint ranges do not change.

For a certain case, in order to compare the maximum normalized joint loads with and without flying watches attached, we define Relative Load Reduction (RLR), η, as follows. C_{NO_FW} is the maximum normalized joint load without flying watch attached. C_{FW} is the maximum normalized joint load under the WACAE. Both C_{NO_FW} and C_{FW} are summed over all cases concerned. η reflects how much flying watches have reduced the maximum normalized joint loads.

$$\eta = \frac{\Sigma C_{NO\_FW} - \Sigma C_{FW}}{\Sigma C_{NO\_FW}} \tag{4.1}$$

Some implementation details are as follows. Regarding the stopping criteria of the example WACAE solution, we use a very high maximum number of iterations (1000) and a very small minimum acceptable decrease of the cost function (10^{-7}) in order to approximate the real local minimal very precisely. When implementing the LIK and IK, the maximum end effector error is 10 mm. We found it is possible (probability=14.3%) that LIK did not reduce the end effector error under 10 mm in Step 1 of the example WACAE solution. We did not include these cases when computing the RLR of WACAE and computing the probability that WACAE is helpful, since no optimization really happened. When implementing AODS, for simplicity, we only compute $\text{LIK}(i, \boldsymbol{q}(i) + \epsilon, \boldsymbol{p}_d, \boldsymbol{q}_l(i^c), \boldsymbol{q}_u(i^c))$ in Step 1 instead of $(C(\boldsymbol{s}, \text{LIK}(i, \boldsymbol{q}(i) + \epsilon, \boldsymbol{p}_d, \boldsymbol{q}_l(i^c), \boldsymbol{q}_u(i^c))) - C(\boldsymbol{s}, \text{LIK}(i, \boldsymbol{q}(i), \boldsymbol{p}_d, \boldsymbol{q}_l(i^c), \boldsymbol{q}_u(i^c))))/\epsilon$. If $\text{LIK}(i, \boldsymbol{q}(i) + \epsilon, \boldsymbol{p}_d, \boldsymbol{q}_l(i^c), \boldsymbol{q}_u(i^c))$ exists, then the ith generalized coordinate can change without changing the end effector configuration. Therefore, we regard the i th generalized coordinate as optimizable. If no flying watch is attached or the attached flying watches are working under WACAE-I, IK is used to compute arm configurations. Since all joints of the simulation arm are identical, it is not necessary to normalize joint load.

Until now, the simulation setup and process are explained in detail, in the following, the simulation results will be presented and discussed.

Firstly, we visualize some cases in our simulations in Fig. 4.2-4.7. The base frame is shown in Fig. 4.2-4.7. The positive directions of the X, Y, and Z axis of the base frame are respectively shown using magenta, black, and green line segments with one end at the origin of the base frame. The absolute values of joint torques of these cases are shown in Table 4.1. The positions of end effector of Fig. 4.2-4.7 are all [4, 0, 2.3]. The base joints are represented by the red dots and other joints are represented by black dots. The cyan lines on the joints represent the torques of the joints. The end effectors are represented by black dots. The end effector reaction forces are represented by green lines on the end effector. The flying watch thrusts are represented by red lines. When WACAE-I is used, the arm is represented by magenta lines. When WACAE-II is used, the arm is represented by blue lines.

Table 4.1. JOINT TORQUES OF EXAMPLE CASES

End Effector Reaction Force (N)	Method	Torque 1 (Nm)	Torque 2 (Nm)	Torque 3 (Nm)	Torque 4 (Nm)	Torque 5 (Nm)	Torque 6 (Nm)	Torque 7 (Nm)	Torque 8 (Nm)	Torque 9 (Nm)
[125,0,0]	First	18.3	284.8	108.2	173.6	118.8	216.8	86.3	12.2	0.0
[125,0,0]	Second	1.7	234.1	241.7	241.7	77.9	197.4	1.5	12.1	0.0
[0,125,0]	First	357.2	98.0	603.0	32.4	307.0	39.3	194.0	12.0	37.5
[0,125,0]	Second	341.6	226.0	331.0	237.1	69.3	160.6	224.9	14.2	37.5
[0,0,-125]	First	18.3	515.0	122.9	324.2	144.0	426.7	24.4	181.7	0.0
[0,0,-125]	Second	33.3	387.6	404.0	404.1	116.7	333.3	10.8	187.4	0.0

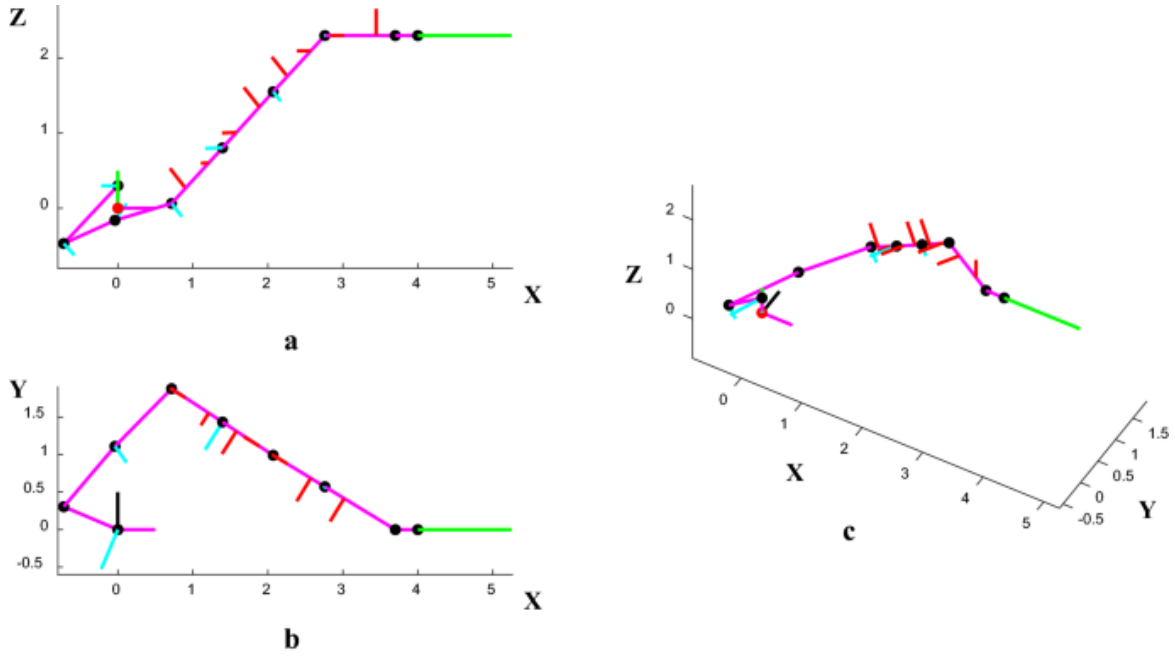

Fig. 4.2. The simulation arm and flying watch thrusts under WACAE-I when the end effector reaction force is [125,0,0] N (RLR = 24.1%). a Front view. b Top view. c 3-D view

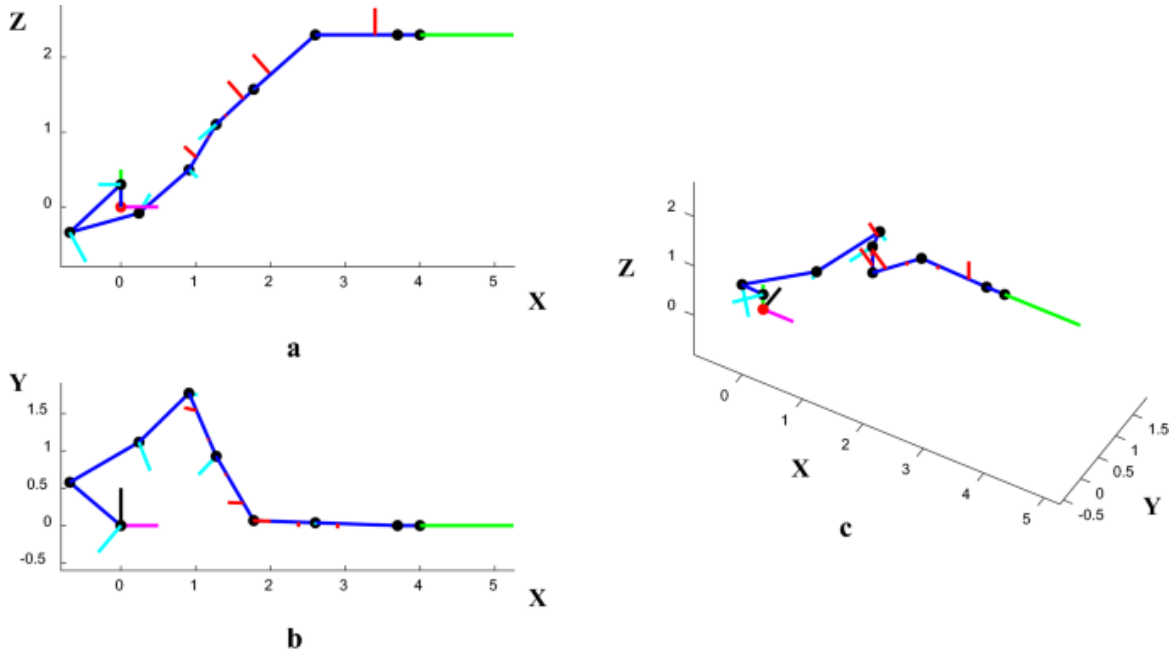

Fig. 4.3. The simulation arm and flying watch thrusts under WACAE-II when the end effector reaction force is [125,0,0] N (RLR = 35.6%). a Front view. b Top view. c 3-D view

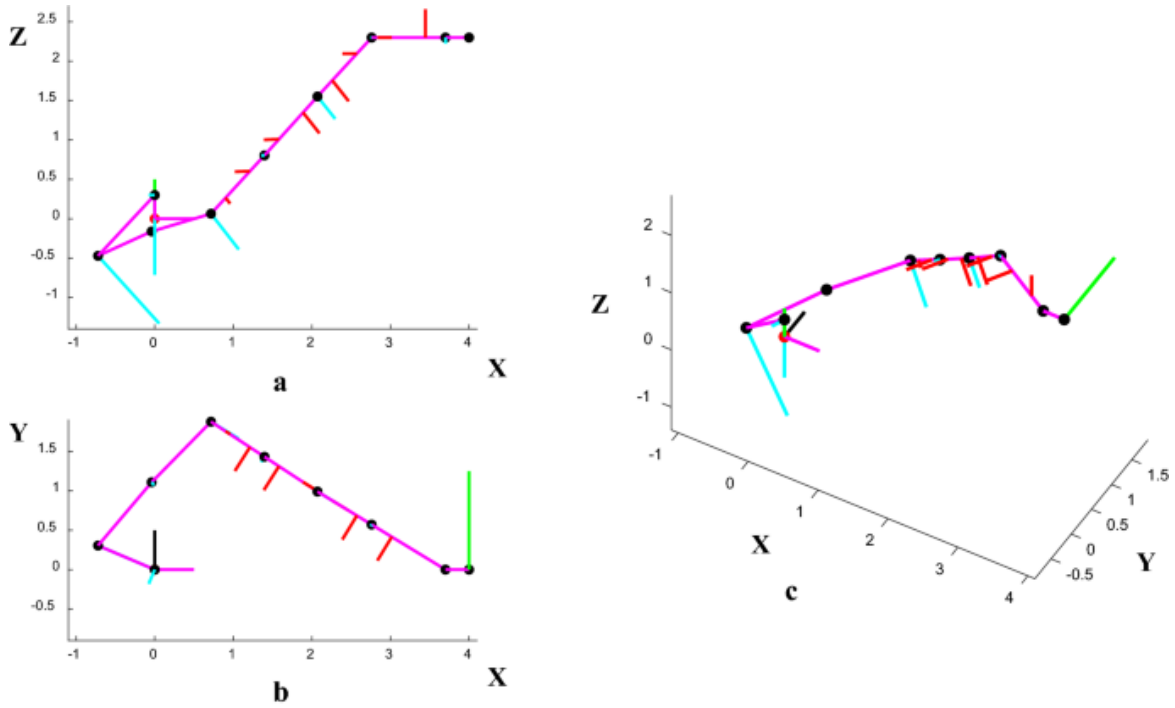

Fig. 4.4. The simulation arm and flying watch thrusts under WACAE-I when the end effector reaction force is [0,125,0] N (RLR= − 20.6%). a Front view. b Top view. c 3-D view

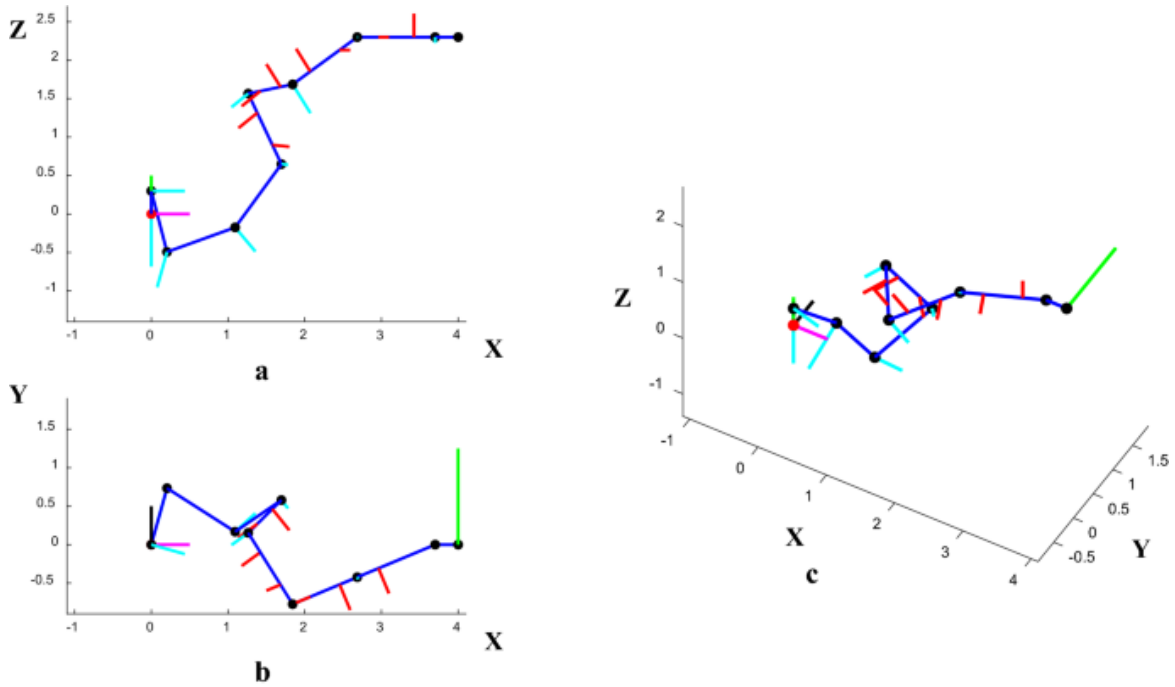

Fig. 4.5. The simulation arm and flying watch thrusts under WACAE-II when the end effector reaction force is [0,125,0] N (RLR = 31.7%). a Front view. b Top view. c 3-D view

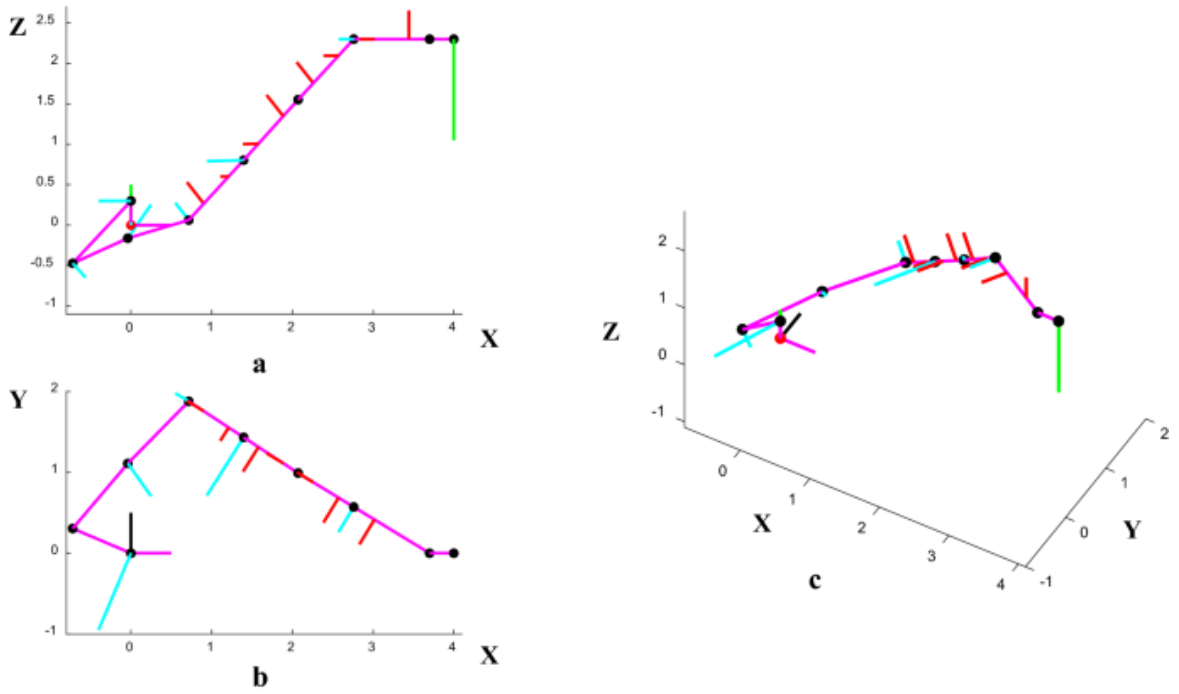

Fig. 4.6. The simulation arm and flying watch thrusts under WACAE-I when the end effector reaction force is [0,0,− 125] N (RLR = − 1.0%). a Front view. b Top view. c 3-D view

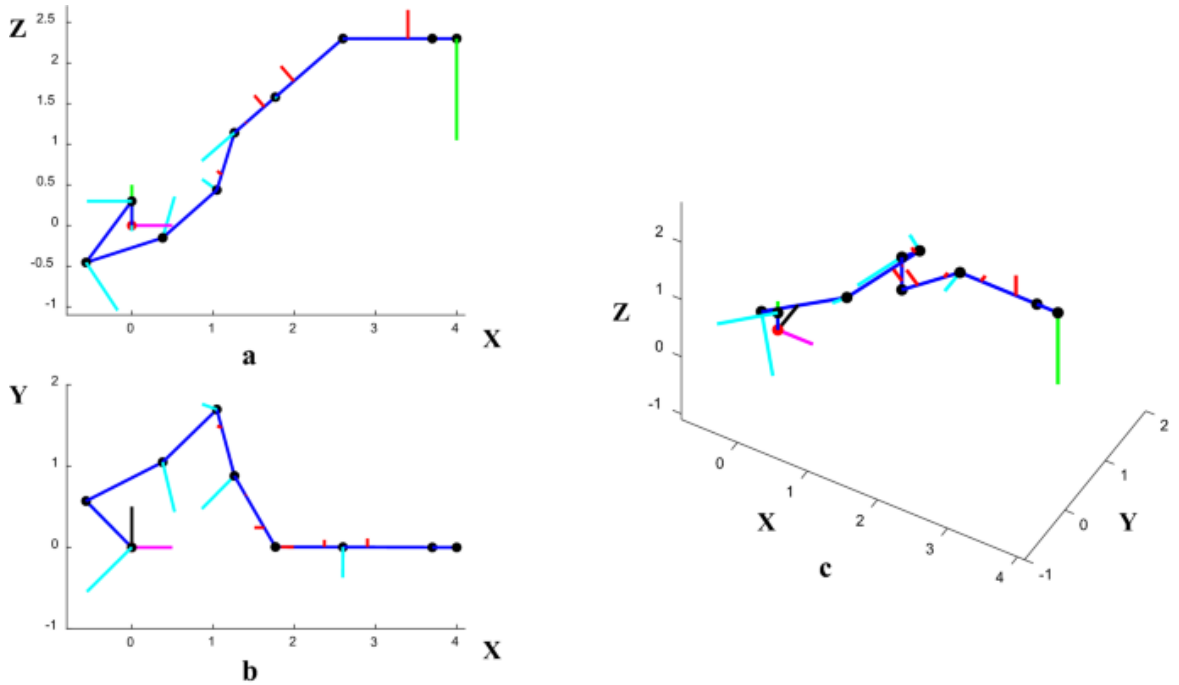

Fig. 4.7. The simulation arm and flying watch thrusts under WACAE-II when the end effector reaction force is [0,0,− 125] N (RLR = 20.8%). a Front view. b Top view. c 3-D view

We can see by comparing Fig. 4.2 and Fig. 4.3 that the WACAE-II can achieve a higher RLR with relatively small watch thrusts. By comparing Fig. 4.4 and Fig. 4.5, when the WACAE-II is applied, we can observe that more horizontal thrusts are positioned closer to the end effector to obtain larger moment arms to counteract the horizontal end effector reaction force. From Fig. 4.4 and Table 4.1, we can also notice that the WACAE-I achieves a negative RLR in Fig. 4.4, which means the situation of operating watches performs worse than the situation in which no watch is attached. This is because when flying watches are attached, joint 6-8 have narrower rotation ranges to avoid flying watch collisions and the arm configuration with less actuator loads may not be available due to the narrower joint rotation ranges. However, we found in most cases operating flying watches helps to reduce the maximum actuator load. The probability that the WACAE-I helps to reduce the maximum joint load is 95.41% and the probability that the WACAE-II helps to reduce the maximum joint load is 98.99%. By comparing Fig. 4.6 and Fig. 4.7, we can also see when WACAE-II is applied, higher RLR can be achieved with smaller thrusts.

Secondly, the overall simulation results are in Table 4.2. From Table 4.2, we can see both levels of WACAE can significantly reduce the maximum joint load by more than 36%. The WACAE-II is statistically more effective than WACAE-1. However, for a single case, we found sometimes WACAE-II may result in lower RLR than WACAE-I. The probability that WACAE-II performs better than WACAE-I is 73.9%. We believe such phenomenon happens because the example WACAE solution only find local minimal instead of global minimum.

Table 4.2. OVERALL PERFORMANCE OF FLYING WATCHES

Method	RLR
First Level Watch-Actuator Cooperation	36.9%
Second Level Watch-Actuator Cooperation	43.7%
Configuration Optimization Only (No Flying Watch Attached)	8.7%

In order to further understand the composition of the RLR of WACAE-II, we removed the mass of flying watches on arm links and skipped step 2 in the example WACAE solution, which means the example solution will only optimize arm configuration. The result is also shown in Table 4.2. We found only arm configuration optimization will result in a much lower RLR (8.7%) than the WACAE-II (43.7%). Therefore, we can understand both optimal flying watch thrusts and optimal watch positions and orientations play a role in enhancing the arm strength.

Thirdly, we tested the computation speed of the WACAE example solution. The computer we used has Intel i7 CPU (Frequency=2.00 GHz) and 8 GB RAM. For simplicity, we changed the step size of end effector positions in X direction from 1 to 2 m. In each axis, the end effector reaction force of -100 N, -50 N, 0 N, 50 N, and 100 N are sampled for testing computation speed. The speed results are shown in Table 4.3.

Table 4.3. SPEED OF EXAMPLE WACAE SOLUTION

Method	Median (s)	Mean (s)	Standard Deviation (s)
First Level Watch-Actuator Cooperation	27.7	42.9	40.8
Second Level Watch-Actuator Cooperation	102.0	457.5	645.9

From Table 4.3, we can see the example WACAE solution is only suitable for offline thrust planning. However, since we used a very high maximum iteration number and very small minimum acceptable decrease of the cost function for the example WACAE solution in order to approximate the real minimal very precisely, the computation speed can be increased by reducing the maximum iteration number and increasing the minimum acceptable decrease of the cost function. From Table 4.3, we can also observe significant variation of computation time. We believe this is because the number of flying watches (8 flying watches) and the arm degree of freedom (9 DOF) are high. Even though the example solution optimizes thrusts and

arm configuration iteratively, in each step (step 2 or step 3 in Algorithm 4.2), the search spaces still have diverse and complicated high-dimension geometries.

4.3. Summary

In this Chapter, we introduced a model-base offline thrust planner called Watch-Actuator Cooperation for Arm Enhancement (WACAE). WACAE requires a dynamic model of a robotic arm (Equation of Motion) as well as prior knowledge of a mission (arm trajectory and end effector reaction forces during mission) to plan appropriate flying watch thrusts before the mission. WACAE includes two level watch-actuator cooperation. In WACAE-I, flying watches adapt thrusts to cooperate with actuators. WACAE-I is suitable when the user wants more control on arm configurations. In WACAE-II, not only do flying watches adapt their thrust, actuator angles will also be adjusted to provide flying watches better positions and orientations to counteract external forces. WACAE-II can generally reduce joint load more significantly than WACAE-I. Simulations show both WACAE-I and WACAE-II are effective for enhancing a long robotic arm.

We may notice that friction is not included in the EoM (2.23) that WACAE used for computing joint loads. This is because lubrication friction in arm transmission is highly dependent on environmental properties such as temperature and accurately predicting friction is difficult. Therefore, the joint loads flying watches reduce include both actuator load and friction. When the arm is static, the friction effects help preventing arm moving and when the arm is moving the friction effects increase actuator loads. In both situations, reducing joint load helps reducing actuator load.

WACAE is a suitable thrust planner when we know exactly the arm dynamics and what will happen during a mission. Also, WACAE can calculate watch thrusts and joint loads before

a mission. Therefore, it allows us to rehearse a mission and make necessary adjustments in advance.

Finally, regarding generality and objectivity of WACAE simulation results, since the simulation arm design is derived from an existing long robotic arm (as described in the second paragraph of subsection 4.2) and varieties of external force and end effector positions are tested, it is safe to say that the simulation results of WACAE have enough generality and objectivity. However, to obtain higher generality and objectivity, simulations or physical experiments based on some existing arms can be done in the future.

5. Model-free Flying Watch Thrust Planning

In the previous Chapter, a model-based offline flying watch thrust planner called WACAE is introduced. WACAE requires dynamics model of a robotic arm and prior knowledge of a mission to work. However, it happens very often in practice that we do not have the tools or time to precisely attach flying watches and construct an arm model and we are not sure what kinds of arm trajectories or external forces will happen in a mission. In those uncertain situations, how to plan flying watch thrusts?

This Chapter answers that question by proposing and demonstrating a model-free online thrust planner, called Physical-gradient-based Optimization of Thrust (POT). POT has the following features. (1) Loose prerequisites and high robustness. POT has the ability to plan flying watch thrusts without arm model and prior knowledge of a mission. It only requires actuator load and arm configuration feedback from an arm. No matter what flying watch attachment allocation is applied and what kind of arm trajectory or external forces happen during a mission, POT will always function to enhance a robotic arm. (2) High portability. No modification is necessary for the original arm control software. Therefore, POT can be easily plugged in or unplugged from the original arm control software.

Although POT requires very loose prerequisites to work, we should still be very careful about the flying watch attachment allocation and possible external forces during a mission. As we discussed in Chapter 3, a flying watch attachment allocation customized for a specific mission can significantly improve the flying watch performance. And if an external force is too strong or changes too fast, POT may fail to counteract the external force. Therefore, customizing flying watch attachment allocation using AOWS and rehearsing a mission using WACAE in advance based on known information are highly recommended, even though we decide to use POT.

5.1. Physical-gradient Optimization of Thrust (POT)

This Section will explain POT in a top-down manner so that the reader will always have a big picture in mind and not lost in details. Initially, the whole workflow of POT will be shown and the basic function of each step will be explained. Then we will explain the details of each step.

The integration of POT and arm controller is shown in Fig. 5.1. POT needs actuator loads and arm configuration information from the actuators. For electric motors, the actuator loads can be calculated from motor currents measured by sensors and arm configuration can be measured by hall sensors or potentiometers. Those current and position information are easily accessible for many commercial motors. From the actuator loads and arm configuration, POT will calculate appropriate flying watch thrusts and automatically command flying watch to implement the thrusts. The flying watch thrusts will further influence actuator loads, which will be further measured by arm sensors. During a mission, all flying watches are operated automatically by POT and the user only needs to focus on arm operation.

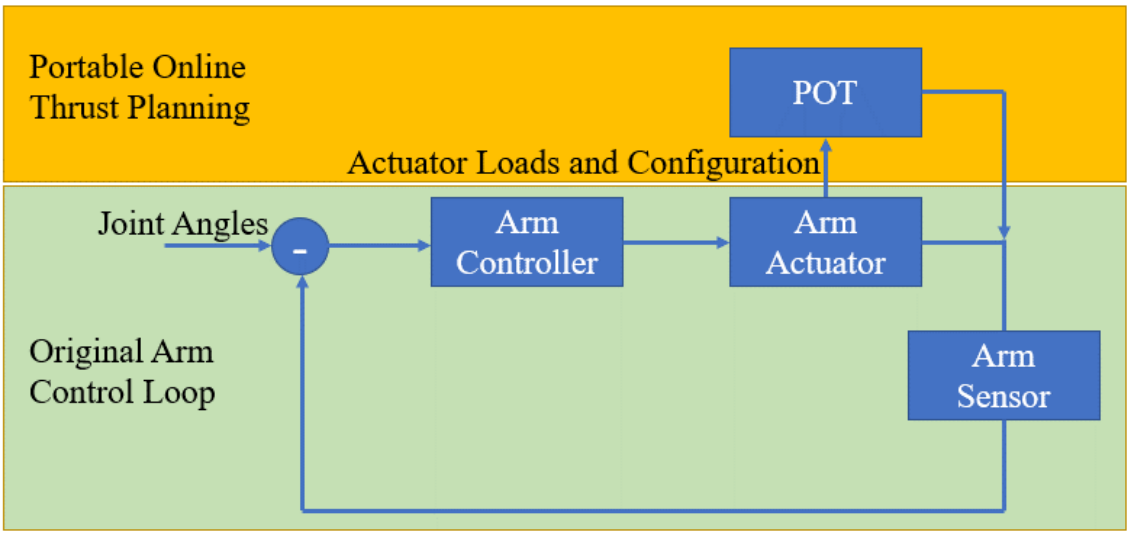

Fig. 5.1. The system integration of POT and original arm controller.

The working principle of POT can be intuitively interpreted in the following way. Firstly one flying watch slightly change its thrust in one direction. Then if the maximum joint load is slightly reduced, then we know the current thrust changing direction is the arm load reduction direction. If the maximum joint load increases, the watch thrust should change in the opposite direction. By deliberately generate slight vibration, the correct direction for reducing arm load can be measured. In a similar way, we can imagine the correct magnitude of thrust change for arm load reduction can also be measured by deliberate flying watch vibration. POT is an algorithm of measuring appropriate thrust changes for arm load reduction through very slight deliberate flying watch vibrations and applying such changes for arm enhancement. POT is essentially a gradient descent method used for reducing actuator loads. More specifically, POT is solving the following problem.

Problem 5.1: Physical-gradient-based Optimization of Thrust (POT):

$$\min_{\boldsymbol{s}} \Lambda(\boldsymbol{q}, \boldsymbol{s}) \text{ s.t. } \boldsymbol{s}_l < \boldsymbol{s} < \boldsymbol{s}_u$$

In Problem 5.1, Λ is the cost function of POT defined as follows.

$$\Lambda(\boldsymbol{q}, \boldsymbol{s}) = \|\tilde{\boldsymbol{\tau}}_a(\boldsymbol{q}, \boldsymbol{s})\|_\infty \tag{5.1}$$

$\boldsymbol{q}$ is the generalized coordinates defining the arm configuration. $\boldsymbol{s}$ is the flying watch thrust vector. $\boldsymbol{s}_l$ and $\boldsymbol{s}_u$ are respective the lower and upper bounds of flying watch thrusts. In (5.1), $\tilde{\boldsymbol{\tau}}_a = \boldsymbol{H}_a \boldsymbol{\tau}_a$, where $\boldsymbol{H}_a = diag(1/\tau_{ap1}, \dots, 1/\tau_{apK})$ is the normalization matrix and $\tau_{ap1}, \dots, \tau_{apk}$ are the maximum permitted actuator loads of the K joints. $\boldsymbol{\tau}_a$ is a vector containing all actuator loads. We can notice by comparing Problem (5.1) and Problem (4.1) that POT and WACAE-I are solving very similar problem. The major difference is that POT is reducing actuator loads while WACAE-I is reducing joint loads.

There are two major differences between POT and typical gradient descent. (1) In POT, the cost function is experimentally measured and the gradient and step size are also experimentally determined by deliberately oscillating flying watch thrusts and measuring how the cost function

changes. Those flying watch thrust oscillations are designed to influence the arm operation as slightly as possible. However, in typical gradient descent, the cost function, gradient, and step size are computationally determined by mathematical models. This is the fundamental reason that POT is a model-free method. To the best of our knowledge, there is no previous research that considered optimizing thrusts through deliberately-generated thrust oscillations. (2) Typical gradient descent intends to obtain the minimal value of the cost function. However, POT only intends to reduce the cost function below a threshold τ_{permit}. The purpose of that is to reduce the number of thrust oscillation experiments on the arm.

The workflow of POT is shown in Fig. 5.2. POT has two phases: passive thrust adjustment phase and active thrust adjustment phase. POT starts from the passive thrust adjustment phase, in which the flying watch thrust is predicted based on current arm configuration and memory of previous thrusts and corresponding arm configurations. If the predicted thrusts fail to reduce the maximum joint load below τ_{permit}, POT will proceed to active thrust adjustment phase, in which POT determines appropriate flying watch thrusts based on deliberately generated thrust

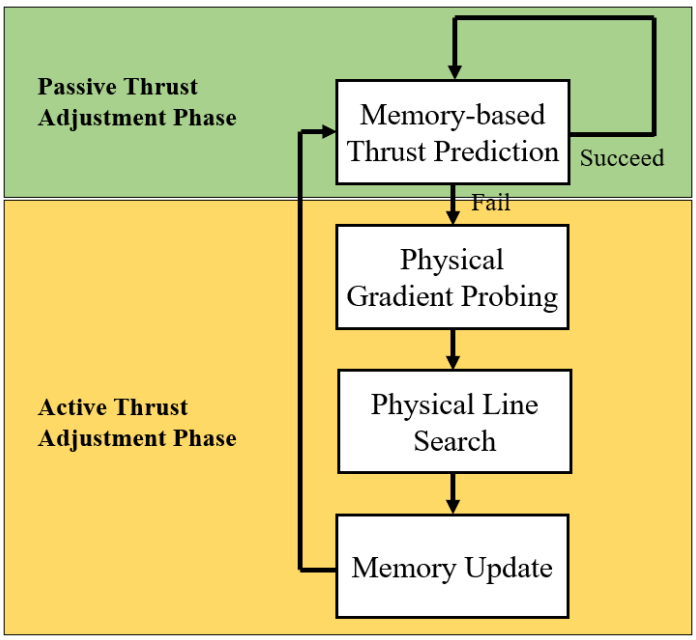

Fig. 5.2. The workflow of POT.

oscillations and corresponding actuator load oscillations. More specifically, the active thrust adjustment phase includes a physical gradient probing step in which the appropriate thrust directions are determined and a physical line search step in which the appropriate thrust magnitudes are determined.

In the following subsections, we will explain each component of POT in detail and finally explain how those components are assembled together.

5.1.1. Memory-based Thrust Prediction

In the active thrust adjustment phase, the deliberately generated thrust changes may result in slight arm vibration. To eliminate unnecessary arm vibration, the memory-based thrust prediction step that estimates appropriate thrusts purely from previous arm configurations and flying watch thrusts is executed before the active thrust adjustment phase. I used the following inverse distance weighting [55] for thrust prediction.

Given the memory of previous N_{idw} tuples of arm configuration and flying watch thrusts $(\boldsymbol{q}_1, \boldsymbol{s}_1), \dots, (\boldsymbol{q}_{N_{idw}}, \boldsymbol{s}_{N_{idw}})$ and the current arm configuration $\boldsymbol{q}_{cur}$, the predicted thrust $\boldsymbol{s}_{pred}$ is as follows.

$$\boldsymbol{s}_{pred} = \begin{matrix} \frac{\sum_{i=1}^{N_{idw}} \|\boldsymbol{q}_{cur} - \boldsymbol{q}_i\|_2^{-\gamma} \boldsymbol{s}_i}{\sum_{i=1}^{N_{idw}} \|\boldsymbol{q}_{cur} - \boldsymbol{q}_i\|_2^{-\gamma}}, if \min_i \|\boldsymbol{q}_{cur} - \boldsymbol{q}_i\|_2 \geq \delta_{idw} \\ \boldsymbol{s}_i, if \ \|\boldsymbol{q}_{cur} - \boldsymbol{q}_i\|_2 < \delta_{idw} \end{matrix} \tag{5.2}$$

Equation (5.2) is a weighted average of all thrusts in the memory. The weights are the power of inverse Euclidean distance of the current arm configuration and the arm configurations in the memory. γ decides how distances influence weights. In this dissertation,

$\gamma = 3$. (5.2) is essentially interpolating the thrust of the current arm configuration based on previous arm configurations and flying watch thrusts.

It is possible that the current arm configuration is too far from the memorized arm configurations. As a result, the predicted thrusts are not meaningful and differs significantly from the current implemented thrusts. Therefore, if the difference of predicted thrusts and the current thrusts is larger than a threshold, the predicted thrust is set to the current thrusts. Also, the previous thrusts and arm configuration that are too old are not helpful. Therefore, a first-in-first-out queue with length of N_{idw} is used as the memory for storing previous watch thrusts and arm configuration. In other words, only the most recent N_{idw} watch thrusts and arm configuration pairs are saved for thrust prediction.

5.1.2. Physical Gradient Probing

The i th components of a physical gradient is defined as follows.

$$\nabla_{s_i}\widehat{\Lambda} = \frac{\widehat{\Lambda}(\boldsymbol{q}, \boldsymbol{s} + \delta_T \boldsymbol{e}_i) - \widehat{\Lambda}(\boldsymbol{q}, \boldsymbol{s})}{\delta_T} \tag{5.3}$$

In (5.3), $\widehat{\Lambda}$ is a measurement of the cost function Λ. δ_T is a very small change of thrusts. $\boldsymbol{e}_i$ is a unit vector whose i th component is 1 and all other components are zero. (5.3) is essentially the definition of the gradient of the cost function Λ regarding watch thrusts. The only difference from typical gradient calculation process is that the cost function is directly measure instead of calculated from a mathematical model. We can see from (5.3) that in order to obtain one dimension of the physical gradient, the thrust of the i th flying watch needs to change slightly in order to cause a slight change in the cost function. After measuring the cost function change, the thrust of the i th flying watch will be set to its original value. Therefore, evaluating one dimension of physical gradient requires one small oscillation of the maximum actuator load.

We call this physical gradient determination process as physical gradient probing. The pseudocode of physical gradient probing is shown in Algorithm 5.1.

Algorithm 5.1: $\boldsymbol{g}_p$=PHYSICAL_GRADIENT_PROBING ($\boldsymbol{s}$, fw_ind, grad_prev)

STEP 1 (Initialization):

Initiate cur_cost=GET_COST(); δ_T; $\beta_T > 1$; $\boldsymbol{g}_p$ =ZERO_VECTOR(NUM_FW()); δ_T^{max};

STEP 2 (Physical Gradient Probing):

FOR i_ind in fw_ind

WHILE($\boldsymbol{g}_p$(i_ind)== 0 && $\delta_T \leq \delta_T^{max}$)

GEN_THRUST($\boldsymbol{s} + \boldsymbol{e}_i * \delta_T$);

$\boldsymbol{g}_p$(i_ind)=(GET_COST()-cur_cost)/δ_T;

GEN_THRUST($\boldsymbol{s}$);

$\delta_T = \beta_T \delta_T$

END_WHILE

END_FOR

STEP 3 (Result Confirmation):

IF $\|\boldsymbol{g}_p\|_\infty == 0$

$\boldsymbol{g}_p$=grad_prev; // use previous working gradient if physical gradient probing fails

END_IF

RETURN($\boldsymbol{g}_p$)

As shown in Algorithm 5.1, the input of PHYSICAL_GRADIENT_PROBING is $\boldsymbol{s}$ which is the current flying watch thrusts, fw_ind, which is a vector of indexes of flying watches whose thrusts we hope to optimize, and grad_prev, which is the previous effective physical gradient. The output of PHYSICAL_GRADIENT_PROBING is a partially evaluated physical gradient $\boldsymbol{g}_p$, at least one dimension of which is the same as $\nabla_{\boldsymbol{s}}\widehat{\Lambda}$ and other dimensions are zero. We only evaluate a subset dimensions of physical gradient indicated by fw_ind in order to increase response speed and decrease influence on arm operation. It can be proved that $\boldsymbol{g}_p$ is still a decreasing direction of the cost function if the step size $t > 0$ is small enough so that the cost function can be linearly approximated. Since the cost function can be linearly approximated, the cost function after updating is $\Lambda(\boldsymbol{q}, \boldsymbol{s} - t\boldsymbol{g}_p) \approx \Lambda(\boldsymbol{q}, \boldsymbol{s}) + \nabla_{\boldsymbol{s}}\widehat{\Lambda}^{\mathrm{T}}(\boldsymbol{s} - t\boldsymbol{g}_p - \boldsymbol{s}) = \Lambda(\boldsymbol{q}, \boldsymbol{s}) -$

$t\nabla_{\boldsymbol{s}}\widehat{\Lambda}^T\boldsymbol{g}_p$. Since $t\nabla_{\boldsymbol{s}}\widehat{\Lambda}^T\boldsymbol{g}_p \geq 0$, $\Lambda(\boldsymbol{q}, \boldsymbol{s} - t\boldsymbol{g}_p) \leq \Lambda(\boldsymbol{q}, \boldsymbol{s})$. fw_ind can be selected randomly or based on selection history. For example, the recent fw_ind that help reducing actuator load may still be effective. δ_T^{max} is the maximum permitted thrust oscillation magnitude that will not influence arm operation.

In Step 1, several key parameters are initialized. GET_COST() is a function to measure the current maximum normalize actuator load $\widehat{\Lambda}$. cur_cost is the current measurement of the cost function.

Regarding the initial value of δ_T, In the case of the prototype in Fig. 2.11, the propeller rotation speed is controlled by duty ratio of PWM signal sent to the motor driver. The duty ratio of 127/255 corresponds to zero rotation and the duty ratio of 227/255 corresponds to maximum speed. The initial value of δ_T is set as 10/255. β_T is the incremental factor of δ_T. ZERO_VECTOR() is a function that returns a zero vector with the length of input scalar. NUM_FW() is a function that returns the number of flying watches attached.

In Step 2, physical gradient is tested according to its definition. For each selected dimension of the physical gradient, the thrust of the corresponding flying watch is slightly increased by δ_T. GEN_THRUST() is a function to implement the input thrusts. If a commended flying watch thrust is larger than the maximum feasible thrust, GEN_THRUST will generate the maximum feasible thrust. Then the cost function is measured and the physical gradient is calculated. After that, the original thrust $\boldsymbol{s}$ is implemented. If the current dimension of physical gradient is zero, then the thrust oscillation is not large enough to cause cost function change. Therefore, δ_T is multiplied by an incremental factor $\beta_T > 1$. In practice, $\beta_T = 1.1$. The thrust oscillation loop of each physical gradient dimension terminates when this dimension of physical gradient is successfully obtained or when the δ_T is larger than permitted maximum oscillation magnitude.

In Step 3, we check whether the physical gradient is obtained successfully. If $\|\boldsymbol{g}_p\|_\infty$ is zero, then all physical gradient probing attempt failed. The previous physical gradient that can reduce the cost function is assigned to $\boldsymbol{g}_p$.

5.1.3. Physical Line Search

The physical line search is essentially a backtracking line search [47] on the physical gradient direction. The major difference from typical backtracking line search is (1) the cost function is still physically measured instead of calculated from mathematical models. (2) The step size will gradually increase so that smallest step sizes are tested first, while in typical backtracking line search, the largest step size is tested first. The pseudocode of physical line

Algorithm 5.2: t_{pls}=PHYSICAL_LINE_SEARCH ($\boldsymbol{s}$, $\boldsymbol{g}_p$)

STEP 1 (Initialization):

Initialize cur_cost =GET_COST(); α_{pls}; $\beta_L > 1$; small_enough_flag=0; t_{pls}; max_count; t_{pls}^{max};

STEP 2 (Physical Line Search):

counter=1;

WHILE(small_enough_flag==0)

IF (counter>max_count || $t_{pls} > t_{pls}^{max}$)

$t_{pls} = 0$;

BREAK;

END_IF

GEN_THRUST($\boldsymbol{s} - t_{pls}\boldsymbol{g}_p$);

small_enough_flag=(GET_COST()<=cur_cost -$\alpha_{pls}t_{pls}\|\boldsymbol{g}_p\|_2$);

GEN_THRUST($\boldsymbol{s}$);

$t_{pls} = \beta_L t_{pls}$;

counter=counter+1;

END_WHILE

RETURN(t_{pls})

search is shown in Algorithm 5.2. The input of PHYSICAL_LINE_SEARCH is the current flying watch thrusts $\boldsymbol{s}$ and a search direction $\boldsymbol{g}_p$. The output is an appropriate step size.

In Step 1, several important parameters are initialized. $\alpha_{pls} \in (0, 0.5)$ is a parameter used for determining whether the cost function is sufficiently reduced. β_L is the incremental factor for updating step size t_{pls}. t_{pls}^{max} is the maximum step size. cur_cost is the current measurement of the cost function. small_enough_flag is used for marking whether the cost function has been reduced small enough in the line search. max_count is the maximum iteration number of the line search.

In Step 2, the thrust corresponding to the initial step size is firstly generated and then we measure the cost function to see whether it is sufficiently reduced. After that the original thrust is implemented again. If the cost function is not sufficiently reduced, a larger step size $\beta_L t$ is further tested. This process repeats until the cost function is sufficiently reduced or the loop time exceed the maximum permitted loop time (max_count) or the step size exceed the maximum step size (t_{max}). If the loop ends due to the later two reasons, the physical line search fails and zero step size is returned. Otherwise, the physical line search succeeds and the result step size is returned.

5.1.4. Physical-gradient-based Optimization of Thrust

After we introduced all components of POT, let us assemble them. The pseudocode of POT is shown in Algorithm 5.3. In Step 1, several key parameters are initialized. τ_{permit} is the maximum permitted actuator load. $\boldsymbol{s}$ is the flying watch thrusts. **Memory** is a matrix recording all previous effective arm configuration and flying watch thrusts. active_adjust is a flag that is 1 when POT is in active thrust adjustment phase and 0 when POT is in passive thrust adjustment

phase. The initial value of active_adjust is 0. grad_prev is the effective physical gradient in the previous active thrust adjustment loop. $\boldsymbol{s}_l$ and $\boldsymbol{s}_u$ are respectively the lower and upper bounds of flying watch thrusts.

In Step 2, if POT is not in active thrust adjustment phase, a temporary flying watch thrust vector is generated using the MEMORY_BASED_THRUST_PREDICT() function, which is an implementation of inverse distance weighting algorithm we discussed in subsection 5.1.1. If the predicted thrusts can reduce the cost function below τ_{permit}, then POT go back to Step 2. Otherwise, active_adjust is set to 1 and POT goes into active thrust adjustment phase.

In Step 3, we firstly select a subset of flying watch to adjust. As we discussed in subsection 5.1.2, the purpose of that is to reduce response time and influence on arm operation. The current latest POT implementation just randomly chooses a given number of flying watch and each flying watch has the same probability to be chosen. Then a search direction $\boldsymbol{g}_p$is returned by PHYSICAL_GRADIENT_PROBING. In Step 4, PHYSICAL_LINE_SEARCH returns an appropriate step size along $\boldsymbol{g}_p$. In Step 5, if some dimensions of the updated thrust exceed the feasible boundary, the updates on those dimensions are canceled. Such selective update will still reduce the cost function if the step size is small enough as we proved in subsection 5.1.2. This processed is called thrust pruning. Then we firstly check whether the pruned thrusts can really reduce the cost function. if not, then the pruning fails and the original thrust is implemented again. If the cost function is reduced, we further check whether the cost function is below τ_{permit}. If not, a new round of active thrust adjustment phase will be executed. If yes, POT will go to passive thrust adjustment phase.

Algorithm 5.3: PHYSICAL_GRADIENT_BASED_OPTIMIZATION_OF_THRUST()

STEP 1 (Initialization):

Initiate τ_{permit}, $\boldsymbol{s}$, **memory**=[], active_adjust=0; grad_prev=ZERO_VECTOR(NUM_FW()); $\boldsymbol{s}_l$;$\boldsymbol{s}_u$;

STEP 2 (Memory-based Thrust Prediction):

IF active_adjust==0

$\boldsymbol{q}$ =GET_ARM_CONFIG(); // GET_ARM_CONFIG() returns the current arm configuration.

$\boldsymbol{s}_{temp}$ =MEMORY_BASED_THRUST_PRIDICT($\boldsymbol{q}$, **memory**);

IF ISEMPTY($\boldsymbol{s}_{temp}$)==0

GEN_THRUST($\boldsymbol{s}_{temp}$);

IF GET_COST()≤ τ_{permit}

$\boldsymbol{s} = \boldsymbol{s}_{temp}$;

GOTO STEP 2;

END_IF

END_IF

END_IF

active_adjust=1;

STEP 3 (Physical Gradient Probing):

fw_ind=SELECT_FW();

$\boldsymbol{g}_p$=PHYSICAL_GRADIENT_PROBING ($\boldsymbol{s}$, fw_ind, grad_prev)

STEP 4 (Physical Line Search):

t_{pot}=PHYSICAL_LINE_SEARCH ($\boldsymbol{s}$, $\boldsymbol{g}_p$)

STEP 5 (Thrust Pruning & Update Memory):

$\boldsymbol{s}_{pruning}$=$\boldsymbol{s} - t_{pot}\boldsymbol{g}_p$;

FOR i_ind=1:NUM_FW()

IF $\boldsymbol{s}_{pruning}$(i_ind)≤ $\boldsymbol{s}_l$ (i_ind) && $\boldsymbol{s}_{pruning}$(i_ind)≥ $\boldsymbol{s}_u$(i_ind)

$\boldsymbol{s}_{pruning}$(i_ind)= $\boldsymbol{s}$(i_ind);

END_IF

END_FOR

cur_cost=GET_COST();

GEN_THRUST($\boldsymbol{s}_{pruning}$)

IF GET_COST()<cur_cost

$\boldsymbol{s}$=$\boldsymbol{s}_{pruning}$;

grad_prev=$\boldsymbol{g}_p$;

IF GET_COST()<τ_{permit}

$\boldsymbol{q}$ =GET_ARM_CONFIG();

UPDATE_MEMORY($\boldsymbol{s}$, $\boldsymbol{q}$);

active_adjust=0;

END_IF

ELSE

GEN_THRUST($\boldsymbol{s}$)

END_IF

GOTO STEP 2;

5.2. Demonstration

In this Section, we demonstrate POT on Planar Inspection Arm (PIA). PIA is shown in Fig. 5.3. The system design of PIA is shown in Fig. 5.4. PIA is a planar arm originally designed only for inspecting a horizontal plane using end effector sensors and the arm motors cannot actuate the arm when the workspace is a tilted plane. To solve this problem, we attached two flying watches at the middle point of link 2 and link 3 so that the workspace of PIA can be extended to tilted plane. Each joint of PIA has a MAXON 267121 motors with a maximum continuous torque of 25.5 mNm and a harmonic drive with gear ratio of 100. The maximum actuator load is $2.55Nm$. The arm length is $l_{arm} = 1.77m$ and the arm mass is 3.46 kg. The detailed specification of PIA is shown in Table 5.1.

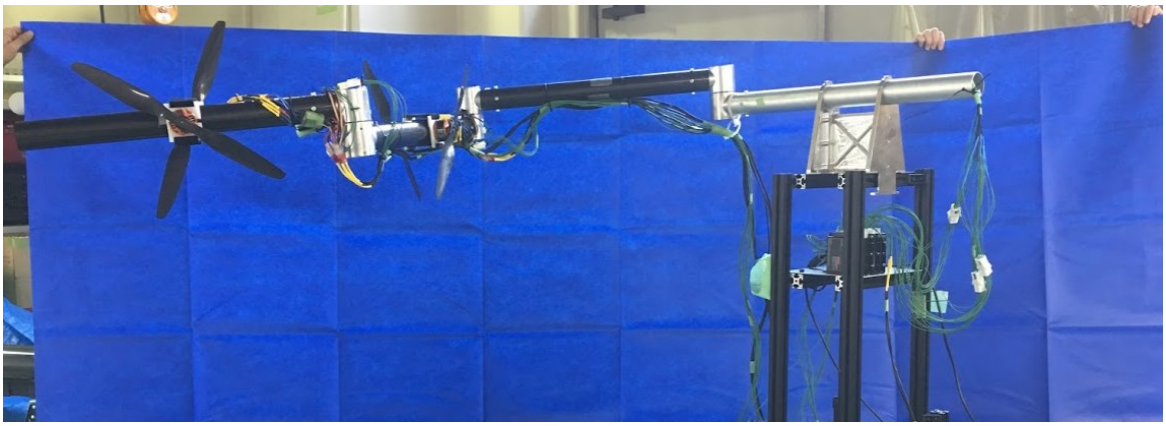

Fig. 5.3. Planar Inspection Arm attached with two flying watches.

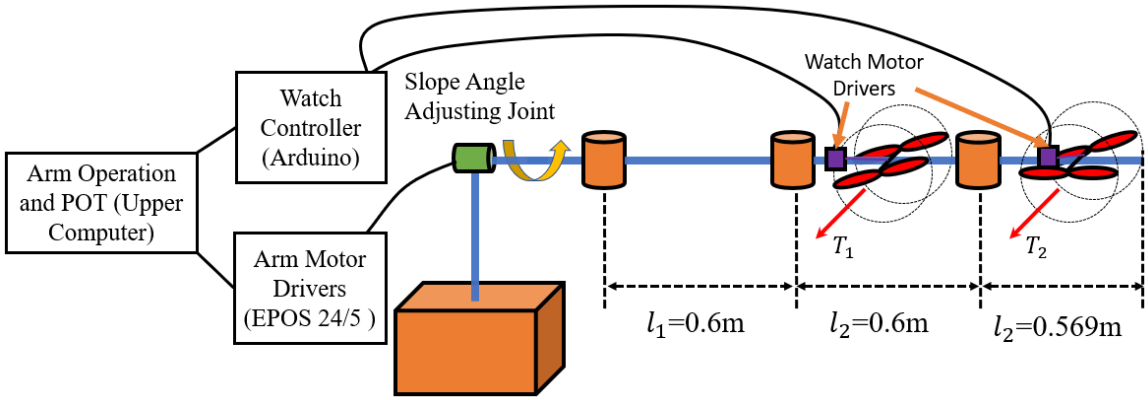

Fig. 5.4. System design of PIA enhanced by flying watches.

When the slope angle is 30 °, we already confirmed that the flying watch prototype in Fig. 2.11 is appropriate for PIA based on Actuator Enhancement Factor, Reaction Counteraction Factor, and Workspace Factor. The flying watch prototype can generate a maximum thrust of 19.4 N. We can calculate that the thrusts of the two flying watches are enough for canceling the gravity torque on the 2nd and 3rd joints. In such situation, the base joint only needs to afford the torque due to the gravity of the first link, which is 0.30 Nm. Such torque is smaller than the maximum actuator load. Therefore, the two flying watch prototypes are theoretically sufficient to enhance PIA on a plane with slope angle smaller or equal to 30 °.

Table 5.1. SPECIFICATION OF PLANAR INSPECTION ARM

Property	Link Material	Link Diameter (mm)	Link Mass (g)	Joint Mass (g)	Motor Power (W)	Max. Continuous Motor Torque (mNm)	Joint Gear Ratio
Value	CFRP	50	205	947	15	25.5	100

The rotation angle of each joint motor is controlled by a PID controller implemented by a MAXON EPOS 24/5 motor driver. The motor drivers also feed motor rotation angle and motor currents to the upper computer running POT. The POT calculates appropriate watch thrusts and send thrust commends to a watch controller, which is an Arduino microcontroller. The upper computer is also responsible for sending arm configuration commands to the arm motor drivers. During an operation, the user only needs to specify arm configuration through the upper computer and the flying watches work fully automatically.

The demonstration is shown in Fig. 5.5. In the demonstration, the arm is commanded to follow the trajectory shown in Fig. 5.6. It took about 7 minutes for the arm to move from initial configuration to the final configuration. About 17 times slight or moderate thrust vibrations are observed. Although the slope angle is not measured, we can clearly see from Fig.5.5 that POT successfully enhance PIA to operate on a tilted plane.

Fig. 5.5. Demonstration of POT on PIA.

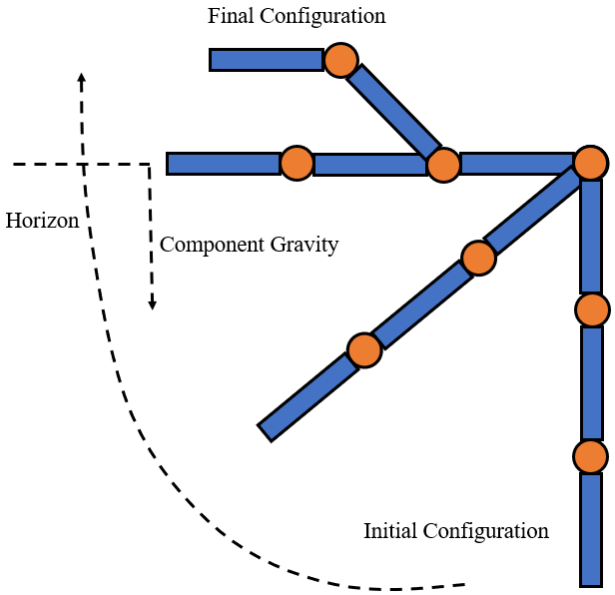

Fig. 5.6. PIA trajectory in POT demonstration.

5.3. Summary

In this Chapter, we proposed a model-free online thrust planner for flying watch called Physical-gradient-based Optimization of Thrust (POT). We firstly introduced the basic principle, system integration, and workflow of POT. Then each component of POT and how they are assembled together are explained in detail. Finally, POT is used to enhance a planar arm and extend its workspace from horizontal plane to a tilted plane in order to verify its effectiveness.

POT features very loose prerequisites to work (only actuator loads and arm configuration) and high portability (no modification is necessary for the original arm controller). This means it does no matter what kind of flying watch attachment allocation we use and what kind of arm-environment interaction and arm configuration happen and POT will always work to reduce actuator loads and thusly enhance robotic arms if the prerequisites are provided. Therefore, POT is suitable for swift deployment of flying watches for uncertain missions.

However, the flying watch users should understand that those POT features are for fighting arm and mission uncertainty instead of ignoring attachment allocation customization and mission conditions. As we have seen in Chapter 3, a brilliant mission-dependent flying watch attachment allocation can significantly improve flying watch performance (and vice versa, a very awfully-designed attachment allocation could lead to mission failure). Also, POT may also fail to response to an external force that is too strong or changes too fast. Therefore, the flying watch users are advised to customize flying watch attachment allocation using AOWS and rehearse a mission using WACAE based on available knowledge of the mission.

POT is essentially an algorithm of measuring appropriate flying watch thrusts for arm load reduction through deliberate watch vibrations and applying such thrust for arm enhancement. The fundamental reason that POT cannot response very fast is that it takes time to generate the

deliberate watch vibration and do meaningful measurement. More specifically, deliberate watch vibration is generated by slight watch thrust change. When a flying watch is commanded to change thrust, the propeller motor takes a small amount of time to response. Also, the air flows around the propeller go from one stable state through an unstable intermediate process to the final stable state. POT needs to wait until the final stable state to measure meaningful arm joint loads for calculating appropriate watch thrust. Both watch motor response and air flow response take time and delay POT response.

Since the watch motor response time and air flow response time are physical limitations that are difficult to overcome, the idea to make POT faster is to reduce the numbers of vibration and measurement. There are several potential ways as follows to achieve that.

1. Currently POT randomly select a subset of flying watches to do vibration and update their thrust. However, poorly selected flying watches are less effective for arm load reduction. For example, selected flying watches with horizontal thrust-generating directions are useless for counteracting arm gravity. It may be possible to intelligently select flying watch to do vibration using machine learning algorithms.

2. Before POT do watch vibrations, there is a memory-based thrust prediction process. Currently an interpolation algorithm named inverse distance weighting is used for that process. However, if we can predict flying watch thrust more accurately, the number of watch vibrations can be reduced. Incorporating arm dynamic model to thrust prediction process may improve prediction accuracy.

6. Conclusion

Long-reach robotic arms generally have large workspaces, long operation time, and redundant degrees of freedom. Because of those advantages, long robotic arms are used for many applications such as infrastructure inspection, nuclear plant decommissioning, and firefighting. However, current long robotic arms in the literature also have the following problems. (1) Proximal joints can be easily overloaded by distal reaction forces or arm gravity. (2) Even though some specialized arm designs with force counteraction mechanisms can solve the first problem to some extent, those specialized arm designs are very difficult to be applied to other existing long arms or be customized for diverse missions.

In order to solve those two problems, this dissertation proposes a watch-like thrust-generating attachable device, named flying watch, which can be attached to the links of a long robotic arms in a mission-dependent way and generate thrusts in cooperation with arm actuators to enhance arm strength. Because of those features, flying watch enhancement is a very useful method for boosting the strength and versatility of existing long robotic arms. In addition, flying watch enhancement also provides a new option for building a reconfigurable long arm (a basic long arm plus reconfigurable flying watch enhancement).

More specifically, this dissertation covers the mechanical design (Chapter 2), attachment allocation customization (Chapter 3), and thrust planning (Chapter 4 and Chapter 5) of flying watch. In Chapter 2, the mechanical design, selection, and dynamics of flying watch are introduced. The thrusts of propeller TGU and propellerless TGU are experimentally tested and those thrusts are theoretically estimated to be adequate for enhancing PIA and Giacometti arm respectively. Then in Chapter 3, the analysis tools (reduction rate, Thrust Drivability Surface, and Thrust Drivability) and automated design tools (AOWS) of flying watch attachment allocation are introduced. Those tools are important for understanding the properties of a flying

watch attachment allocation or fast designing of mission-dependent flying watch attachment allocations. Simulations in both static object holding and object manipulation missions show that AOWS-based flying watch attachment allocation design is more than 20% better in counteracting known reaction forces and more than 20% better in counteracting unexpected end effector reaction forces than human-experience-based flying watch attachment allocation design. In Chapter 4 and Chapter 5, a model-based offline thrust planner called WACAE and a model-free online thrust planner called POT are respectively introduced. WACAE requires the watch-arm equation of motion, the arm trajectory in a mission, and the external reaction forces in the mission to work. It features two levels of arm-actuator cooperation (WACAE-I and WACAE-II). In WACAE-I, the flying watch thrusts are adjusted to cooperate with actuator and reduce joint loads. In WACAE-II, not only do flying watches adjust thrusts, actuators also cooperate to position flying watches in optimal positions and orientations. WACAE is a suitable thrust planner for a known robotic arm in a known mission. WACAE can also be used to rehearse a mission and discover potential problems in advance. Simulations show WACAE can reduce more that 35% of maximum joint loads. POT requires only actuator loads and arm configurations feedback to work. Such loose requirements allow POT to fight different kinds of uncertainty, such as unexpected payload and arm configuration. As a result, POT is a suitable thrust planner for unfamiliar robotic arms or uncertain missions. The effectiveness of POT is shown by a physical demonstration, in which the workspace of a planar arm is successfully extended by POT to a tilted plane. Although POT has the ability to fight uncertainty, an awfully-designed flying watch attachment allocation can significantly compromise flying watch enhancement performance and an excessively strong or rapidly changing external reaction force can still lead to mission failure. Therefore, the flying watch users is advised to customize the flying watch attachment allocation using AOWS and rehearse a mission using WACAE based on available information of the mission.

There are several very interesting potential research topics on the basis of this dissertation.

Firstly, thrust-driven robotic arms as reviewed in Chapter 1, like Hiryu [13], [15] and LASDRA [14], can be regarded as special cases of flying watch enhanced arm when all loads on passive joint are counteracted by flying watches and flying watch allocations are not allowed to be customized. As a result, the thrust drivability theory and AOWS proposed in Chapter 3 should be applicable to those thrust-driven arms. It would be interesting to use those analysis tools to analyze the properties of existing thrust-driven arms and use AOWS to design new thrust-driven arms that are robust to unexpected environmental perturbation.

Secondly, most current long robotic arms move very slowly not just for safety reasons. High speed movements can result in large inertial torques on proximal joints that challenge arm actuators. Also, both WACAE and POT are designed for very slow arm movements. However, high speed long arm motions are useful for quick inspection. It would be interesting to design a flying watch thrust planner that can generate high speed long arm motions.

Thirdly, system identification methods are potentially useful for precisely estimating the Equation of Motion of a robotic arm attached with flying watches. Such models may improve the performance of model-based thrust planning method such as WACAE.

Finally, adaptive control algorithms may be used to control flying watches. In that situation, the problem of inaccurate model parameters may be overcome since the controller parameters can adapt to uncertainty or change of plant parameters.

Reference

[1] Xiao, X., Dufek, J., Suhail, M., & Murphy, R. (2018, October). Motion planning for a uav with a straight or kinked tether. In 2018 IEEE/RSJ International Conference on Intelligent Robots and Systems (IROS) (pp. 8486-8492). IEEE.

[2] Zikou, L., Papachristos, C., & Tzes, A. (2015, June). The power-over-tether system for powering small uavs: tethering-line tension control synthesis. In 2015 23rd Mediterranean Conference on Control and Automation (MED) (pp. 681-687). IEEE.

[3] Takeichi, M., Suzumori, K., Endo, G., & Nabae, H. (2017, September). Development of a 20-m-long Giacometti arm with balloon body based on kinematic model with air resistance. In *2017 IEEE/RSJ International Conference on Intelligent Robots and Systems (IROS)* (pp. 2710-2716). IEEE.

[4] Keller, D., Perrot, Y., Gargiulo, L., Friconneau, J. P., Bruno, V., Le, R., ... & Bonnemason, J. (2008, September). Demonstration of an ITER relevant remote handling equipment for Tokamak close inspection. In 2008 IEEE/RSJ International Conference on Intelligent Robots and Systems (pp. 1495-1500). IEEE.

[5] Rico, J. A. S., Endo, G., Hirose, S., & Yamada, H. (2017). Development of an actuation system based on water jet propulsion for a slim long-reach robot. Robomech Journal, 4(1), 8.

[6] Horigome, A., Yamada, H., Endo, G., Sen, S., Hirose, S., & Fukushima, E. F. (2014, May). Development of a coupled tendon-driven 3D multi-joint manipulator. In 2014 IEEE International Conference on Robotics and Automation (ICRA) (pp. 5915-5920). IEEE.

[7] Endo, G., Horigome, A., & Takata, A. (2019). Super dragon: a 10-m-long-coupled tendon-driven articulated manipulator. IEEE Robotics and Automation Letters, 4(2), 934-941.

[8] Ando, H., Ambe, Y., Ishii, A., Konyo, M., Tadakuma, K., Maruyama, S., & Tadokoro, S. (2018). Aerial hose type robot by water jet for fire fighting. IEEE Robotics and Automation Letters, 3(2), 1128-1135.

[9] Endo, G., Yamada, H., Yajima, A., Ogata, M., & Hirose, S. (2010, May). A passive weight compensation mechanism with a non-circular pulley and a spring. In 2010 IEEE International Conference on Robotics and Automation (pp. 3843-3848). IEEE.

[10] Morita, T., Kuribara, F., Shiozawa, Y., & Sugano, S. (2003, July). A novel mechanism design for gravity compensation in three dimensional space. In Proceedings 2003

IEEE/ASME International Conference on Advanced Intelligent Mechatronics (AIM 2003) (Vol. 1, pp. 163-168). IEEE.

[11] Hirose, S., Ishii, T., & Haishi, A. (2003, September). Float arm V: hyper-redundant manipulator with wire-driven weight-compensation mechanism. In 2003 IEEE International Conference on Robotics and Automation (Cat. No. 03CH37422) (Vol. 1, pp. 368-373). IEEE.

[12] Horigome, A., Endo, G., Suzumori, K., & Nabae, H. (2016, December). Design of a weight-compensated and coupled tendon-driven articulated long-reach manipulator. In 2016 IEEE/SICE International Symposium on System Integration (SII) (pp. 598-603). IEEE.

[13] Endo, G., Hagiwara, T., Nakamura, Y., Nabae, H., & Suzumori, K. (2018, July). A proposal of super long reach articulated manipulator with gravity compensation using thrusters. In 2018 IEEE/ASME International Conference on Advanced Intelligent Mechatronics (AIM) (pp. 1414-1419). IEEE.

[14] Yang, H., Park, S., Lee, J., Ahn, J., Son, D., & Lee, D. (2018, May). LASDRA: Large-size aerial skeleton system with distributed rotor actuation. In 2018 IEEE International Conference on Robotics and Automation (ICRA) (pp. 7017-7023). IEEE.

[15] Ueno, Y., Hagiwara, T., Nabae, H., Suzumori, K., & Endo, G. (2020). Development of Hiryu-II: A Long-Reach Articulated Modular Manipulator Driven by Thrusters. IEEE Robotics and Automation Letters, 5(3), 4963-4969.

[16] Pan, S., & Endo, G. (2019). Flying watch: an attachable strength enhancement device for long-reach robotic arms. ROBOMECH Journal, 6(1), 5.

[17] Liu, B., Huang, Z., Wei, J., Shi, C., Ota, J., & Zhang, Y. (2018, October). Jet-HR1: Stepping Posture Optimization for Bipedal Robot Over Large Ditch Based on a Ducted-fan Propulsion System. In 2018 IEEE/RSJ International Conference on Intelligent Robots and Systems (IROS) (pp. 6010-6015). IEEE.

[18] Huang, Z., Wang, Z., Wei, J., Yu, J., Zhou, Y., Lao, P., ... & Zhanga, Y. Three-Dimensional Posture Optimization for Biped Robot Stepping over Large Ditch Based on a Ducted-Fan Propulsion System . In 2020 IEEE/RSJ International Conference on Intelligent Robots and Systems (IROS) . IEEE.

[19] Fujikawa, T., Yamauchi, Y., Ambe, Y., Konyo, M., Tadakuma, K., & Tadokoro, S. (2019, September). Development of Practical Air-floating-type Active Scope Camera and User Evaluations for Urban Search and Rescue. In 2019 IEEE International Symposium on Safety, Security, and Rescue Robotics (SSRR) (pp. 1-8). IEEE.

[20] Garimella, G., & Kobilarov, M. (2015, May). Towards model-predictive control for aerial pick-and-place. In 2015 IEEE international conference on robotics and automation (ICRA) (pp. 4692-4697). IEEE.

[21] Seo, H., Kim, S., & Kim, H. J. (2017, May). Aerial grasping of cylindrical object using visual servoing based on stochastic model predictive control. In 2017 IEEE international conference on robotics and automation (ICRA) (pp. 6362-6368). IEEE.

[22] Ruggiero, F., Lippiello, V., & Ollero, A. (2018). Aerial manipulation: A literature review. IEEE Robotics and Automation Letters, 3(3), 1957-1964.

[23] Gabrich, B., Saldana, D., Kumar, V., & Yim, M. (2018, May). A flying gripper based on cuboid modular robots. In 2018 IEEE International Conference on Robotics and Automation (ICRA) (pp. 7024-7030). IEEE.

[24] Zhao, M., Kawasaki, K., Chen, X., Noda, S., Okada, K., & Inaba, M. (2017, May). Whole-body aerial manipulation by transformable multirotor with two-dimensional multilinks. In 2017 IEEE International Conference on Robotics and Automation (ICRA) (pp. 5175-5182). IEEE.

[25] Shi, F., Zhao, M., Murooka, M., Okada, K., & Inaba, M. (2020, May). Aerial Regrasping: Pivoting with Transformable Multilink Aerial Robot. In 2020 IEEE International Conference on Robotics and Automation (ICRA) (pp. 200-207). IEEE.

[26] Zhao, M., Anzai, T., Shi, F., Chen, X., Okada, K., & Inaba, M. (2018). Design, modeling, and control of an aerial robot dragon: A dual-rotor-embedded multilink robot with the ability of multi-degree-of-freedom aerial transformation. IEEE Robotics and Automation Letters, 3(2), 1176-1183.

[27] Staub, N., Mohammadi, M., Bicego, D., Delamare, Q., Yang, H., Prattichizzo, D., ... & Franchi, A. (2018). The tele-magmas: An aerial-ground comanipulator system. IEEE Robotics & Automation Magazine, 25(4), 66-75.

[28] Staub, N., Mohammadi, M., Bicego, D., Prattichizzo, D., & Franchi, A. (2017, May). Towards robotic MAGMaS: Multiple aerial-ground manipulator systems. In 2017 IEEE International Conference on Robotics and Automation (ICRA) (pp. 1307-1312). IEEE.

[29] Yang, H., Staub, N., Franchi, A., & Lee, D. (2018, October). Modeling and Control of Multiple Aerial-Ground Manipulator System (MAGMaS) with Load Flexibility. In 2018 IEEE/RSJ International Conference on Intelligent Robots and Systems (IROS) (pp. 1-8). IEEE.

[30] Osuka, K., Yoshida, K., & Ono, T. (1994, December). New design concept of space manipulator: a proposal of Torque-unit Manipulator. In Proceedings of 1994 33rd IEEE Conference on Decision and Control (Vol. 2, pp. 1823-1825). IEEE.

[31] Osuka, K., Yoshida, K., & Ono, T. (1996). Proposal of torque unit manipulator. Journal of the Robotics Society of Japan, 14(7), 1018-1025.

[32] PAN, S., & ENDO, G. (2019). A Proposal of a Watch-like Attachable Device for Long-Reach Robotic Arm Enhancement. In the Proceedings of JSME annual Conference on Robotics and Mechatronics (Robomec) 2019 (pp. 1P1-M08). The Japan Society of Mechanical Engineers.

[33] PAN, S., and Endo, G. A Proposal of Propellerless Watch-like Device for Long-reach Robotic Arm Enhancement. The 38th annual conference of the Robotics Society of Japan 2020.

[34] Pan, S., Endo, G. Toward mission-dependent long robotic arm enhancement: design method of flying watch attachment allocation based on thrust drivability. Robomech J 8, 11 (2021). https://doi.org/10.1186/s40648-021-00198-1

[35] Graf, W. E. (2005). Effects of duct lip shaping and various control devices on the hover and forward flight performance of ducted fan UAVs (Master Thesis, Virginia Tech).

[36] Paul S. K. (2009). A Brief Introduction to Mechanical and Biological Propulsion. https://s2.smu.edu/propulsion/Pages/thrustmain.htm. Accessed on 08/07/2020

[37] Engineering Toolbox. https://www.engineeringtoolbox.com/drag-coefficient-d_627.html. Accessed on 11/27/2020

[38] Siciliano, B., Sciavicco, L., Villani, L., & Oriolo, G. (2010). Robotics: modelling, planning and control. Springer Science & Business Media.

[39] Yoshikawa, T. (1985). Manipulability of robotic mechanisms. The international journal of Robotics Research, 4(2), 3-9.

[40] Yoshikawa, T. (1985, March). Manipulability and redundancy control of robotic mechanisms. In Proceedings. 1985 IEEE International Conference on Robotics and Automation (Vol. 2, pp. 1004-1009). IEEE.

[41] Bayle, B., Fourquet, J. Y., & Renaud, M. (2003). Manipulability of wheeled mobile manipulators: Application to motion generation. The International Journal of Robotics Research, 22(7-8), 565-581.

[42] Naksuk, N., & Lee, C. G. (2006, May). Zero moment point manipulability ellipsoid. In Proceedings 2006 IEEE International Conference on Robotics and Automation, 2006. ICRA 2006. (pp. 1970-1975). IEEE.

[43] Costa, J. T., & Yim, M. (2017, May). Designing for uniform mobility using holonomicity. In 2017 IEEE International Conference on Robotics and Automation (ICRA) (pp. 2448-2453). IEEE.

[44] Yamamoto, Y., & Yun, X. (1999, May). Unified analysis on mobility and manipulability of mobile manipulators. In Proceedings 1999 IEEE International Conference on robotics and automation (cat. no. 99ch36288c) (Vol. 2, pp. 1200-1206). IEEE.

[45] Merlet, J. P. (2006). Jacobian, manipulability, condition number, and accuracy of parallel robots. In Springer Tracts in Advanced Robotics Robotics Research 175–184. doi: 10.1007/978-3-540-48113-3_16.

[46] Kucuk, S., & Bingul, Z. (2006). Comparative study of performance indices for fundamental robot manipulators. Robotics and Autonomous Systems, 54(7), 567-573.

[47] Boyd, S., Boyd, S. P., & Vandenberghe, L. (2004). Convex optimization. Cambridge university press.

[48] Nakamura, Y., & Hanafusa, H. (1986). Inverse kinematic solutions with singularity robustness for robot manipulator control.

[49] Wampler, C. W. (1986). Manipulator inverse kinematic solutions based on vector formulations and damped least-squares methods. IEEE Transactions on Systems, Man, and Cybernetics, 16(1), 93-101.

[50] Asada, H., & Slotine, J. J. (1986). Robot analysis and control. John Wiley & Sons.

[51] Andrei, N. (2017). A SQP algorithm for large-scale constrained optimization: SNOPT. In Continuous Nonlinear Optimization for Engineering Applications in GAMS Technology (pp. 317-330). Springer, Cham.

[52] Vanderbei, R. J., & Shanno, D. F. (1999). An interior-point algorithm for nonconvex nonlinear programming. Computational Optimization and Applications, 13(1-3), 231-252.

[53] Pan, S., & Ishigami, G. (2017). Strategy optimization for energy efficient extraterrestrial drilling using combined power map. IEEE Robotics and Automation Letters, 2(4), 1980-1987.

[54] Pan S (2017). Strategy Optimization for Energy Efficient Robotic Extraterrestrial Drilling Tasks. Master Thesis, Keio University.

[55] Shepard, D. (1968, January). A two-dimensional interpolation function for irregularly-spaced data. In Proceedings of the 1968 23rd ACM national conference (pp. 517-524).

Publications

The content of this dissertation originates from the following publications.

Pan, S., & Endo, G. (2019). Flying watch: an attachable strength enhancement device for long reach robotic arms. ROBOMECH Journal, 6(1), 5. (Chapter 2 and 4)

PAN, S., & ENDO, G. (2019). A Proposal of a Watch-like Attachable Device for Long-Reach Robotic Arm Enhancement. In The Proceedings of JSME annual Conference on Robotics and Mechatronics (Robomec) 2019 (pp. 1P1-M08). The Japan Society of Mechanical Engineers. (Chapter 2)

PAN, S., and Endo, G. A Proposal of Propellerless Watch-like Device for Long-reach Robotic Arm Enhancement. The 38th annual conference of the Robotics Society of Japan 2020. (Chapter 2)

Pan, S., Endo, G. Toward mission-dependent long robotic arm enhancement: design method of flying watch attachment allocation based on thrust drivability. Robomech J 8, 11 (2021). https://doi.org/10.1186/s40648-021-00198-1 (Chapter 3)

Acknowledgments

The works contained in this dissertation result from close collaboration with Prof. Gen Endo. Many ideas presented in this dissertation are inspired from or develop through our discussions. In addition, I have learned many things from Prof. Endo, such as how to choose and solve research problems, how to present research results, and how to teach, etc. Therefore, I would like to thank Prof. Endo for his patient guidance in my doctoral studies.

I am also very grateful for the advice from Prof. Koichi Suzumori on my research, which helps me jump out of theoretical details and consider more carefully about the purpose of my research and the application scope of my proposals.

I would like to thank other members of Suzumori Endo lab for their kind help and advice. Especially, I would like to thank Prof. Hiroyuki Nabae, Tatsuhiro Hiramitsu, Kosuke Tani, Takashi Fujioka, Atsushi Takata, and Takahiro Ukida for teaching me many critical technical skills and patiently discussing research problems with me.

Finally, I am very grateful for the support from my family during my doctoral study.